Dispersion and dissipation in viscoelastic metamaterials: Theory, experiments and applications

by

Clémence L. Bacquet

M.S., University of Technology Compiègne, 2013

A thesis submitted to the

Faculty of the Graduate School of the

University of Colorado in partial fulfillment

of the requirements for the degree of

Doctor of Philosophy

Department of Aerospace Engineering Sciences

2018

This research proposal entitled:
Dispersion and dissipation in viscoelastic metamaterials: Theory, experiments and applications
written by Clémence L. Bacquet
has been approved for the Department of Aerospace Engineering Sciences

Prof. Mahmoud I. Hussein

Prof. Sedat Biringen

Prof. Carlos Felippa

Prof. Francisco López Jiménez

Prof. Fatemeh Pourahmadian

Date ______________

The final copy of this thesis has been examined by the signatories, and we find that both the content and the form meet acceptable presentation standards of scholarly work in the above mentioned discipline.

Bacquet, Clémence L. (Ph.D., Aerospace Engineering Sciences)

Dispersion and dissipation in viscoelastic metamaterials: Theory, experiments and applications

Thesis directed by Prof. Mahmoud I. Hussein

Phononic materials comprise microstructures engineered for unique, and often exotic, acoustic or elastic wave-propagation characteristics. For example, an elastic metamaterial, which is a type of phononic material, may be tuned to exhibit a band gap at frequencies corresponding to wavelengths much longer than the size of the microstructure. A common approach for realizing such extreme dynamical properties is to intrinsically distribute local resonators along the domain of the material. This concept has been extensively studied in the context of low-frequency vibration shielding, subwavelength focusing and imaging, and acoustic/elastic cloaking. However, despite the importance of dissipation in wave propagation, the effects of damping are often neglected in these applications, and in the elastodynamics literature in general. Incorporating damping in the treatment of metamaterials does not only provide a more realistic description of their dynamical behavior, but also allows one to understand and manipulate the complex interplay between dispersion, local resonances, and dissipation. The dispersion and resonance properties of a damped metamaterial may be controlled by changing the levels of dissipation, and, conversely, it is possible to enhance, or reduce, dissipation by engineering the dispersion properties.

The objective of this thesis is to advance the understanding of the connection between dispersion, local resonances, and dissipation in viscoelastically damped metamaterials and to develop a methodology for precise engineering of the dissipation. A viscoelastic damping model is fitted with experimental data for accurate prediction of dissipation within the dispersion and finite-structure analysis frameworks. An intriguing phenomenon that is investigated using this modeling framework is metadamping–a dissipation emergence phenomenon caused by the presence of local resonances. This concept is investigated in a real-world system, both numerically and experimentally. A methodology is developed to determine the levels of dissipation in a finite metamaterial pillared beam structure using only unit-cell analysis. With this information, guidelines are provided that enable engineering of the dissipation by varying the unit-cell dispersion properties. Results show that dissipation can either be enhanced, or reduced, within prescribed frequency ranges without sacrificing stiffness. This concept is first shown in the context of freely propagating waves and then extended to harmonically driven waves.

Acknowledgements

Firstly, I would like to express my sincere gratitude to my advisor Professor Mahmoud Hussein for his constant support throughout my PhD study, and for always pushing me to be a better researcher. He has offered me steadfast support in academia and beyond, and his guidance and enthusiasm made my graduate studies one of the best experience of my life.

Besides my advisor, I would like to thank my committee members: Professor Carlos Felippa, who has been a great teaching mentor, Professor Sedat Biringen, Professor Fatemeh Pourahmadian, and Professor Franscisco López Jiménez for their encouragement and their insightful comments. I am also very grateful for the support I received from the NSF CAREER Grant No. 1254931.

My sincere thanks also go to my colleagues at CU Boulder for the enlightening discussions and for making the lab such a friendly environment. Thank you Mike, Dimitri, Romik, Hossein, Amanda, Jonas, Mary, and especially Osama, for all the help and support you have provided me with during these five years. I would also like to extend my gratitude to my colleagues at ESI group for giving me the opportunity to join their team as an intern, and to my labmates at UIUC, Mehmet and Melih, who first inspired me to pursue a PhD program.

I would like to thank my amazing friends Virginia, Colleen, Ingrid, and so many others for making me my time in Boulder and San Diego such a marvellous one. I am grateful for your flawless support and for all the adventures we have had together, both on the wall and on the ground.

Last but not least, I would like to thank my parents, Anne and Michel, my sisters, Ariane and Agathe, and the rest of my family for believing in me and for always supporting my career choices, even when those choices meant moving halfway around the world.

Contents

Chapter

Tables

Table

Figures

Figure

Chapter 1

Introduction

Vibrations are omnipresent. In fact, they are an essential part of who we are. When sound waves enter our ears, our eardrums vibrate thus allowing us to hear; when light waves are reflected of objects, they undergo vibrations thus allowing us to see.

From an engineering perspective, however, vibrations are quite often undesirable, as they produce noise, increased stresses, added wear, premature fatigue in machines and structures, or even passenger discomfort in vehicles. If structural resonances are excited, structures can exhibit high levels of vibrations leading to catastrophic failure. An infamous example is the case of the Tacoma Narrows bridge, which dramatically collapsed due to wind-induced vibrations. Vibration mitigation is therefore necessary in numerous engineering problems and has been active field of research for the past decades. Nondissipative vibration isolation can be achieved by altering structural properties such as geometry and connections with adjoining structures; however, these alterations are limited in practice by engineering design criteria such as size or weight. Dissipative vibration isolation, on the other hand, aims at increasing the levels of dissipation within structures by introducing damping through layering of heavily damped materials. Layers of polymer are effective at reducing the levels of vibration but because of their low elasticity modulus, they are often not stiff enough to resist breakage or failure.

In many engineering applications, where structures are exposed to both static and dynamic loads, materials exhibiting both high stiffness and high damping are highly desirable. Unfortunately, naturally occurring materials are constrained by trade-off between these two properties. In this dissertation, we propose periodic elastic metamaterials as candidate materials to overcome the stiffness/damping trade-off. We show that, through precise engineering of their internal structure, we can enhance the levels of dissipation of existing materials such as aluminum.

1.1 Phononic Materials

Periodic materials and structures have long been recognized by researchers for their ability to manipulate waves in unique ways. This interest dates back to 1686, when Newton [85] attempted to derive a formula for the velocity of sound by studying a 1D periodic lattice. Two centuries later, Rayleigh made the first study of a continuous periodic structure when he investigated a stretched string whose density periodically varied along the length [92]. During the first half of the 20th century, most of the research efforts on periodic materials were carried out by physicists and electrical engineers, who developed mathematical models to study crystals, electrical circuits, electrical transmission lines, etc. [75]. It was not until the second half of the century that engineers recognized their great potential and applied similar analysis techniques to engineering materials and structures such as beams [19], composite materials [84, 106], and aircraft structures [77, 97].

A milestone was reached in the field of periodic materials when Yablonovich [120], shortly followed by John [44], introduced the concept of photonic materials in 1987. They investigated a dieletric structure, periodic in all three dimensions, and reported the existence of photonic band gaps, which are frequency ranges through which no electromagnetic wave (i.e., photon) is allowed to propagate.

A couple years later, the field of phononic materials emerged as researchers applied this concept of periodicity to the manipulation of vibrational and acoustic waves [98, 99]. Similarly, phononic materials exhibit phononic band gaps through which no elastic or acoustic wave (i.e., phonon) is allowed to propagate. Based on the manner in which the band gaps are generated, phononic materials can be divided into two categories: phononic crystals (PCs) and elastic metamaterials (EMs).

1.1.1 Phononic Crystals

Phononic crystals (PCs) are periodic structures formed by a building block, called the unit cell, which is repeated spatially in one, two, or three directions. Their unique dynamical properties arise from non-homogeneity in the unit cell, which is typically characterized by some form of disparity in the constituent material phases, the internal geometry, the boundary conditions, or a combination of them. The impedance mismatch caused by that change of material, geometry, boundary conditions within the unit cell leads to Bragg scattering, i.e., the canceling of waves due to destructive interferences between incident and reflected waves at certain frequencies. This phenomenon give rises to the most notable property of PCs, the band gaps, which are frequency ranges through which no acoustic or elastic waves is allowed to propagate.

PCs were first investigated in the early 1990s [98, 99], when Sigalas and Economou reported a band gap for elastic and acoustic waves in a structure made of periodic spheres embedded in a homogeneous host material. Since then, PCs have attracted the attention of scientists working in the field of vibrations and acoustics as their internalized vibration control make them ideal candidates for applications where wideband vibroacoustics mitigation is desired. For example, Richards and Pines [93] proposed to use a periodic shaft to reduce noise generated by the dynamic impact of gear meshes in helicopters. In a later study Sánchez-Dehese *et al.* [102] showed that periodically arranged, porous cylinders exhibited band gaps in both the transmittance and reflectance spectra, thus effectively creating a sound barrier. As of today, extensive research has been conducted on the applications of these materials, which go beyond vibration control. Some of these applications include wave filtering [87], wave guiding [49], and flow control [35].

Because the band-gap formation mechanism is based on Bragg scattering, PCs can only affect whose wavelengths are on the order of the periodicity of the unit cell. For low-frequency vibrations and therefore long wavelengths, the length of the unit cell becomes impractically large for most engineering applications. Figure 1.1 shows an example of a 1D PC material, where the unit cell, composed of one layer of aluminum and one layer of ABS, is repeated along the axial direction.

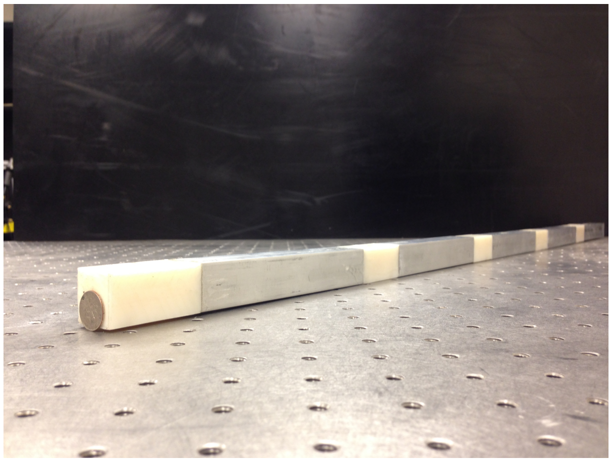

Figure 1.1: Photograph of 1D phononic crystal beam. The unit cell, made of aluminum and plastic (ABS), is repeated five times along the axial direction. (A dime is included for scale comparison.)

1.1.2 Elastic Metamaterials

Metamaterials (“meta” from Greek “beyond”) are artificially engineered materials whose properties are beyond those found in naturally occurring materials or even in phononic crystals. By making use of local resonance features (e.g., pillars, heavy bodies in a compliant matrix), they alter the wave propagation within the underlying medium and bestow unusual properties near the resonance frequency, such as negative effective density and/or modulus [24, 58]. In addition to these unique physical properties, metamaterials have the ability to affect waves much larger than themselves and therefore, to open band gaps in the sub-wavelength regime thus overcoming the limitation of phononic crystals at low frequencies. Indeed, the local-resonance band gaps do not depend on the spatial periodicity and are governed by the resonance frequency of the resonating substructure instead.

The first investigation of elastic metamaterials (EMs) was a study by Liu *et al.* [64] in 2000 in which the authors examined the dispersion characteristics of a 3D material composed of lead spheres coated with silicone rubber and embedded in an epoxy matrix. Excited with acoustic waves, the medium generated a band gap at a wavelength two orders of magnitude lower than its periodicity, indicating that periodicity is not required for the formation of band gaps in EMs. This capacity to generate band gaps in the sub-wavelength regime engendered a multitude of applications, including sub-wavelength focusing [30], sub-wavelength imaging [6], vibration and acoustic shielding [33], and acoustic cloaking [16]. Figure 1.2 shows an example of a 1D EM, where the unit cell is composed of a square pillar on top of a beam element.

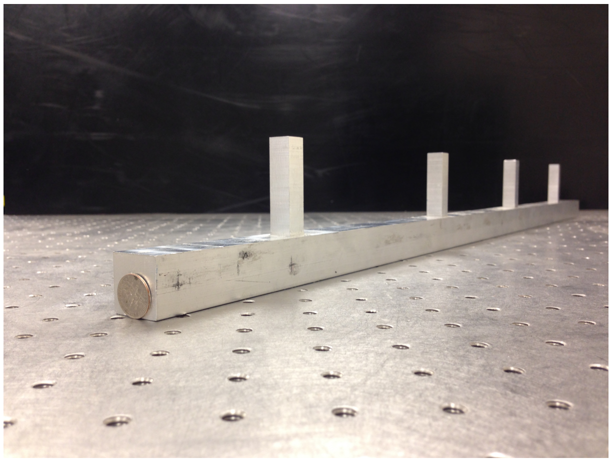

Figure 1.2: Photograph of 1D elastic metamaterial beam. The pillars act as local resonators. (A dime is included for scale comparison.)

1.1.3 Models and Equations

When studying phononic materials, two different approaches are usually considered: 'material' versus 'finite-structure'. The material approach consists of viewing the material as a unit cell that is spatially repeated to infinity (in one, two, or three directions) and provides the intrinsic dynamical properties of the material. The finite-structure approach, on the other hand, assumes a finite number of unit cells and provides the forced response in a conventional structural setting. In this subsection, we present the basic principles of wave propagation in phononic materials.

1.1.3.1 Material Approach

First, the PC and EM systems are considered as infinite materials. For simplicity, they are discretized as 1D, diatomic spring-mass systems (see Fig. 1.3), where m_1 and m_2 are the two masses, and k_1 and k_2 are the two spring constants.

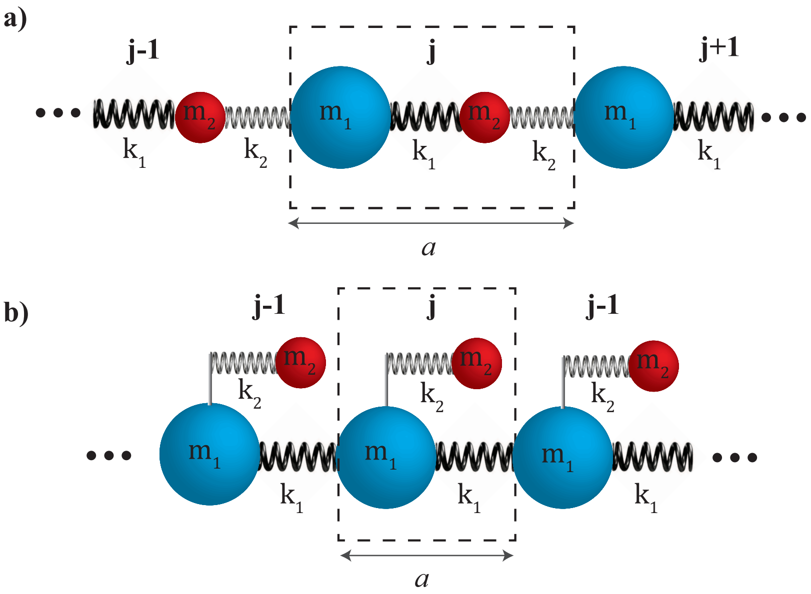

Figure 1.3: Lattice models of 1D infinite chains. **a)** phononic crystal (PC), **b)** elastic metamaterial (EM). The jth unit cells are highlighted (black dashed box).

For the PC system (see Fig. 1.3-a), the unit cell consists of two masses m_1 and m_2 connected in series by two springs k_1 and k_2. From work by [40], the equations of motion for each mass in the PC model are given by

$$m_1\ddot{u}_1^j + k_1(u_1^j - u_2^{j-1}) + k_2(u_1^j - u_2^j) = 0 \tag{1.1a}$$

and

$$m_2\ddot{u}_2^j + k_1(u_2^j - u_1^{j+1}) + k_2(u_2^j - u_1^j) = 0, \tag{1.1b}$$

where u_m^j is the displacement of the mth mass in the jth unit cell. The neighboring left and right unit cells are denoted by $j-1$ and $j+1$, respectively.

For the EM model (see Fig. 1.3-b), the unit cell is similar to that of the PC model except that the masses are now connected in parallel. The equations of motion for the displacement of m_1

and m_2 are as follows:

$$m_1\ddot{u}_1^j + k_1(2u_1^j - u_1^{j-1} - u_1^{j+1}) + k_2(u_1^j - u_2^j) = 0, \tag{1.2a}$$

and

$$m_2\ddot{u}_2^j + k_2(u_2^j - u_1^j) = 0. \tag{1.2b}$$

To obtain the dispersion characteristics of both systems, the generalized form of Bloch's theorem [11] is applied on the PC and EM unit cells. This theorem states that the wave field in a periodic medium is also periodic and is the product of an amplitude function with the unit-cell spatial periodicity a and a plane-wave envelope. The displacement response of the mth mass in the jth unit cell can be expressed as:

$$u_m^j(\kappa, t) = \tilde{U}_m(\kappa)e^{i(j\kappa a+\omega t)}, \tag{1.3}$$

where $\tilde{U}_m$ represents the periodic amplitude function of the mth mass, κ is the wavenumber, and ω is the frequency. The displacement at one end of the unit cell can, therefore, be related to that of the other end of the unit cell, such that:

$$u_m^{j+n}(\kappa, t) = u_m^j(\kappa, t)e^{in\kappa a}. \tag{1.4}$$

Substituting Eq. (1.3) into the two systems of equations (1.1) and (1.2), and recasting into a matrix form results in an eigenvalue problem given by

$$[\mathbf{M} - \omega^2\mathbf{K}(\kappa)]\tilde{\mathbf{U}}(\kappa) = 0, \tag{1.5}$$

where the mass $\mathbf{M}$ and stiffness $\mathbf{K}$ matrices for the PC and EM unit cells, respectively, are given by

$$\mathbf{M}_{PC} = \begin{bmatrix} m_1 & 0 \\ 0 & m_2 \end{bmatrix}, \ \mathbf{K}_{PC} = \begin{bmatrix} k_1 + k_2 & -(k_1e^{-i\kappa a} + k_2) \\ -(k_1e^{i\kappa a} + k_2) & k_1 + k_2 \end{bmatrix} \tag{1.6}$$

and

$$\mathbf{M}_{EM} = \begin{bmatrix} m_1 & 0 \\ 0 & m_2 \end{bmatrix}, \ \mathbf{K}_{EM} = \begin{bmatrix} 2k_1(1 - cos(\kappa a)) & -k_2 \\ -k_2 & k_2 \end{bmatrix}. \tag{1.7}$$

We select the spring and mass parameters for the PC system to be $m_1^{PC} = 1$, $m_2^{PC} = 2$, and $k_1^{PC} = k_2^{PC} = 2,000$. For a fair comparison between the PC and EM systems, we require that they be statically equivalent, i.e., that they have the same speed of sound in the long-wavelength regime $c = \lim_{\kappa\to 0}(\omega/\kappa)$ [40]. For the PC, $c_{stat}^{PC} \simeq 18.25$ m/s, therefore, the parameters for the EM system are defined such that $c_{stat}^{EM} = c_{stat}^{PC}$, which yields $m_1^{EM} = 1$, $m_2^{EM} = 2$, and $k_1^{EM} = k_2^{EM} = 1,000$. Figures 1.4-a and 1.4-b show the dispersion curves obtained by solving Eq.(1.5) for the PC and EM systems, respectively. Dispersion diagrams, which relate frequency to wavenumber, provide a useful insight about the wave-propagation characteristics of the two systems. Moreover, they are a powerful tool for design for properties such as locations and widths of band gaps can easily be inferred from the dispersion diagram. Here, the PC band gap, caused by Bragg scattering, ranges from 7.1 to 10 Hz , whereas the EM band gap, caused by hybridization of the local resonator with the underlying medium, is significantly lower, and ranges from 3.1 to 6.2 Hz.

1.1.3.2 Finite-Structure Approach

Next, the PC and EM systems are analyzed as finite structures made of $n = 50$ unit cells and their frequency response functions (FRFs) are obtained. For a finite system, the equation of motion under a harmonic excitation is

$$\mathbf{M}\ddot{\boldsymbol{u}}(t) + \mathbf{K}\boldsymbol{u}(t) = \boldsymbol{f}(t), \tag{1.8}$$

where $f(t) = \boldsymbol{F}e^{i\omega t}$. Assuming a harmonic displacement $\boldsymbol{u}(t) = \boldsymbol{X}e^{i\omega t}$, substituting it into Eq. (1.8) and rearranging the terms yields

$$\boldsymbol{X}(\omega) = (\mathbf{K} - \omega^2\mathbf{M})^{-1}\boldsymbol{F}(\omega). \tag{1.9}$$

FRF plots are given in Figs. 1.4-c and 1.4-d. It is interesting to note that the FRFs follow a similar behavior to that of the dispersion curves. Indeed, in the frequency ranges that correspond to the band gaps, the amplitude responses decrease significantly, indicating that no wave propagates in

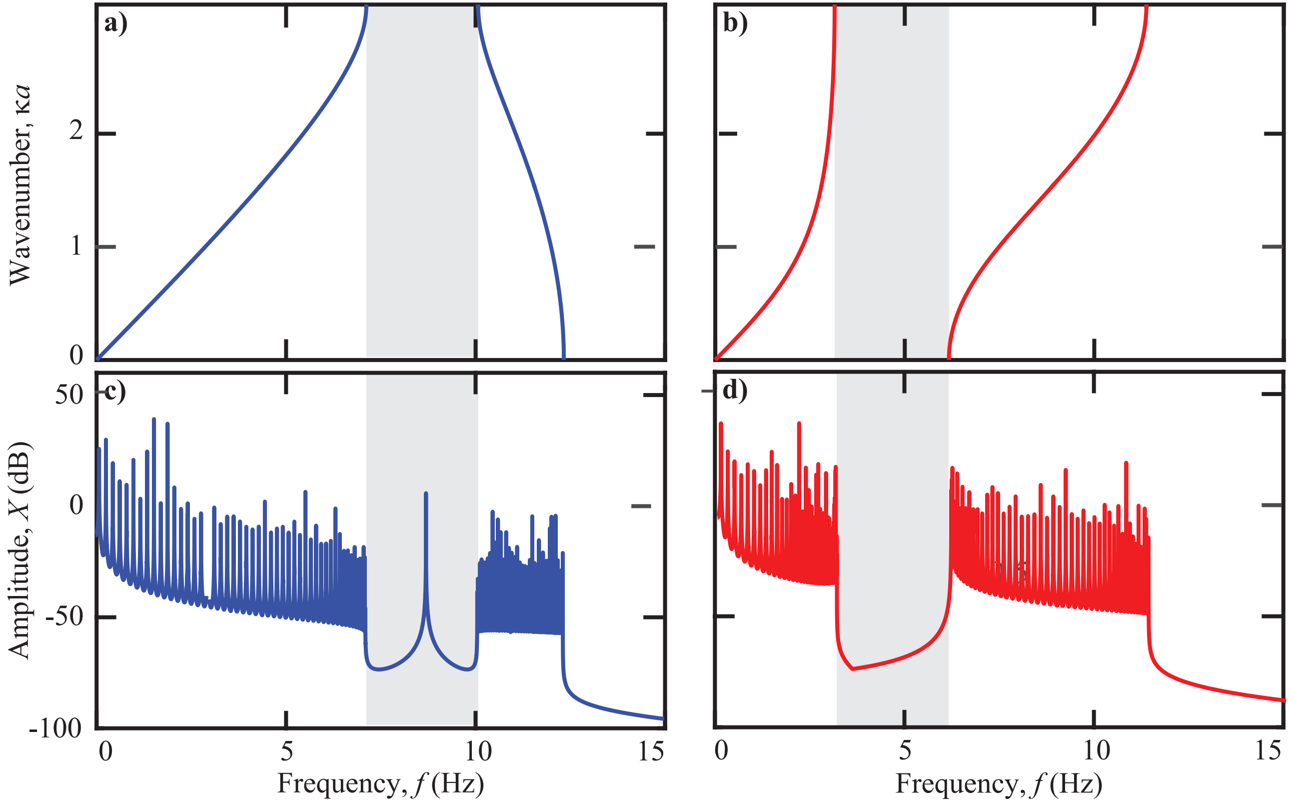

Figure 1.4: *Material approach*: Dispersion diagrams for the **a)** PC system (blue), **b)** EM system (red); *Structure approach*: Frequency response functions for the **c)** PC system (blue), **d)** EM system (red). Band gaps are shaded in grey.

this frequency range. On Fig. 1.4-c, however, one peak remains in the band gap. This peak, called truncation resonance, arises from truncating an infinite chain of unit cells to one with a finite number of unit cells.

In addition, we plot in Fig. 1.5-a the displacement of the $50th$ mass of the PC system (resp., EM system) in response to a sinusoidal excitation applied on the $1st$ mass. The excitation is of the form $f(t) = sin(2\pi f_r t)$, where f_r is the frequency of excitation in Hz. For each system, we select two excitation frequencies f_{rBG} and f_{rPB}, such that f_{rBG} falls within the bang gap and f_{rPB} is within one of the pass bands. The time responses are obtained by numerically solving Eq. (1.8)

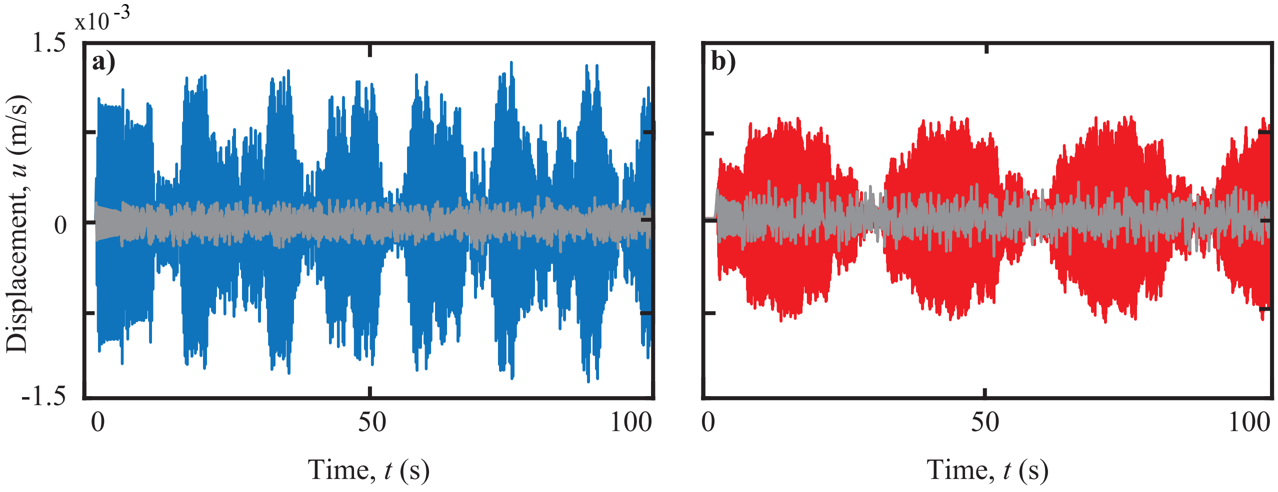

Figure 1.5: **a)**: *PC system*: Displacement of the 50*th* mass excited in one of the pass bands at $f_{rPB} = 5$ Hz (blue) and in the band gap at $f_{rBG} = 9$ Hz (grey). **b)** *EM system*: Displacement of the 50*th* mass excited in one of the pass bands at $f_{rPB} = 10$ Hz (red) and in the band gap at $f_{rBG} = 5$ Hz (grey).

for $0 \leq t \leq 100$ s using the Newmark-β method:

$$\mathbf{A}_{i+1} = \mathbf{M}^{-1}(\boldsymbol{F}_{i+1} - \mathbf{K}\boldsymbol{X}_{i+1}) \tag{1.10}$$

$$\boldsymbol{V}_{i+1} = \boldsymbol{V}_i + \Delta t[(1-\gamma)\boldsymbol{A}_i + \boldsymbol{A}_{i+1}] \tag{1.11}$$

$$\boldsymbol{X}_{i+1} = \boldsymbol{X}_i + \Delta t\boldsymbol{V}_i + \Delta t^2[(\frac{1}{2} - \beta)\boldsymbol{A}_i + \beta\boldsymbol{A}_{i+1}], \tag{1.12}$$

where $\boldsymbol{A}_i$, $\boldsymbol{V}_i$, $\boldsymbol{X}_i$ are the acceleration, velocity and displacement vectors at time step t_i. We choose $\gamma = \frac{1}{2}$ and $\beta = 0$, such that the method is at least second-order accurate and fully explicit (for these parameters, the method becomes identical to the central difference method). The time step $\Delta t = 10^{-4}$ s is chosen to ensure both stability and convergence of the results. In Fig. 1.5-a, we show the time responses of the 50*th* of PC system excited in the band gap at $f_{rBG} = 9$ Hz and in one of the pass bands at $fr_{rPB} = 5$ Hz. The amplitude of the displacement decreases significantly (by one order of magnitude) when the frequency of excitation falls within the band gap versus in a pass band. A similar behavior is observed for the EM system with $f_{rBG} = 5$ Hz and $fr_{rPB} = 10$ Hz.

1.2 Damping in Phononic Materials

Damping is present in every structure and material and greatly impacts wave propagation. Yet, because of the diversity and complexity of its mechanisms, it is often neglected or oversimplified in the phononic materials literature, especially in the dispersion analysis. Some studies have examined the effects of material damping on the transmission properties of finite phononic materials. Psarobas *et al.* [90] studied the effect of viscoelastic damping on 3D sonic crystals composed of viscoelastic rubber spheres in air and reported an omnidirectional transmission band gap. Merheb *et al.* [80] investigated the transmission properties of rubber/air PCs and showed a strong attenuation of transmission over wide ranges of frequencies. Oh *et al.* [42] examined the wave attenuation and dissipation mechanisms in viscoelastic phononic crystals with different inclusions. However, these studies mostly focused on the effect of damping on transmission properties and paid little attention to its effects on the dispersion characteristics. Introducing material damping in the unit-cell analysis provides a more realistic description of the intrinsic dynamics of the system. Furthermore, it also allows phononic materials to realize their full potential and opens the door to novel applications involving enhancement or reduction of dissipation in materials [40], as described in chapter 4.

The impact of damping on the dispersion of phononic materials is usually assessed by studying its effects on the dispersions curves. Depending on the type of wave-propagation problem (free versus driven), two approaches are followed to solve the damped eigenvalue problem: either the wavenumbers are fixed to real values ($\omega(\kappa)$-formulation) or the frequencies are fixed to real values ($\kappa(\omega)$-formulation). The $\omega(\kappa)$-formulation allows the frequencies to be complex, which corresponds to freely propagating waves, and is therefore employed to describe temporal dissipation. The $\kappa(\omega)$-formulation, on the other hand, allows the wavenumbers to be complex, which corresponds to harmonically driven waves, and is employed to describe spatial attenuation (caused by dissipative mechanisms). A literature review of both methods will be given in chapter 2.

Regardless of the type of wave-propagation problem (free or forced) and the method chosen to solve it, one still has to select a damping model, which often proves to be a challenging tasks. The complexity of damping lies in the diversity of dissipative mechanisms. Very often, a simple structure exhibits multiple sources of damping: internal damping (atomistic level), boundary damping (structural joints), damping due to acoustic radiation, friction damping, etc. Moreover, dissipative mechanisms are often nonlinear: damping can increase (or decrease) nonlinearly with the amplitude of excitation, or with temperature. Over the past two centuries, extensive research has been conducted on vibration damping and numerous models have been proposed, each with their own assumptions and simplifications. Because its equations of motion are simple and linear, viscous damping is one of the simplest models, and probably the most popular. A further simplification — Rayleigh (or proportional) damping [91]—is often employed in the phononic materials literature to model vibrations [4, 23, 88]. In some cases, viscous damping is a fair assumption, especially when the damping levels are low. However, in most cases a nonviscous damping model is required in order to accurately describe the dissipation mechanisms taking place in damped phononic materials. Therefore, over the past couple years, an increasing number of studies have modeled damped wave propagation through phononic materials using viscoelastic damping models [39, 55, 62].

1.3 Metadamping

When it comes to vibration control, conventional materials are constrained by a trade-off between their dissipation capacity and their mechanical resistance. For example, viscoelastic materials such as rubber are highly dissipative but are often not stiff enough to resist high mechanical loads. On the other hand, metals can resist high levels of load before failure but dissipate little energy. In many applications, where high dynamic loads can lead to premature material fatigue and catastrophic failure, it is desirable for an engineering material to possess a high capacity to dissipate energy while retaining high levels of stiffness and/or strength. Over the past decades, great efforts have been made to overcome this challenge and design materials featuring both high damping and high stiffness. Several approaches based on the engineering of composite materials have been proposed. Some researchers have investigated polymers reinforced with negative-phase inclusions in a matrix [43, 59] or carbon-nanotube, engineered trusses [78]. Others have examined a hybrid concept combining composite materials with polymers, such as thin layers of polymer sandwiched between stiffer layers [13, 95] or coated around stiff inclusions [65]. Zhang *et al.* [122] replicated the structure of biological bones, which consists of hard prisms arranged in staggered layers in a soft matrix, and reported an enhancement of damping with minimal loss in stiffness.

Metamaterials have been gaining a lot of attention lately as they offer a possible solution to the stiffness/damping trade-off. *Metadamping*, a damping emergence phenomena caused by the presence of a local resonance, was recently proposed in the context of simple spring-mass systems [26, 40]. When compared to an equivalent phononic crystal, it was shown in [40] and [26] that the metamaterial exhibited higher dissipation levels for the same prescribed damping. Several studies emerged afterwards following the metadamping concept. Antioniadis *et al.* [8] proposed a linear oscillator with a negative-stiffness element which was shown to achieve a promising enhancement of dissipation when applied to a 1D acoustic metamaterial lattice. More recently, a hybrid system between a phononic crystal and acoustic metamaterial, referred to as phononic resonator, was shown to greatly enhance metadamping with a careful choice of parameters [20]. However, despite promising results, the concept of metadamping has only been shown theoretically and in the context of lumped systems. In order for this concept to leave the realm of fundamental science and be used in practice by engineers, its realization needs to be shown in an experimental continuous system.

1.4 Thesis Objectives

The objectives of this thesis are to advance the understanding of the relation between dispersion and dissipation in viscoelastically damped metamaterials and to develop a methodology for precise engineering of the dissipation in experimental EMs.

The key results can be summarized as follows:

- Experimental fitting of a damping model for accurate prediction of dissipation within the dispersion analysis framework.

- Validation of metadamping in a finite experimental setting with direct correlation to theory as described within the dispersion framework
- Theoretical extension of the concept of metadamping to the driven-waves problem with qualitative and quantitative verification.

1.5 Summary of Chapters

This chapter introduces the topic phononic materials. The fundamental equations describing the dynamics of these materials are derived for simple 1D spring-mass systems. First, the system is considered as an infinite material and fundamental concepts of the dispersion analysis are presented. Then, the infinite system is truncated and analyzed as a finite structure. Classical methods of structural dynamics such as time integration or frequency-response analysis are employed. This chapter also introduces the topic of damping in phononic materials and presents one of its appealing applications: metadamping. For both of these topics, a brief literature review is presented.

The second chapter develops the framework for the treatment of damping in phononic materials. The two classes of problems, i.e. free-wave versus driven-wave propagation, as well as their respective formulations are discussed. The damped equations of motion are derived for the lattice system presented in the first chapter. The dispersion eigenvalue problem is solved for different levels of prescribed damping. The effects of damping on the dispersion curves obtained with both formulations ($\omega(\kappa)$ versus $\kappa(\omega)$) are compared and discussed.

The third chapter describes the treatment of damping in continuous 3D phononic materials in the context of free-wave propagation. A viscoelastic damping model, whose parameters are curve-fitted with experimental data, is developed and applied to two 3D beam unit cells. This model provides a realistic description of the damped wave propagation in phononic materials within the dispersion analysis framework. Moreover the effects of viscous versus viscoelastic damping on the dispersion curves are analyzed.

The fourth chapter explores an innovative application for damped phononic materials: metadamping. Its existence in a 3D elastic metamaterial beam is demonstrated both experimentally and numerically. A parametric design study is also performed in order to examine the effects of pillar spacing on the levels of metadamping. Finally, a simplified analytical model is proposed to determine bounds on both positive and negative metadamping.

The fifth chapter investigates metadamping in a 3D elastic metamaterial beam for frequency-driven waves. The existence of both positive metadamping is verified both qualitatively as well as quantitatively in the unit-cell and finite-structure analyses.

Chapter 2

Damped Phononic Materials: Preliminary Concepts

2.1 Introduction

Because damping plays such a crucial role on the intrinsic dynamics of phononic materials, an increasing number of researchers have been incorporating damping in their studies. Depending on the type of problem one is looking at, i.e., free or forced vibrations, damping is introduced in the eigenvalue problem using one of two formulations. Their key distinction is based on whether the wavenumbers are fixed to real values—allowing the frequencies to be complex ($\omega(\kappa)$-formulation)—or whether the frequencies are fixed to real values —allowing the wavenumbers to be complex ($\kappa(\omega)$-formulation). In this chapter, we introduce both formulations and derive their equations for a 1D lattice system. We then investigate the effects of dissipation on the dispersion relation and compare the results obtained with both formulations.

2.2 Formulations for Damped Wave Propagation

2.2.1 Freely Propagating Waves: $\omega(\kappa)$-Formulation

The first approach ($\omega(\kappa)$-formulation) corresponds to free vibrations, which occur when a structure or material responds to an impulsive excitation. In this case, the wavenumbers are constrained to real values and the frequencies are complex, thus accounting for energy loss over time. Mukherjee and Lee [82] investigated the wave-propagation characteristics in a viscoelastic periodic composite. They introduced damping using a complex elastic modulus, assumed real wavenumbers and derived the complex frequencies. Similarly, Sprik and Wedgam [103] used complex sound velocities to model damping in a 3D solid-viscous fluid composite material. Zhang *et al.* [124] studied the absolute acoustic band gaps in 2D systems consisting of silica cylinders in a viscous liquid using a plane-wave expansion method. They modeled damping with a complex velocity but assumed that the viscous damping parameter was frequency independent. Wei and Zhao [117] followed a similar approach and showed that both the location and width of the band gaps in a 2D phononic crystal composed of cylindrical fillers embedded periodically in a viscoelastic host was affected by the viscosity of host material. Hussein [37] and Hussein and Frazier [38] derived the damped dispersion relation in the case of general viscous damping, for both 1D and 2D phononic materials, and showed that damping alters the band structure. For certain levels of prescribed damping, they observed branch overtaking and branch cut-off phenomena, which can result in changes in the band-gap width and in the formation of partial wavenumber band gaps. In a subsequent study, Hussein and Frazier [39] considered a viscoelastic model based on a convolution integral. They extended to unit-cell problems the state-space approach that was first developed in [114] to solve for the eigenvalues of exponentially damped, finite structures.

2.2.2 Harmonically Driven Waves: $\kappa(\omega)$-Formulation

The second approach ($\kappa(\omega)$-formulation), where frequencies are fixed to real values and wavenumbers are allowed to be complex, corresponds to harmonically driven waves, which implies that only spatial dissipation is considered (in addition, of course, to attenuation mechanisms due to Bragg scattering and local resonance phenomena). As the wavenumbers are complex, both propagating and evanescent modes can be obtained from the dispersion analysis.

Mead [76] was the first to study harmonic-wave propagation in a 1D periodic structure in the context of a linear eigenvalue problem. Following this approach, Mehreb *et al.* [80] proposed a method to incorporate viscoelastic damping in a 2D silicon rubber/air PC. They considered a compressible general linear viscoelastic fluid model with frequency-dependent elastic moduli that they implemented using a finite-domain, time-difference method. Moiseyenko and Laude [81] investigated the influence of material loss on the complex band structure and group velocity in 2D viscoelastic PCs. They introduced damping through a complex elasticity tensor, whose imaginary part was assumed to increase linearly with frequency. Collet *et al.* proposed a new Floquet-Bloch formulation to compute the complex wavenumbers of 2D PCs with non-homogeneous and generic frequency-dependent damping terms. Andreassen and Jensen [7] compared the band diagrams obtained with both $\omega(\kappa)$- and $\kappa(\omega)$-formulations band and showed that the dispersion diagrams and temporal decays were in good agreement for small to medium amounts of material dissipation and for long wavelengths. Recent studies have looked at the effects of viscoelastic damping on the dispersion and attenuation characteristics of locally resonant materials The viscoelastic material losses present in the matrix and/or in the resonator coating were introduced through a KelvinVoigt [55] or generalized Maxwell model [55, 62].

2.2.3 Simultaneously Complex Wavenumbers and Frequencies

It is commonly assumed that only one of the variables can be complex: either the wavenumber κ, in which case it is a driven-wave problem, or the frequency, in which case it is a free-wave problem. For harmonically driven waves, this assumption holds as, by definition, the frequency has to be real. Therefore, only the wavenumber can be complex. However, for freely propagating waves, nothing prevents spatial dissipation to take place in addition to temporal dissipation, i.e, in principle, it is possible to have a complex wavenumber even when the frequency is complex. Recently, Frazier had Hussein [27] proposed an algorithm based on a $\kappa = \kappa(\lambda)$ formulation to solve this problem in the context of proportionally damped 1D lattice systems. This algorithm, however, does not apply to generally damped problem as the eigenvalue problem becomes nonlinear.

2.3 Effects of Dissipation on the Dispersion Relations: Example for a 1D PC Lattice

The effects of viscous damping on the dispersion curves are illustrated for the 1D PC model shown in Fig.1.3-a. (More complex damping models will be detailed in chapter 3.) Two viscous dampers c_1 and c_2 are added between the masses m_1 and m_2, as shown in Fig.2.1.

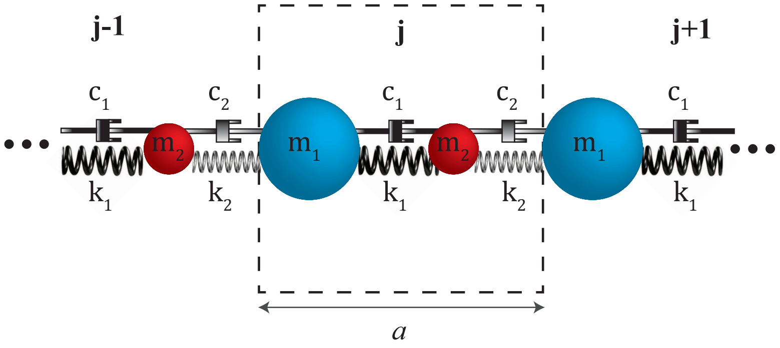

Figure 2.1: Model of 1D infinite lattice for a PC lattice with viscous dampers.

According to [40], with damping, the equations of motion for the PC derived in Eq.(1.1) become:

$$m_1\ddot{u}_1^j + c_1(\dot{u}_1^j - \dot{u}_2^{j-1}) + c_2(\dot{u}_1^j - \dot{u}_2^j) + k_1(u_1^j - u_2^{j-1}) + k_2(u_1^j - u_2^j) = 0, \tag{2.1a}$$

and

$$m_2\ddot{u}_2^j + c_1(\dot{u}_2^j - \dot{u}_1^{j+1}) + c_2(\dot{u}_2^j - \dot{u}_1^j) + k_1(u_2^j - u_1^{j+1}) + k_2(u_2^j - u_1^j) = 0. \tag{2.1b}$$

Similarly, Eqs. (2.1) can be recasted into matrix form. The mass and stiffness matrices given in Eq. (1.6) remain unchanged. In addition, the damping matrix is:

$$\mathbf{C}_{PC} = \begin{bmatrix} c_1 + c_2 & -(c_1 e^{-i\kappa a} + c_2) \\ -(c_1 e^{i\kappa a} + c_2) & c_1 + c_2 \end{bmatrix}. \tag{2.2}$$

2.3.1 Free Waves: Derivation of the $\omega(\kappa)$-Formulation

As mentioned in Section 2.1, in the $\omega(\kappa)$-formulation, the wavenumbers κ are fixed and real. For each wavenumber, the complex frequencies can be determined by solving the following eigenvalue problem:

$$[\lambda^2(\kappa)\mathbf{M} + \lambda(\kappa)\mathbf{C}(\kappa) + \mathbf{K}(\kappa)]\tilde{\boldsymbol{U}}(\kappa) = \mathbf{0}. \tag{2.3}$$

In the case of general damping (i.e., damping is nonproportional), it is not possible to solve for Eq. (2.3) directly. Therefore, this second-order problem must be converted to a first-order problem through a state-space transformation, such that [54]:

$$\left(\begin{bmatrix}\mathbf{K}(\kappa) & \mathbf{0}\\ \mathbf{0} & \mathbf{I}\end{bmatrix} - \lambda\begin{bmatrix}-\mathbf{C}(\kappa) & -\mathbf{M}\\ \mathbf{I} & \mathbf{0}\end{bmatrix}\right)\begin{Bmatrix}\tilde{\boldsymbol{U}}(\kappa)\\ \lambda(\kappa)\tilde{\boldsymbol{U}}(\kappa)\end{Bmatrix} = \begin{Bmatrix}\mathbf{0}\\ \mathbf{0}\end{Bmatrix}. \tag{2.4}$$

The solutions of Eq. (2.4) are the complex eigenvalues:

$$\lambda_s(\kappa) = -\zeta_s(\kappa)\omega_s(\kappa) \pm i\omega_{ds}(\kappa), \tag{2.5}$$

where the imaginary part ω_{ds} represents the damped frequencies corresponding to branch s, and the real part is the product of the wavenumber-dependent damping ratios ζ_s with the resonant frequencies $\omega_s = |\lambda_s|$. Note that in the case of viscous proportional damping, the resonant frequency is equal to the undamped frequency. The damped-dispersion and damping-ratio diagrams, which provide insight about the dissipation associated with each Bloch mode, can be derived from Eq. (2.5). Figures 2.2-a and 2.2-b display the damped-dispersion and damping-ratio diagrams for three levels of prescribed damping: low ($c_1 = c_2 = 10$), medium ($c_1 = c_2 = 20$) and high ($c_1 = c_2 = 50$). For comparison, the undamped dispersion curves are also plotted in Fig. 2.2-a.

2.3.2 Harmonically Driven Waves: Derivation of the $\kappa(\omega)$-Formulation

In this approach, the frequencies ω are fixed and real. At each frequency, the corresponding complex wavenumbers are found by solving a quadratic eigenvalue problem. Recall the damping matrix obtained after enforcement of Bloch boundary conditions:

$$\mathbf{C}_{PC} = \begin{bmatrix} c_1 + c_2 & -(c_1 e^{-i\kappa a} + c_2)\\ -(c_1 e^{i\kappa a} + c_2) & c_1 + c_2\end{bmatrix}. \tag{2.6}$$

Substituting $\gamma = e^{i\kappa a}$ into Eq. (2.6) yields

$$\mathbf{C}_{PC} = \begin{bmatrix} c_1 + c_2 & -\frac{1}{\gamma}c_1 - c_2\\ -\gamma c_1 - c_2 & c_1 + c_2\end{bmatrix}. \tag{2.7}$$

Similarly, we can rewrite the stiffness matrix in terms of γ:

$$\mathbf{K}_{PC} = \begin{bmatrix} k_1 + k_2 & -\frac{1}{\gamma}k_1 - k_2\\ -\gamma k_1 - k_2 & k_1 + k_2\end{bmatrix}. \tag{2.8}$$

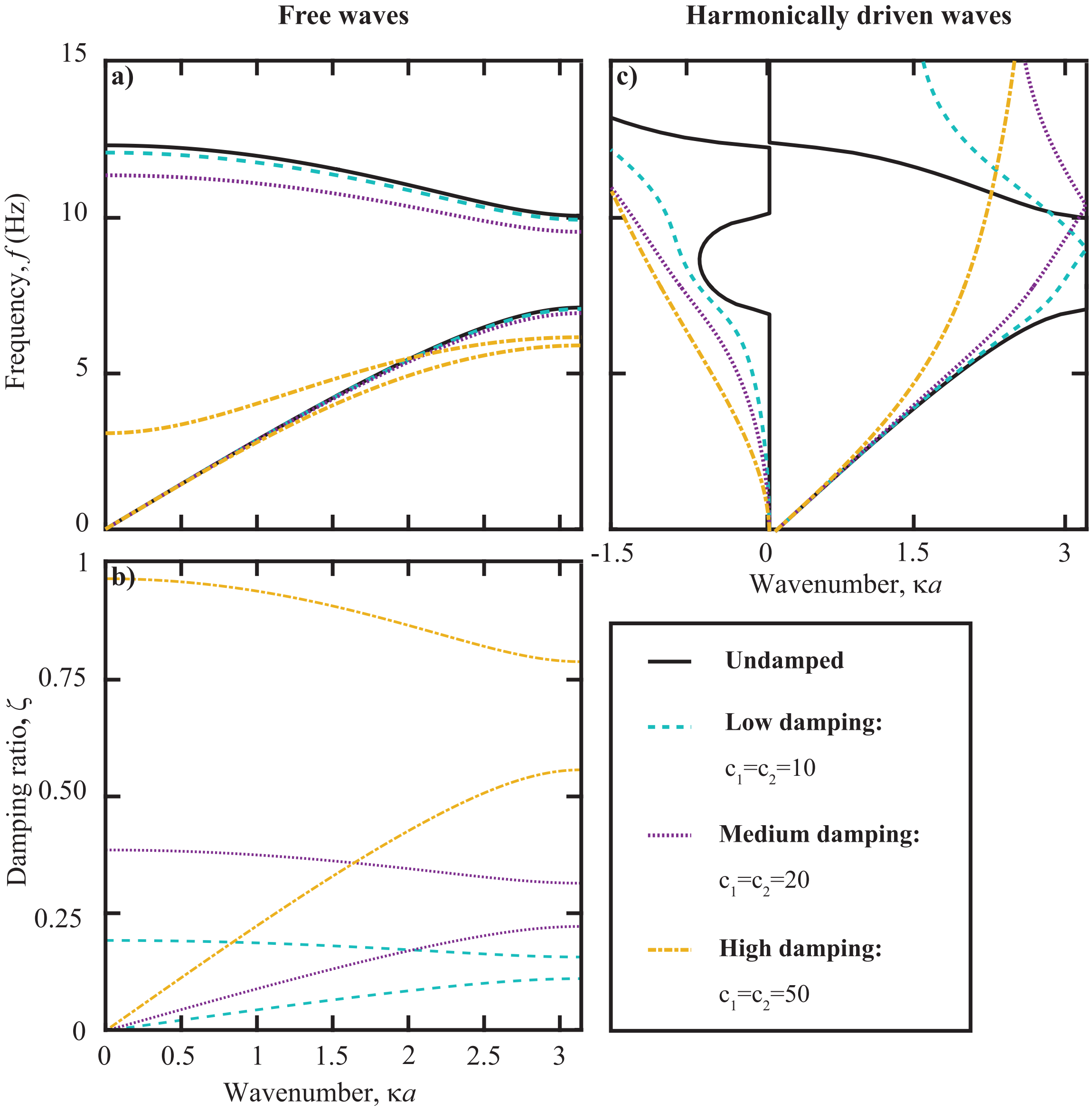

Figure 2.2: *Free waves*: **a)** Damped dispersion curves for three levels of prescribed damping: low, medium, and high. The undamped dispersion curves are plotted as a reference in black. **b)** Corresponding damping-ratio diagram. **c)** *Harmonically driven waves*: Dispersion curves for the three levels of prescribed damping.

Equations (2.7) and (2.8) can be rewritten as functions of γ:

$$\bar{\mathbf{C}} = \bar{\mathbf{C}}_0 + \gamma \bar{\mathbf{C}}_1 + \gamma^2 \bar{\mathbf{C}}_2. \tag{2.9a}$$

$$\bar{\mathbf{K}} = \bar{\mathbf{K}}_0 + \gamma\bar{\mathbf{K}}_1 + \gamma^2\bar{\mathbf{K}}_2 \tag{2.9b}$$

Substituting Eqs. (2.9) into Eq. (2.3) yields the following quadratic eigenvalue problem:

$$[\underbrace{(\bar{\mathbf{K}}_0 + \lambda\bar{\mathbf{C}}_0 + \lambda^2\bar{\mathbf{M}}_0)}_{\bar{\mathbf{A}}_0} + \kappa \underbrace{(\bar{\mathbf{K}}_1 + \lambda\bar{\mathbf{C}}_1)}_{\bar{\mathbf{A}}_1} + \kappa^2 \underbrace{(\bar{\mathbf{K}}_2 + \lambda\bar{\mathbf{C}}_2)}_{\bar{\mathbf{A}}_2}]\tilde{\mathbf{U}} = \mathbf{0}, \tag{2.10}$$

where $\lambda = i\omega$. Similarly, this eigenvalue problem can be"linearized" through a state-space transformation [53]:

$$\left(\begin{bmatrix} \bar{\mathbf{A}}_0(\omega) & \mathbf{0} \\ \mathbf{0} & \bar{\mathbf{I}} \end{bmatrix} - \gamma \begin{bmatrix} -\bar{\mathbf{A}}_1(\omega) & -\bar{\mathbf{A}}_2(\omega) \\ \mathbf{I} & \bar{\mathbf{0}} \end{bmatrix} \right) \begin{Bmatrix} \tilde{\mathbf{U}} \\ \gamma\tilde{\mathbf{U}} \end{Bmatrix} = \begin{Bmatrix} \mathbf{0} \\ \mathbf{0} \end{Bmatrix}. \tag{2.11}$$

The solutions of Eq. (2.11) are the frequency-dependent, complex eigenvalues $\gamma(\omega)$, from which we can extract the complex wavenumbers:

$$\kappa(\omega) = \frac{\ln \gamma(\omega)}{ia} \tag{2.12}$$

The solution in Eq. (2.12) can be decomposed into its real and imaginary parts:

$$\kappa(\omega) = \kappa_R(\omega) + i\kappa_I(\omega). \tag{2.13}$$

The real part of Eq. (2.13) corresponds to propagating modes (plotted here as positive wavenumbers) whereas the imaginary part represents evanescent modes, i.e., modes that decay in space (plotted here as negative wavenumbers). The dispersion curves are plotted for the same three levels of prescribed damping as those applied in the free-wave case (see Fig. 2.2-c).

2.3.3 Free Waves versus Driven Waves

As expected, both methods yield the same dispersion curves for the undamped case (black curves). Depending on the class of wave-propagation problem, i.e, free or driven, the effects of damping on the dispersion characteristics of the unit cell vary drastically. For example, in the case of free waves, the optical branch (upper branch) tends to drop for increasing the levels of prescribed damping, and can even drop below the acoustical branch (lower branch) if the levels of prescribed damping are very high. On the other hand, in the case of driven waves, the shape both dispersion branches changes quite significantly, and we can also notice the interesting phenomenon of bang-gap closing.

Chapter 3

Modeling of Damping in Elastic Metamaterials

3.1 Introduction

Chapter 2 introduced the basic concepts of damping for 1D lattice phononic materials. In this chapter, we extend the treatment of damping to continuous, 3D phononic materials. A viscoelastic damping model, whose parameters are curve-fitted with experimental data, is developed and applied to two 3D beam unit cells. For the sake of completeness, the viscous damping model derived in chapter 2 is rederived in this chapter. We will only focus of damping in the context of free waves; models driven-wave problems will be discussed in details in chapter 5.

3.2 Viscous Damping

Viscous damping is the best introduction to the concept of damping in that the equations of motion of a viscously damped system are simple and linear. In introductory vibration classes, this damping model is typically represented by viscous dashpots, which real-life examples are door closers, or shock absorbers. A linear dashpot uses a piston to exert a force on a viscous flow. That damping force opposes the motion and is proportional to the relative velocity such as $\mathbf{f}_d = \mathbf{C}\dot{\boldsymbol{u}}(t)$. The equations of motion for discrete lattice systems with viscous dashpots were derived in chapter 2. For convenience, there are rederived here for general continuous systems.

The free equations of motion for a system with general viscous damping are given by

$$\mathbf{M}\ddot{\boldsymbol{u}}(t) + \mathbf{C}\dot{\boldsymbol{u}}(t) + \mathbf{K}\boldsymbol{u}(t) = \mathbf{0}. \tag{3.1}$$

where **M**, **C** and **K** are the mass, damping, and stiffness matrices, respectively. General solutions of Eq. (3.1) are assumed to be of the form:

$$\boldsymbol{u}(t) = \tilde{\boldsymbol{U}}(x, \kappa)e^{\lambda t}, \tag{3.2}$$

where λ is the frequency. In the literature, λ is commonly prescribed as an imaginary value $\lambda = i\omega$, where ω is a real frequency, thus representing waves decaying in space only. To account for temporal energy dissipation, and therefore waves decaying in time, we assume that λ is a complex number [38]. Applying Bloch's theorem, the total displacement field is given by

$$\boldsymbol{u}(t) = \tilde{\boldsymbol{U}}(\kappa)e^{i\kappa x + \lambda t}. \tag{3.3}$$

Substituting Eq. (3.3) in Eq. (3.1) yields a quadratic eigenvalue problem:

$$[\lambda^2(\kappa)\mathbf{M} + \lambda(\kappa)\mathbf{C}(\kappa) + \mathbf{K}(\kappa)]\tilde{\boldsymbol{U}}(\kappa) = \mathbf{0}. \tag{3.4}$$

We note here that Bloch periodicity has been enforced through a Bloch operator method [36]. The plane-wave term was embedded within the element derivation through Eq. (3.3), and, as a result, the stiffness and damping matrices in Eq. (3.4) depend on the wavenumber κ. Again, the second-order problem in Eq. (3.4) can be rearranged into a first-order problem through a state-space transformation:

$$\left(\begin{bmatrix} \mathbf{K}(\kappa) & \mathbf{0} \\ \mathbf{0} & \mathbf{I} \end{bmatrix} - \lambda \begin{bmatrix} -\mathbf{C}(\kappa) & -\mathbf{M} \\ \mathbf{I} & \mathbf{0} \end{bmatrix} \right) \begin{Bmatrix} \tilde{\boldsymbol{U}}(\kappa) \\ \lambda(\kappa)\tilde{\boldsymbol{U}}(\kappa) \end{Bmatrix} = \begin{Bmatrix} \mathbf{0} \\ \mathbf{0} \end{Bmatrix}. \tag{3.5}$$

The solutions of Eq. (3.5) are the complex frequencies and appear in complex conjugate pairs:

$$\lambda_s(\kappa) = -\zeta_s(\kappa)\omega_s(\kappa) \pm i\omega_{ds}(\kappa), \tag{3.6}$$

where the imaginary part $\omega_{ds}(\kappa)$ represents the damped frequencies corresponding to branch s, and the real part is the product of the wavenumber-dependent damping ratios $\zeta_s(\kappa)$ with the resonant frequencies $\omega_s(\kappa)$.

As briefly mentioned in chapter 1, there are two methods to enforce Bloch periodicity: Bloch operator and Bloch boundary conditions. In this chapter, the Bloch-operator method is employed but we briefly discuss here the Bloch boundary conditions method, which are enforced as follows. First, the equations of motion are formed for a free unit cell with no periodicity (at this stage, the equations are equivalent to those of a finite structure made of one unit cell). Then, the equations are discretized with the finite-element method (FEM) and Bloch periodic conditions— which relate the displacement and stress fields of the degrees of freedom (DOFs) at one end of the unit cell to that of the DOFs on the other end— are applied with a Bloch periodicity matrix which contains the plane-wave terms. In that case, Eq. (3.4) becomes

$$[\lambda^2(\kappa)\bar{\mathbf{M}} + \lambda(\kappa)\bar{\mathbf{C}} + \bar{\mathbf{K}}]\tilde{\boldsymbol{U}}(\kappa) = \mathbf{0}, \tag{3.7}$$

where $\bar{\mathbf{M}} = \mathbf{P}^*\mathbf{M}\mathbf{P}$, $\bar{\mathbf{C}} = \mathbf{P}^*\mathbf{C}\mathbf{P}$, and $\bar{\mathbf{K}} = \mathbf{P}^*\mathbf{K}\mathbf{P}$. The Bloch periodicity matrix $\mathbf{P}$ is a function of the wavenumber and relates the DOFs at one end of the unit-cell to those at the other end of the unit cell. Its complex conjugate is denoted as $\mathbf{P}^*$. Detailed derivations, as well as a thorough analysis of both methods, can be found in [52].

3.3 Viscoelastic Damping

Viscous damping is simple to implement and may be suitable to account for dissipation associated with the presence of fluids, however, it typically fails at modeling material damping in a physically realistic way. This is why we consider here a nonviscous damping model. Viscoelastic damping is commonly introduced through complex material properties such as complex Young's moduli [7] $E(\omega) = E'(\omega) + iE''(\omega)$ (diagrams for a wide selection of materials can be found in the literature [46]) or complex sound velocities [69] $c_L(\omega) = c'_L(\omega) + ic''_L(\omega)$. As a result, damping is introduced through the stiffness matrix, which becomes complex, and no extra term to account for the damping force is needed in equation of motion. However, because of their frequency dependency, these quantities typically require solving the damped equation of motions with a $\kappa(\omega)$-formulation and are therefore more appropriate to describe damping in the context of driven-wave propagation. In this chapter, we focus on damping models in the context of free-wave propagation; damping in the context of driven waves will be investigated in chapter 5.

Other simple nonviscous damping models can be built as a combination of viscous and elastic elements [46] such as the Maxwell model (spring in series with dashpot), the Voigt model (spring in parallel with dashpot), or the standard model which is combination between the Maxwell and Voigt elements. These types of models, however, also lead to a frequency-dependent complex stiffness matrix, which again, are challenging to implement in a $\omega(\kappa)$-formulation.

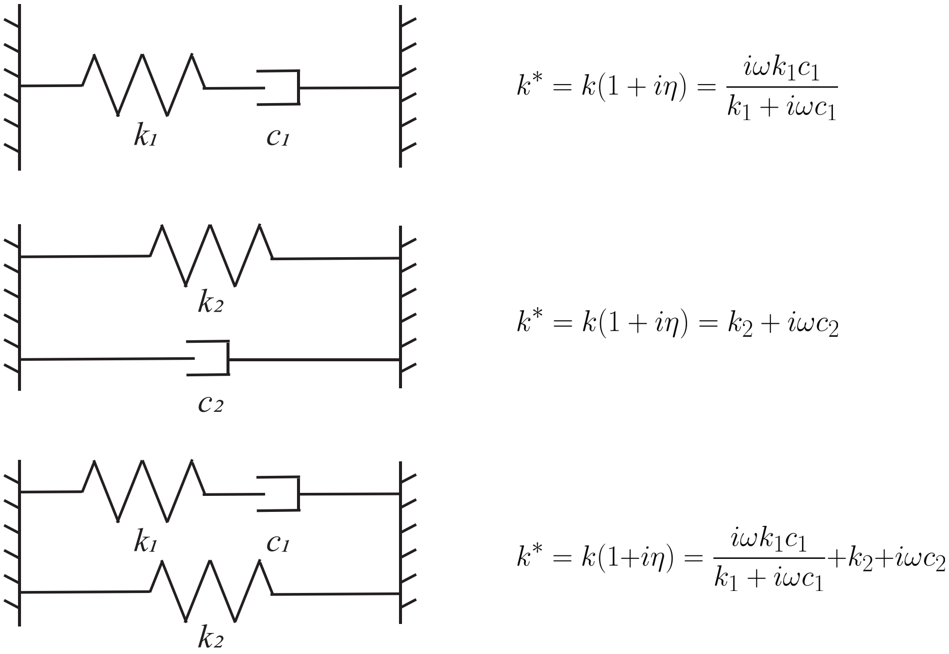

$$k^* = k(1 + i\eta) = \frac{i\omega k_1 c_1}{k_1 + i\omega c_1}$$

$$k^* = k(1 + i\eta) = k_2 + i\omega c_2$$

$$k^* = k(1+i\eta) = \frac{i\omega k_1 c_1}{k_1 + i\omega c_1} + k_2 + i\omega c_2$$

Figure 3.1: **a)** Maxwell model, **b)** Voigt model, **c)** Standard model. [46]

In other models such as fractional derivative models [28, 66, 110] or convolution integral models [29, 118], damping is incorporated via a damping force. Consequently another term has to be added in the equation of motion, which means that a damping matrix has to be specified. In this chapter, we assume exponential damping which is a case of damping based on a convolution integral [3]. As stated by Boltzmann's hereditary theory, the damping force depends on the past history of motion via a convolution integral over a kernel function $G(t)$ [118]. We select one of the simplest forms of these kernel functions which is based on the Maxwell model (see Fig. 3.1-a). As seen on Fig. 3.1, the Maxwell model consists of a linear spring (that accounts for mechanical energy storage during loading) placed in series with a viscous damper (that represents the energy loss) and its associated kernel function can be described by $G(t) = \mu_1 e^{\mu_2 t} H(t)$ where $\mu_{1,2}$ are the relaxation parameters [114].

Assuming that the degree of hereditary is 1 (hence, $\mu = \mu_1 = \mu_2$), the equation of motion of a system with exponential damping is [114]:

$$\mathbf{M}\ddot{\boldsymbol{u}}(t) + \int_0^t \mu e^{-\mu(t-\tau)} \mathbf{C}\dot{\boldsymbol{u}}(\tau) d\tau + \mathbf{K}\boldsymbol{u}(t) = \boldsymbol{f}(t) \tag{3.8}$$

The band structure is obtained by setting $\boldsymbol{f}(t) = 0$ in Eq. (3.8) and by assuming a Bloch solution of the form $\boldsymbol{u}(t) = \tilde{\boldsymbol{U}}(\kappa) e^{i\kappa x + \lambda t}$. The internal variable $\boldsymbol{v}$ is defined in [39] as follows:

$$\boldsymbol{v} = \int_0^t \mu e^{-\mu(t-\tau)} \dot{\boldsymbol{u}}(\tau) d\tau. \tag{3.9}$$

Applying Leibniz rule to Eq. (3.9) gives:

$$\dot{\boldsymbol{v}} = \mu[\dot{\boldsymbol{u}} - \boldsymbol{v}]. \tag{3.10}$$

Substituting Eq. (3.10) into Eq. (3.8) yields

$$\mathbf{M}\ddot{\boldsymbol{u}} + \mathbf{C}(\kappa)[\dot{\boldsymbol{u}} - \frac{1}{\mu}\dot{\boldsymbol{v}}] + \mathbf{K}(\kappa)\boldsymbol{u} = \mathbf{0}. \tag{3.11}$$

Premultiplying Eq.(3.10) by $\mathbf{C}$ and dividing by μ^2:

$$-\frac{1}{\mu}\mathbf{C}(\kappa)\dot{\boldsymbol{u}} - \frac{1}{\mu^2}\mathbf{C}(\kappa)\dot{\boldsymbol{v}} + \frac{1}{\mu}\mathbf{C}(\kappa)\boldsymbol{v} = \mathbf{0}. \tag{3.12}$$

Combining Eq.(3.11) and Eq. (3.12), we obtain the eigenvalue problem in state-space form [39]:

$$\left(\begin{bmatrix} \mathbf{0} & \mathbf{M} & \mathbf{0} \\ \mathbf{M} & \mathbf{C}(\kappa) & -\frac{1}{\mu}\mathbf{C}(\kappa) \\ \mathbf{0} & -\frac{1}{\mu}\mathbf{C}(\kappa) & \frac{1}{\mu^2}\mathbf{C}(\kappa) \end{bmatrix} + \gamma \begin{bmatrix} -\mathbf{M} & \mathbf{0} & \mathbf{0} \\ \mathbf{0} & \mathbf{K}(\kappa) & \mathbf{0} \\ \mathbf{0} & \mathbf{0} & \frac{1}{\mu}\mathbf{C}(\kappa) \end{bmatrix} \right) \boldsymbol{y} = \mathbf{0}, \tag{3.13}$$

where $\boldsymbol{y} = [\dot{\boldsymbol{u}} \quad \boldsymbol{u} \quad \boldsymbol{v}]$.

Solving Eq. (3.13) yields a set of six eigenvalues, which have the same form as the eigenvalues for the viscous eigenproblem (see Eq. (3.6)). However, there are now three pairs of roots instead of two: two complex conjugate pairs that physically represent the modes of damped wave propagation, and one pair of roots that represent spurious non-oscillating solutions [39]. It is interesting to note that, as μ tends to infinity, the viscous damping eigenvalue problem from Eq. (3.4) is recovered.

3.4 Experimental Curve-Fitting of the Damping Parameters

The mass $\mathbf{M}$ and stiffness $\mathbf{K}$ matrices in Eq. (3.13) are obtained upon discretization of Eq. (3.8) using the FEM. The damping matrix $\mathbf{C}(\kappa)$ in Eq. (3.8) is constructed assuming proportional damping such that $\mathbf{C}(\kappa) = p\mathbf{M} + q\mathbf{K}(\kappa)$. The relaxation parameter μ, as well as the proportional damping parameters p and q are unknown and are therefore selected with the help of laboratory vibration testing. In this procedure, a numerical FRF is curve-fitted with the experimental FRF until the numerical modal damping ratios match the experimental ones. The procedure to select the parameters is described in the following section for an aluminum beam.

3.4.1 Description of the Experimental Set-Up

The experimental FRF is obtained as follows. A $32 \times 1 \times 1$ inch aluminum beam is suspended using nylon cords in order to simulate free-free boundary conditions. An accelerometer (PCB WJ35C65) is fixed on one of the ends of the beam, at the center point of the cross-section. Impulsive excitations are applied with an impact hammer with a metal tip (PCB 086C02) at a point located at the center of the opposite cross-section, such that only the longitudinal modes are excited and measured. An effort was made to keep the levels of the input force constant for all measurements. After each hammer hit, the quality of the impulse is checked to ensure that no double impulse was applied and that sufficient energy was input in the frequency range of interest.

The measurements are collected with a NI-DAQ 9234 data acquisition system. The frequency rate is set to 25.6 kHz and the sample time is 10 s to ensure that the time signal decays to zero. For averaging purposes, five time series are recorded. The inertance spectrum is obtained by post-processing the time data using a commercial software package (MATLAB, The MathWorks Inc., Natick, MA, 01760, USA). First, because no trigger was used during the test, the excitation and response signals are cropped such that, for all measurements, the impulse starts at the same time $t_0 = 0.2$s (see Fig. 3.3) and the time series have the same length $t = 7$ s.

The cropped signals are transformed to the frequency domain by using the Fourier transform

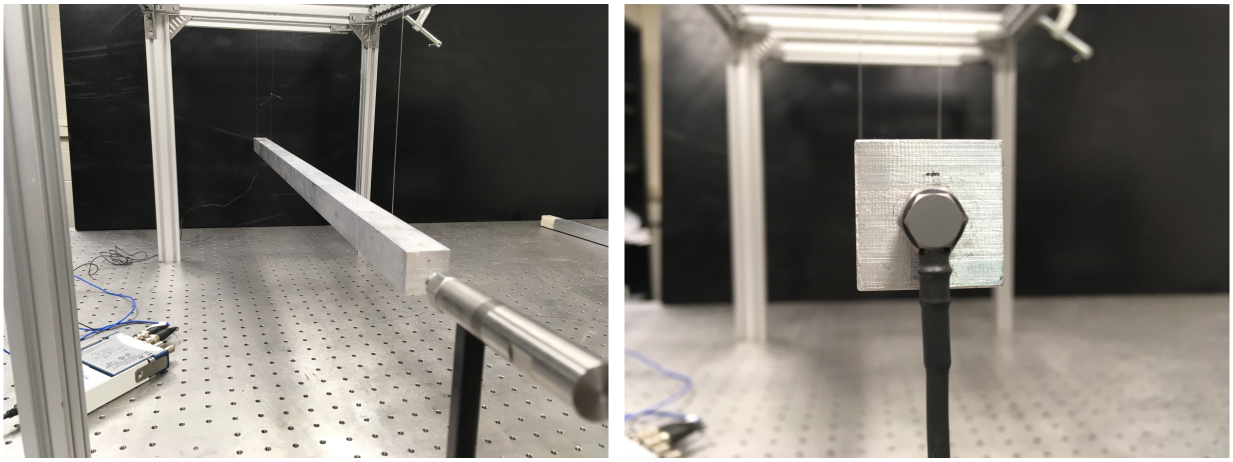

Figure 3.2: Photograph of the experimental set-up used to extract the damping parameters.

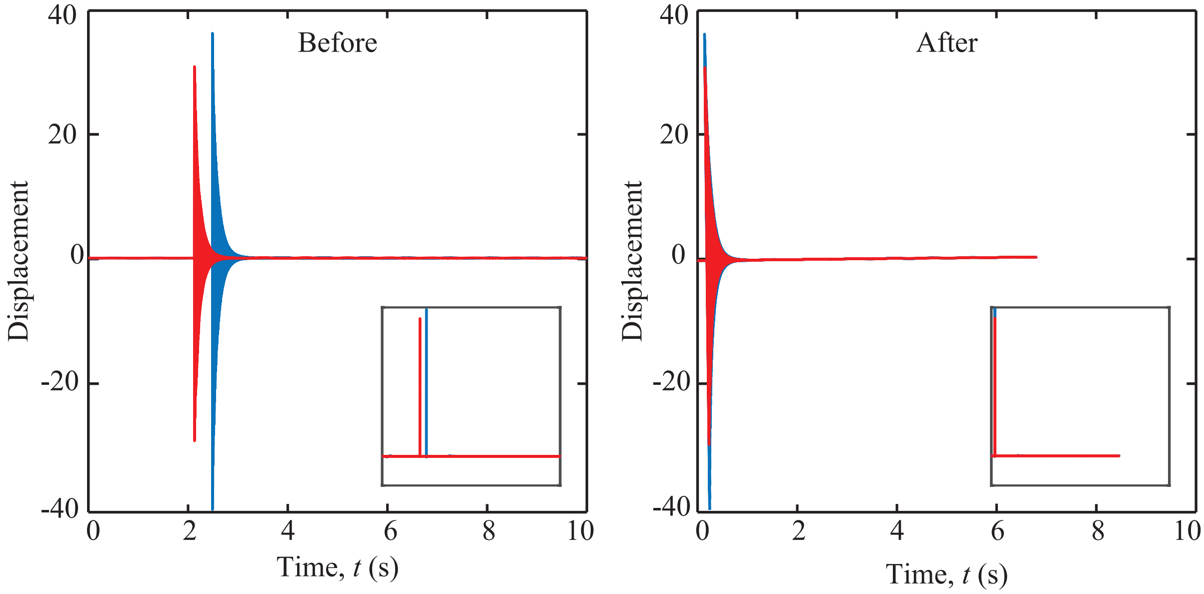

Figure 3.3: Examples of output time signals before and after cropping. The corresponding input signals are shown in the insets.

method. The excitation and response linear spectra are averaged, and the auto- and crosspower spectra are computed using MATLAB built-in functions (*pwlech* for the autopower spectra, and *cspd* for the crosspower spectra). The system transfer functions are then computed [23]:

$$H_1 = \frac{S_{rf}}{S_{ff}} \qquad H_2 = \frac{S_{fr}}{S_{rr}}, \tag{3.14}$$

where the crosspower spectrum S_{rf} (resp. S_{fr}) is the complex conjugate of the output (resp. output) spectrum and the input (resp. output) spectrum, and the autopower spectrum S_{ff} (resp. S_{rr}) is the complex conjugate of the input (resp. output) spectrum to itself. The H_1 transfer-function estimator tends to underestimate the actual transfer function H and is more sensitive to noise on the input. The H_2 transfer-function estimator, on the other hand, tends to overestimate H and is more sensitive to noise on the output. There exist other estimators for H but they are not considered here. The coherence function γ is usually used as an indicator of the quality and consistency of the measurements:

$$\gamma = \frac{H_1}{H_2}. \tag{3.15}$$

Values range from 0 (low-quality measurements, the amplitude and phase are not repeatable from one measurement to another) to 1 (high-quality measurements, the amplitude and phase are very repeatable from one measurement to another.)

The two transfer-function estimators H_1 and H_2 for the longitudinal modes of the aluminum beam are plotted and compared in the frequency range of interest $0 \leq f \leq 8$ kHz. As can be seen on Fig. 3.4-a, they show excellent agreement. The coherence is depicted on Fig. 3.4-b. Over the frequency range of interest, its value is mostly 1, indicating repeatable and high-quality measurements. For the rest of this study, we will consider the transfer function to be $H = H_1$.

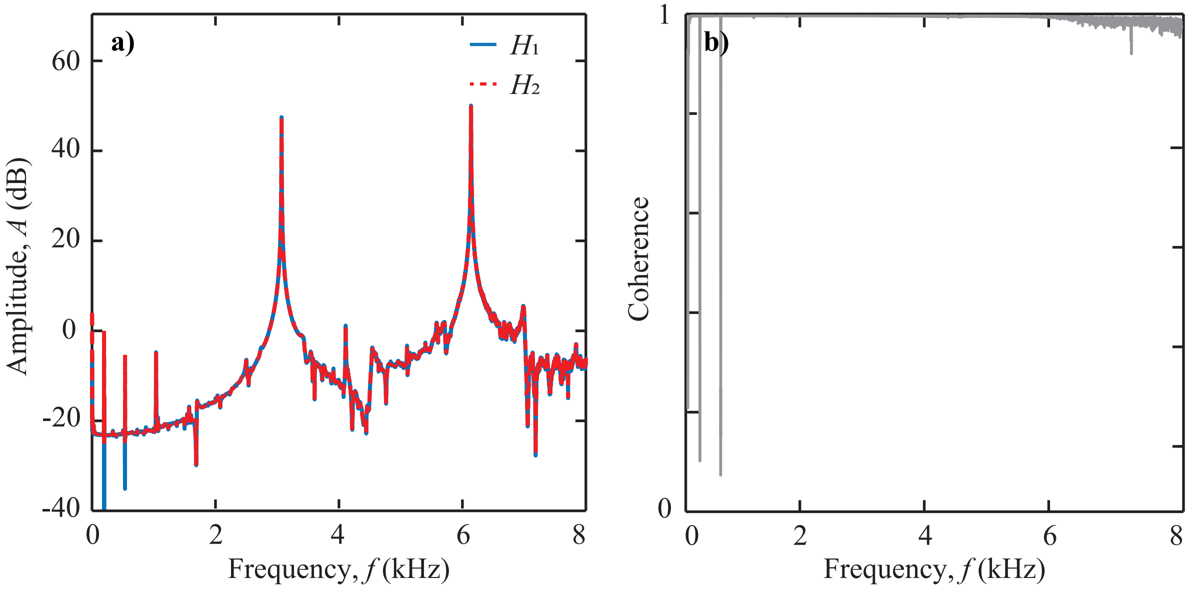

Figure 3.4: **a)** Transfer-function estimators H_1 and H_2, **b)** Coherence function γ.

3.4.2 Numerical Model Curve-Fitted with Experimental Data

The numerical beam geometry is such that $0 \leq x \leq 32$, $0 \leq y \leq 1$, and $0 \leq z \leq 1$ in. The numerical FRF is computed by discretizing the beam geometry using 16,384 3D 8-node brick finite elements, with elasticity parameters $E = 68.9$ GPa, $\nu = 0.33$ and density $\rho = 2700$ kg/m^3. The equation of motion for a forced system with exponential damping is given by

$$\mathbf{M}\ddot{\boldsymbol{u}}(t) + \int_0^t \mu e^{-\mu(t-\tau)}\mathbf{C}\dot{\boldsymbol{u}}(\tau)d\tau + \mathbf{K}\boldsymbol{u}(t) = \boldsymbol{f}(t), \tag{3.16}$$

where $\boldsymbol{u}(t)$ here is redefined to denote the vector of displacements of the finite structure, and $\boldsymbol{f}(t) = \mathbf{F}e^{i\omega t}$ is a harmonic excitation with frequency ω and amplitude $\mathbf{F} = f_j, j = 1, ..., n$, where n is the total number of degrees of freedom. Assuming a time-harmonic response $\boldsymbol{u}(t) = \mathbf{U}(\omega)e^{i\omega t}$ and substituting into Eq. (3.16) yields

$$(\mathbf{K} + i\omega(\frac{\mu}{\mu + i\omega})\mathbf{C} - \omega^2\mathbf{M})\mathbf{U}(\omega) = \mathbf{F}, \tag{3.17}$$

from which the displacement amplitude is calculated as

$$\mathbf{U}(\omega) = (\mathbf{K} + i\omega(\frac{\mu}{\mu + i\omega})\mathbf{C} - \omega^2\mathbf{M})^{-1}\mathbf{F}. \tag{3.18}$$

Finally, the inertance spectrum $\mathbf{Y}(\omega)$ is given by

$$\mathbf{Y}(\omega) = \frac{-\omega^2}{f_{max}}\mathbf{U}(\omega), \tag{3.19}$$

where

$$f_{max} = \max_{j=1,...,n}\{f_j\}. \tag{3.20}$$

Note that for viscously damped system Eq. (3.16) is simply

$$\mathbf{M}\ddot{\mathbf{u}}(t) + \mathbf{C}\dot{\mathbf{u}}(t) + \mathbf{K}\mathbf{u}(t) = \mathbf{0}. \tag{3.21}$$

Therefore the displacement amplitude is given by

$$\mathbf{U}(\omega) = (\mathbf{K} + i\omega\mathbf{C} - \omega^2\mathbf{M})^{-1}\mathbf{F}. \tag{3.22}$$

The sinusoidal force is applied on the axial DOF at location $x = 0,\ y = 0.5,\ z = 0.5$ in and the displacement amplitude is calculated at location $x = 32,\ y = 0.5,\ z = 0.5$ in, which are the excitation and measurements locations of the experimental set-up. The modal damping ratios associated with the two longitudinal resonance frequencies in the range of interest ($0 \leq f \leq 8$ kHz) are extracted using the circle-fit modal analysis technique. We use the code EasyMod [50], which is available online. Using a trial-and-error approach, we vary the prescribed-damping values p, q, and μ in the numerical model until the numerical modal-damping ratios match the experimental ones. Prescribed damping values of $p = 22$, $q = 2.2 \times 10^{-7}$, and $\mu = 10^4$ are found to yield a satisfactory match. Figure 3.5-a compares the experimental inertance spectrum with the numerical one for the curve-fitted damping values $p = 22$, $q = 2.2 \times 10^{-7}$, and $\mu = 10^4$. Figure 3.5-b compares the numerical and experimental modal-damping ratios. For this set of prescribed-damping parameters, the experimental and numerical results show excellent agreement.

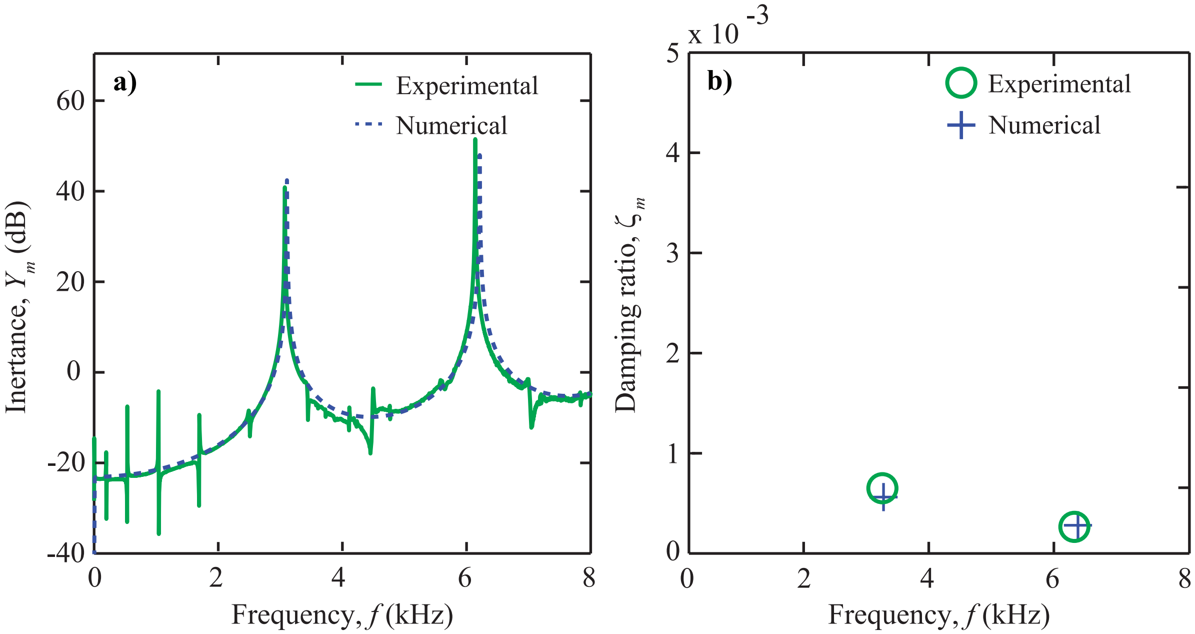

Figure 3.5: **a)** Frequency response functions showing a comparison of experimental and numerical inertance spectra for the first two longitudinal modes, and **b)** corresponding experimental and numerical modal-damping ratios. Y_m and ζ_m represent the inertance and the damping ratio at the measurement point.

3.4.3 Damping Model Based on Experimental Data: Another Application

The procedure described in the previous subsections is applied here to select viscous damping parameters for ABS plastic [53]. The experimental set-up is similar to that of section 3.4.1: the ABS beam is suspended using nylons cords and hit with the modal hammer at a location 2 inches from one end and exactly halfway up. This excites flexural modes in the horizontal plane and avoids torsional and longitudinal modes. Velocities are measured with a vibrometer laser (Polytec PDV 100) on the opposite face from the impulse at a location 12 inches from the same end and halfway up. The measurements are collected with a Polytec VIB-E-220 data acquisition system (the frequency rate is set to 9.6 kHz and the sample time is 3.2 s). The experimental mobility spectrum is obtain by post-processing the time data on MATLAB.

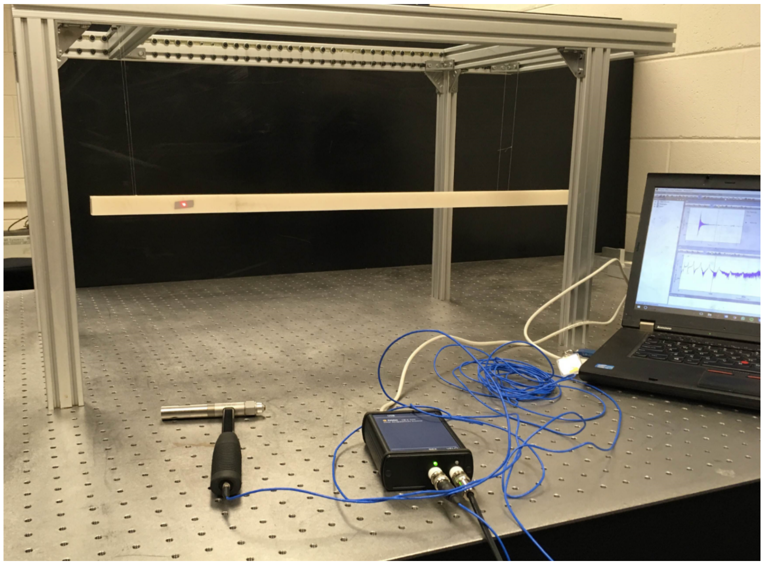

Figure 3.6: Experimental set-up for extraction of viscous damping properties of an ABS structure.

The numerical FRF is computed by discretizing the experimental beam using the finite-element method with 16,384 3D 8-node, iso-parametric elements. The damping matrix $\mathbf{C}$ is constructed assuming stiffness-proportional damping $\mathbf{C} = q\mathbf{K}$, where $\mathbf{K}$ is the stiffness matrix and q the viscous damping parameter. The numerical mobility spectrum is given by

$$\mathbf{H}(\omega) = i\omega\mathbf{X}(\omega). \tag{3.23}$$

We extract the modal damping ratios associated with the five resonance frequencies in the range of interest (0-1 kHz). To find a viscous-damping parameter q that leads to realistic level of dissipation in the material, we compare the numerical and experimental modal-damping ratios. Using a trial-and-error approach, we vary q in the numerical model until the first five flexural modal damping ratios approximately match the experimental values. A prescribed damping value of $q = 5 \times 10^{-6}$ is found to produce a reasonable match. Figure 3.7 compares the experimental FRF with the numerical FRF using the curve-fitted damping value ($q = 5 \times 10^{-6}$). The corresponding damping ratios for the two FRFs are shown in Fig. 3.7-b.

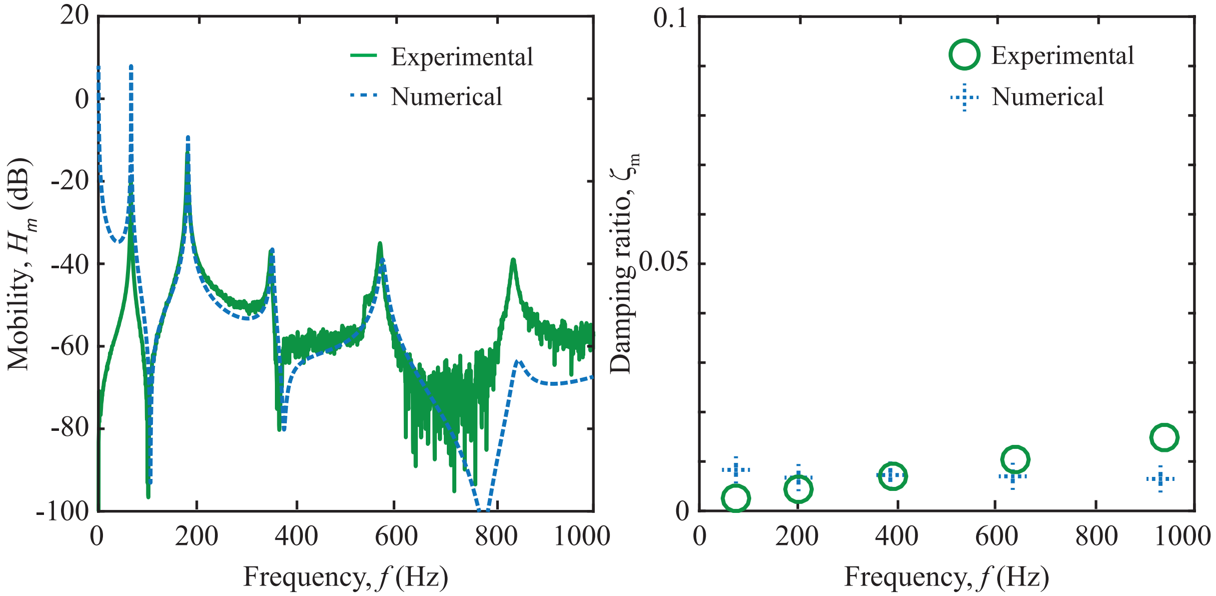

Figure 3.7: **a)** Frequency response functions showing a comparison of experimental and numerical mobility spectra for the first five bending modes, and **b)** corresponding experimental and numerical modal-damping ratios. Y_m and ζ_m represent the mobility and the damping ratio at the measurement point.

3.5 Dispersion Analysis of 3D Beam Unit Cells with Viscous and Viscoelastic Damping

In this section, two beam unit cells are considered: a regular beam unit cell referred to as *unpillared* and a beam unit cell with a square pillar on top, referred to as *pillared*. (The pillar act as a local resonator.) Both unit cells are depicted on Fig. 3.8 (the dimensions are given in inches).

The mass $\mathbf{M}$ and stiffness $\mathbf{K}$ matrices are obtained upon discretization of the equations of motion with 4,096 and 4,352 3D brick elements, respectively. The damping matrix is obtained

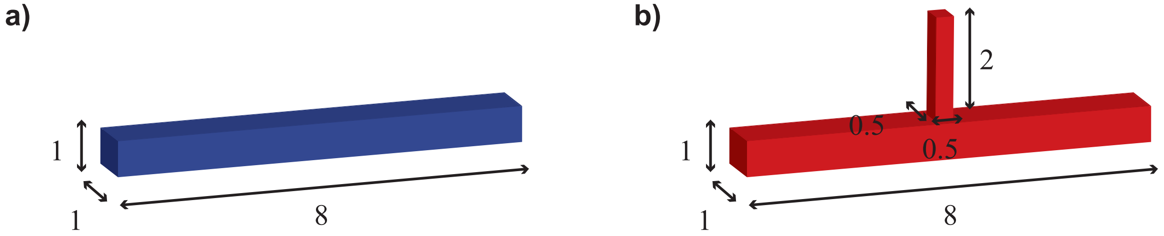

Unpillared

Pillared

Figure 3.8: Models of the **a)** unpillared and **b)** pillared unit cells. Dimensions are given in inches.

following the procedure described in the previous section. Bloch periodicity is enforced in one direction, along the longitudinal axis. Dispersion and damping-ratio diagrams are obtained for three different levels of prescribed damping and for both damping models: viscous and viscoelastic. The damped dispersion and damping-ratio diagrams for both unit cells are shown in Figs. 3.9 and 3.10 if viscous damping is assumed and in Figs. 3.11 and 3.12 if viscoelastic damping is assumed..

As the level of prescribed damping is increased, the band structure is altered more profoundly. The phenomenon of *branch cut-off* can be observed [38], i.e., the branches get cut off in the wavenumber domain and do not span the entire Brillouin zone. Moreover, it is important to note that the two types of damping alter the dispersion curves differently; with viscous damping, as the levels of prescribed damping are increased, the dispersion branches shift down in frequency, whereas, with the viscoelastic damping model, they shift up.

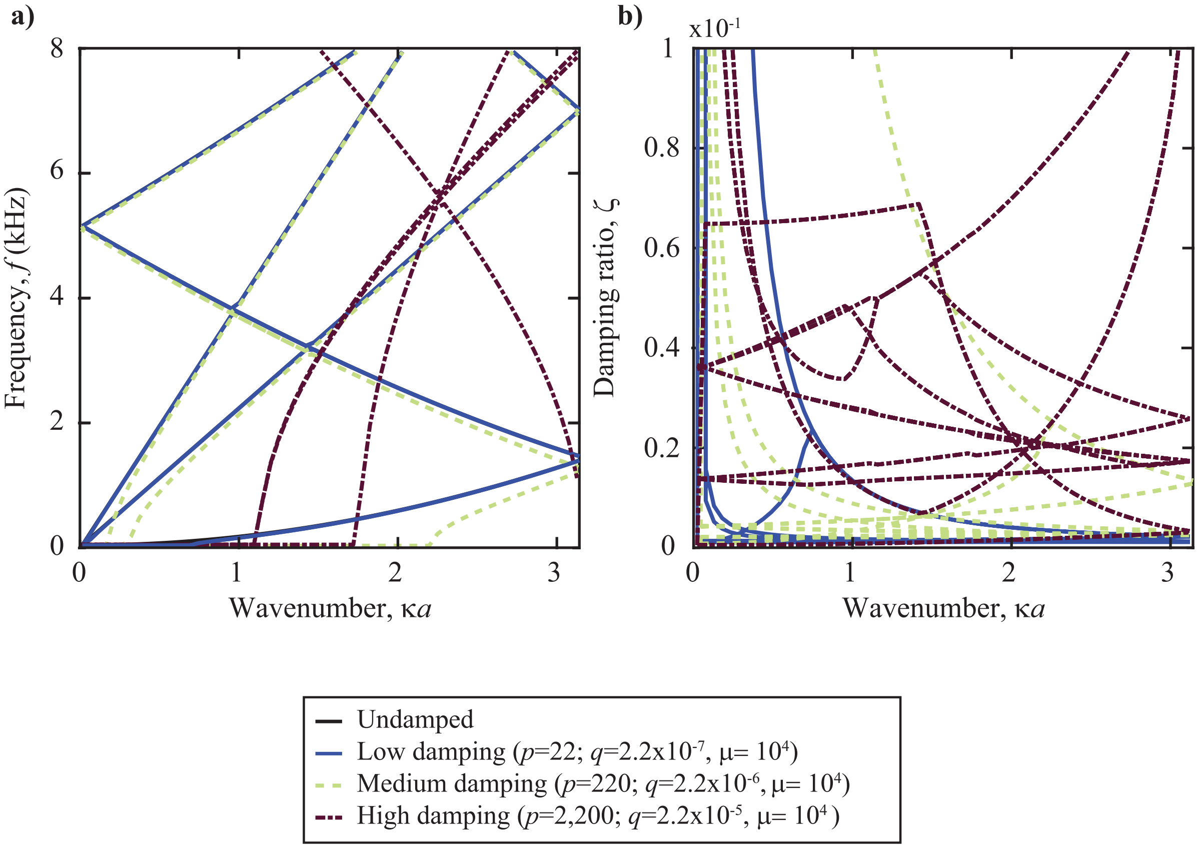

Figure 3.9: *Viscous damping model-Unpillared.* **a)** Dispersion diagram and **b)** damping-ratio diagram of the unpillared beam unit cell for three levels of prescribed damping (low, medium, high).

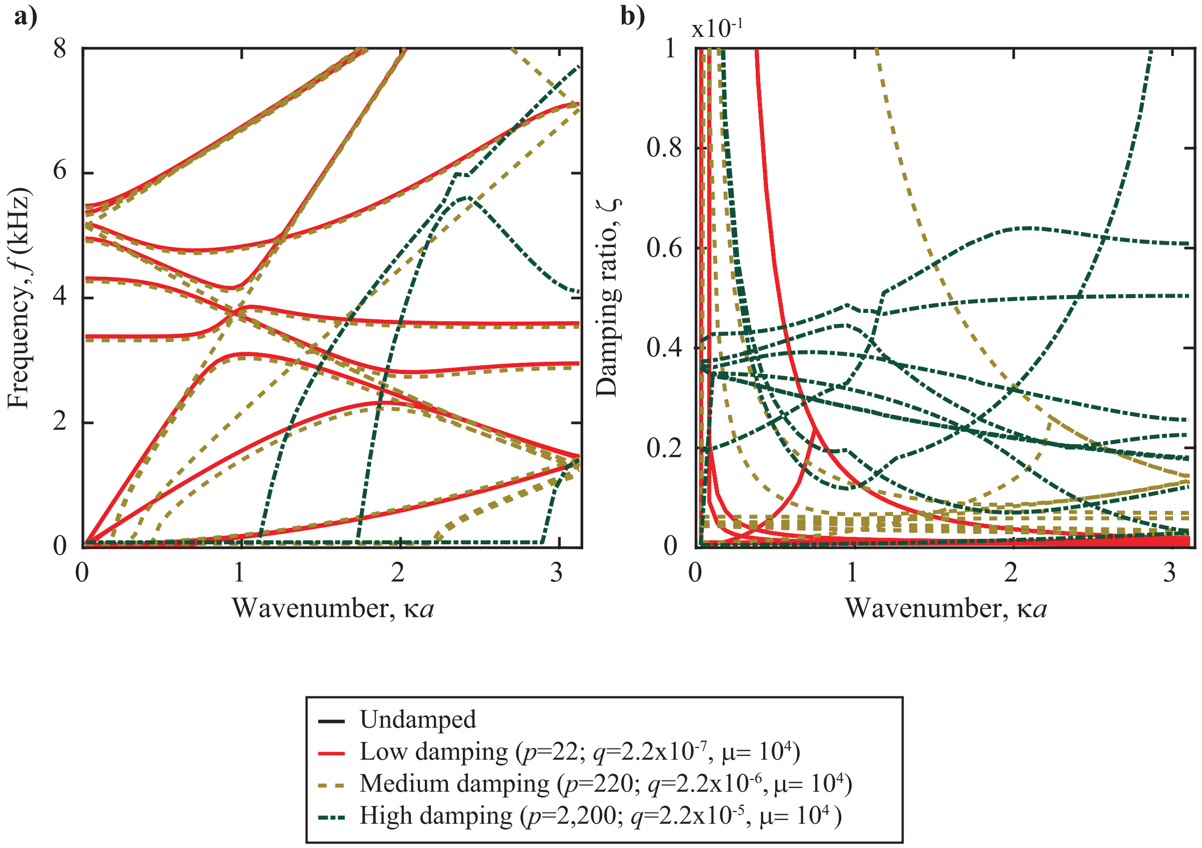

Figure 3.10: *Viscous damping model-Pillared.* **a)** Dispersion diagram and **b)** damping-ratio diagram of the pillared beam unit cell for three levels of prescribed damping (low, medium, high).

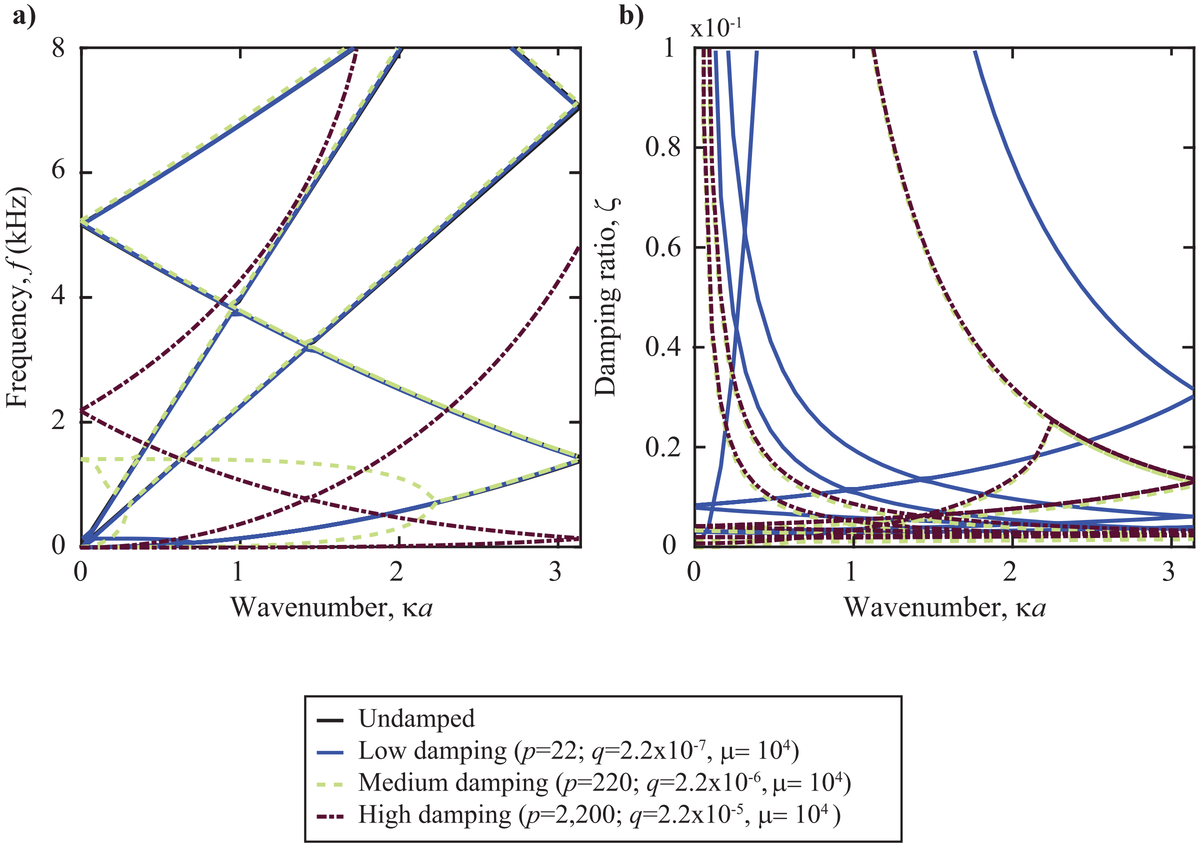

Figure 3.11: *Viscoelastic damping model-Unpillared.* **a)** Dispersion diagram and **b)** damping-ratio diagram of the unpillared beam unit cell for three levels of prescribed damping (low, medium, high).

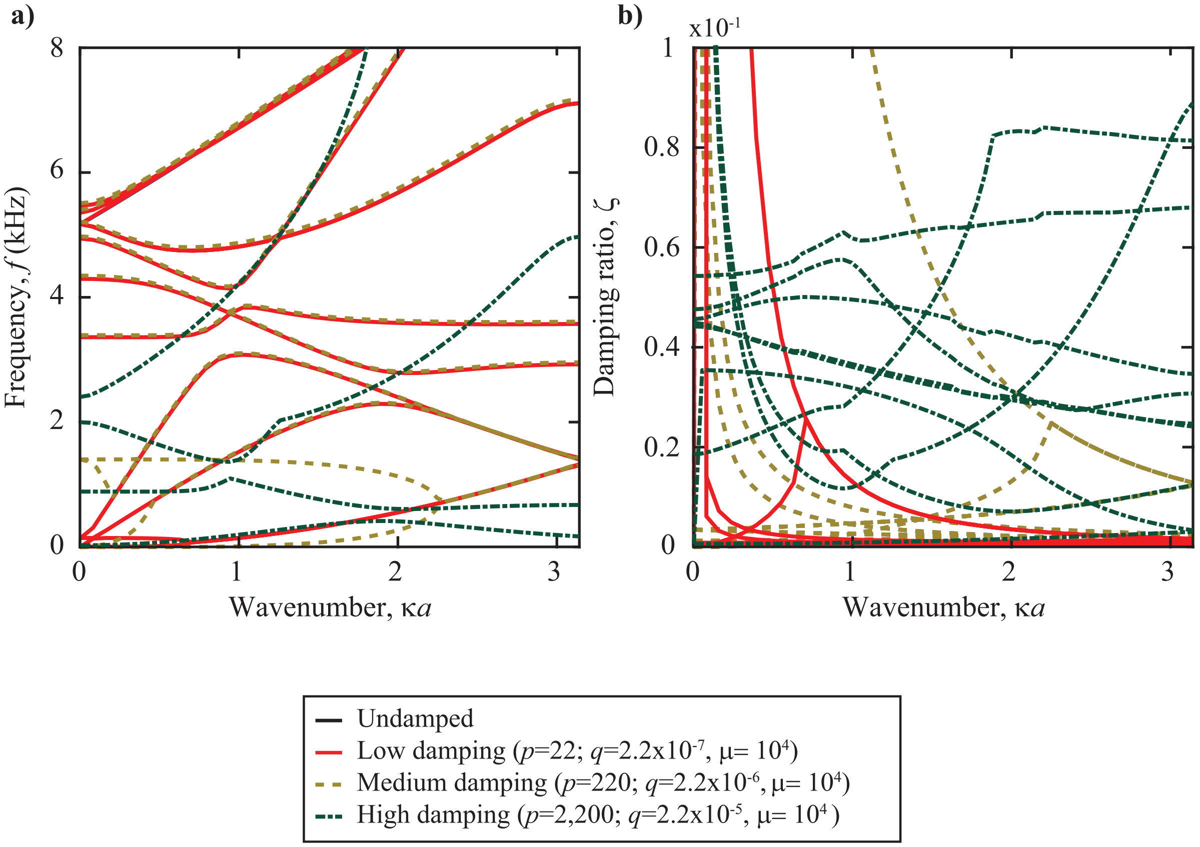

Figure 3.12: *Viscoelastic damping model-Pillared.* **a)** Dispersion diagram and **b)** damping-ratio diagram of the pillared beam unit cell for three levels of prescribed damping (low, medium, high).

Chapter 4

Metadamping: Dissipation Engineering by Elastic Metamaterials in Free-Wave Propagation

4.1 Introduction

In many engineering applications where materials exhibiting both high stiffness and high loss are highly desirable, metadamping offers an appealing solution to the classic stiffness/damping trade-off. Despite promising results, the concept of metadamping has only, as of today, been shown in the context of 1D spring-mass systems and in theory [8, 20, 40]. In order for this concept to leave the realm of fundamental science and be used in practice by engineers, it first needs to be proven experimentally. In this section, we demonstrate the realization of metadamping in an experimental system. We examine the dissipation levels of a 3D beam with a local array of square pillars (which act as local resonators) and compare them to the dissipation levels of an equivalent *unpillared* beam. First, we demonstrate the realization of metadamping in finite structures, both experimentally and numerically. Then, we carry out a dispersion analysis at the unit-cell level and establish a relation between the damping ratios derived from the unit-cell analysis and those derived from modal analysis on the finite system. In other terms, we relate the wave-propagation problem to the vibration problem. Based on this relation, we lay out a theoretical description for the concept of metadamping and successfully show, through numerical experiments, that we can engineer dissipation in elastic metamaterials in the context of free waves. We perform a parametric study and show the effects of pillar spacing on metadamping. Finally, we provide a rigorous mathematical description for metadamping in a locally resonant rod.

4.2 Evidence of Metadamping in an Experimental System

4.2.1 Experimental Set-Up

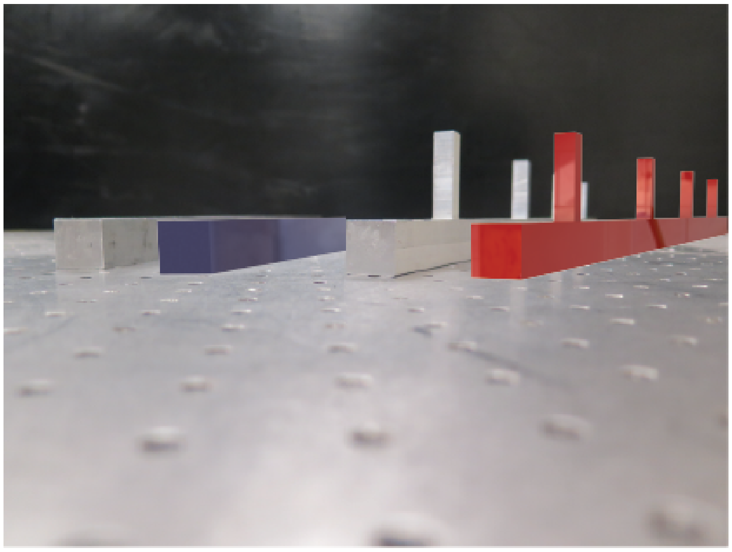

Figure 4.1: Photograph of the experimental systems and their equivalent numerical systems.

As illustrated in Fig. 4.1, the two test structures are aluminum beams, referred to as unpillared and pillared. The unpillared beam has for dimensions 32 × 1 × 1 inches and is made of aluminum. The pillared beam is composed of four periodic unit cells of dimensions 8 × 1 × 1 inch along the axial direction, where each unit cell consists of a square pillar of dimensions 0.5 × 0.5 × 2 inch on top of the beam. In order to solely focus on the effects of the pillar on damping and minimize the variables involved, the pillars were not attached to the main beam using glue. Instead, the pillared beam was manufactured by milling a beam of dimensions $32 \times 1 \times 3$ inch with a CNC milling machine. The experimental time responses are obtained following the procedure described in 3.4.1. For convenience, we provide here a brief summary. Each beam is suspended using nylon cords in order to simulate free-free boundary conditions. An accelerometer (PCB WJ35C65) is fixed on one of the ends of the beam, at the center point of the cross-section. Impulsive excitations are applied with an impact hammer (PCB 086C02) at a point located at the center of the opposite cross-section, such that only the longitudinal modes are excited and measured. The acceleration responses are collected with a NI-DAQ 9234 for 10s. FRFs for both beams are obtained by post-processing the time data on MATLAB (see section 3.4.1 for more details).

4.2.2 Numerical Model

Numerical FRFs are obtained by modeling the experimental beam geometries using 16,384 and 16,896 3D 8-node brick finite elements, with elasticity parameters $E = 68.9$ GPa, $\nu = 0.33$ and density $\rho = 2700$ kg/m^3. Viscoelastic damping is applied to the numerical model following the procedure described in chapter 3. The proportional damping parameters p, and q, as well as the viscoelastic damping constant μ are found by curve-fitting the experimental and numerical modal-damping ratios (see 3.4.2 for more details). Prescribed damping values of $p = 22$, $q = 2.2 \times 10^{-7}$, and $\mu = 10^4$ are found to produce a satisfactory match (see Fig. 4.2). The numerical time responses are obtained by implementing the direct time integration method for exponentially damped systems

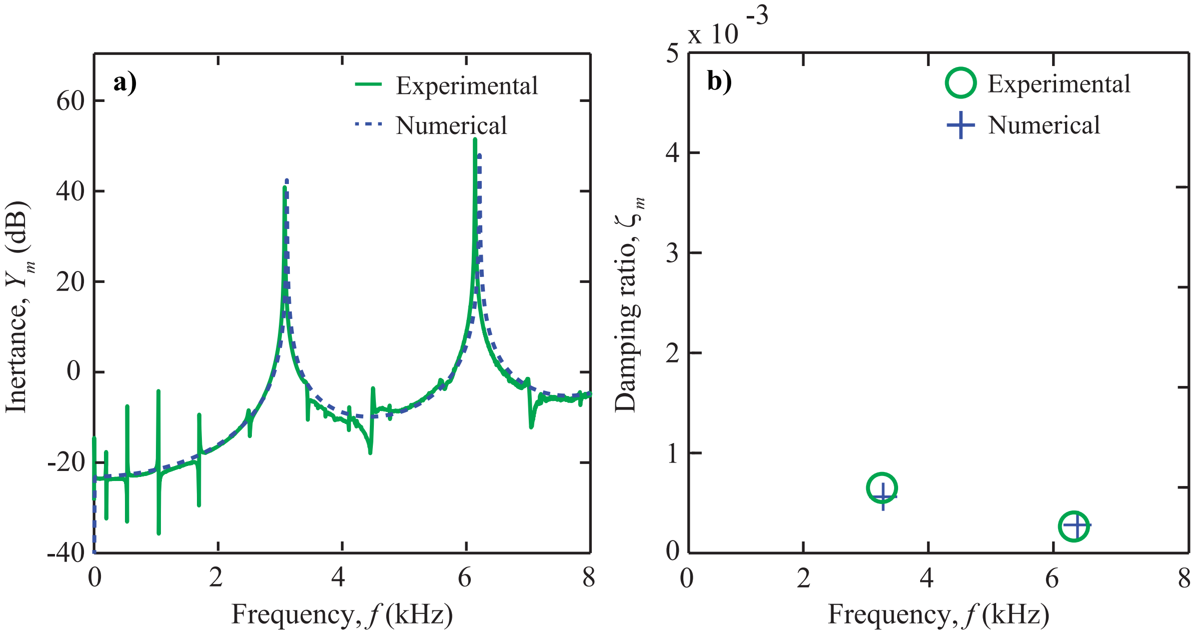

Figure 4.2: **a)** Frequency response functions (FRFs) showing a comparison of the experimental and numerical inertance spectra, and **b)** corresponding experimental and numerical modal-damping ratios.

described in [3]. As in laboratory testing, an initial displacement is applied at the center of the cross-section on one end of the beam along the longitudinal axis, and the displacement is calculated at a point located at the center of the opposite cross-section. The simulation is run for a total time of $t = 0.4$ s with a time step of $\Delta t = 3 \times 10^{-5}$ s. To further simulate the experimental set-up, the initial displacement is modeled as a Gaussian excitation whose parameters a and b are selected such that it matches the experimental impulse:

$$u_0(t) = e^{-\frac{(t-a)^2}{2b^2}}, \tag{4.1}$$

where $a = 0.01$ and $b = 8 \times 10^{-5}$.

4.2.3 Metadamping Quantification

Fig. 4.3-c shows the time series obtained for both beams in response to impulsive excitations applied on the longitudinal axis. The excitation profiles are shown in the insets. Note that order to fairly compare the time series of both experimental structures, we had to ensure that the excitation impulses had the same amplitude; therefore, multiple excitations were applied on each beam until two measurements providing a satisfactory match were obtained. To quantify the temporal attenuation in each beam, and hence, get information about their dissipation levels, we compare the time decays, which we obtain using the following procedure. We take the first derivative of the displacement response and we extract the extrema, which are the points where the derivative changes signs. They are referred to as *response peaks.* We curve-fit exponential functions of the form $f(t) = ae^{-bt}$, where b is the exponential decay constant, to the response peaks using MATLAB curve-fitting tool.

The ratio $r = b_{\text{pillared}}/b_{\text{unpillared}}$ is defined as an indicator of metadamping. A ratio greater than unity signifies *positive metadamping*, i.e., the time response of the pillared beam decays faster than that of the unpillared beam. Conversely, a ratio less than unity indicates *negative metadamping*, i.e., the time response of the pillared beam decays slower than that of the unpillared beam.

A ratio of $r_{\text{exp}} = 1.49$ is found for the experimental time decays, hence suggesting that the

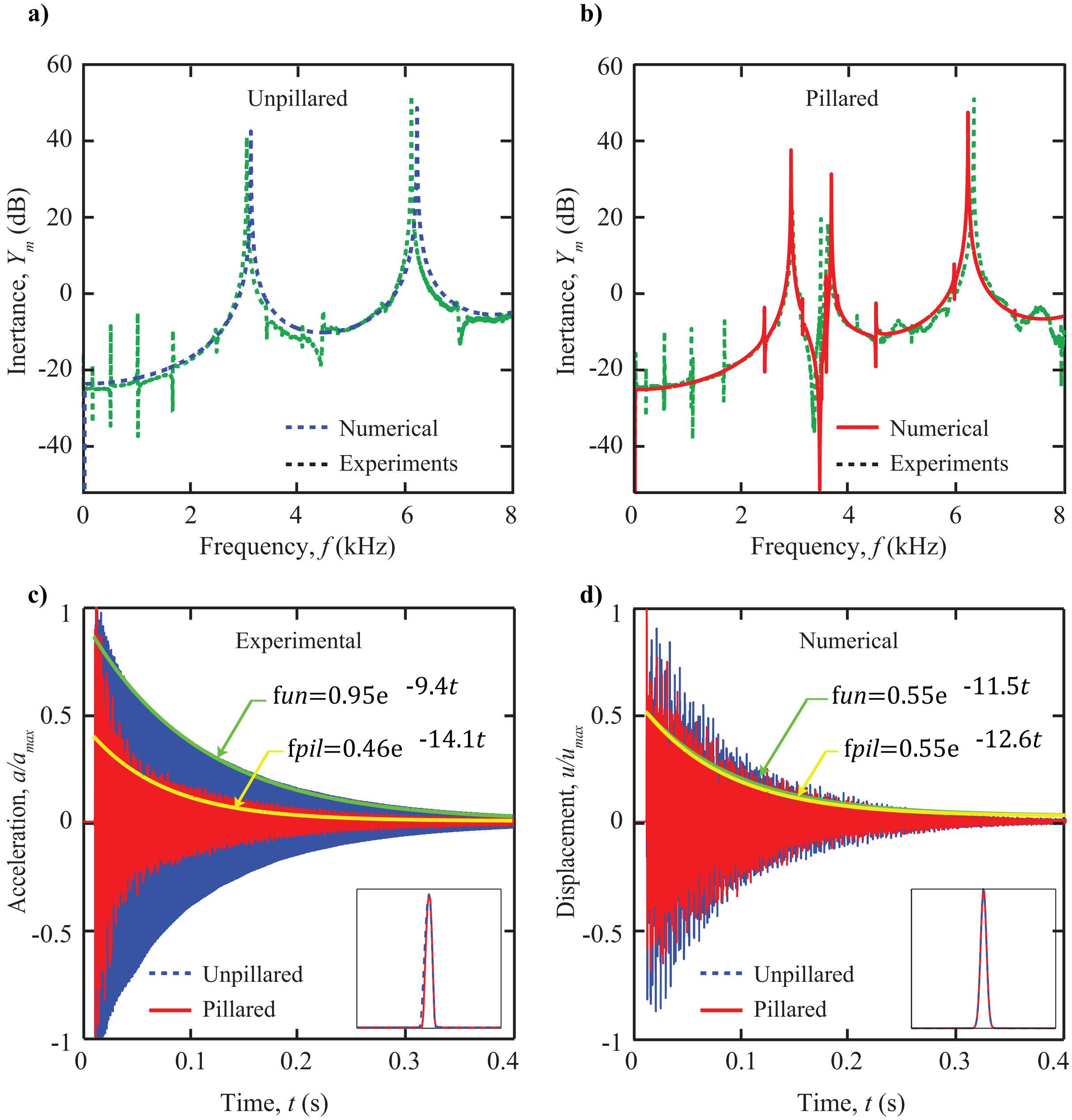

Figure 4.3: *Finite-structure response*, Numerical and experimental FRFs for the **a)** unpillared and **b)** the pillared beam. **c)** Experimental **d)** and numerical time responses for the two beams. The yellow and green curves correspond to exponential curves that were fitted to the unpillared and pillared time signals, respectively, to determine their time decays. The impulsive excitations are shown in the insets.

pillared beam exhibits higher dissipation levels than the unpillared one. To support the experimental findings, a numerical experiment is performed : the numerical ratio $r_{\text{num}} = 1.09$ follows the same trend, supporting the positive metadamping hypothesis.

4.3 Dispersion Analysis

In elastic metamaterials, local resonances interfere with the dispersion curves of the underlying medium and can alter the spatial attenuation characteristics by creating band gaps, which are frequency range through which no wave is allowed to propagate. Here, the idea that local resonances can affect the temporal attenuation instead is investigated; therefore, a dispersion analysis at the unit-cell level is performed to comprehensively describe and analyze this concept. Figure 4.4 depicts the unpillared and pillared unit cells; dimensions are in inches. The damped band structure and damping-ratio diagrams are plotted in Figs. 4.5-a and b, respectively, for both unit cells (see chapter 3 for details). For clarity, we denote the first four beam branches in the dispersion diagram–corresponding to the flexional, torsional, transverse and longitudinal beam modes, respectively [48]–as well as their equivalent branches in the damping-ratio diagram.

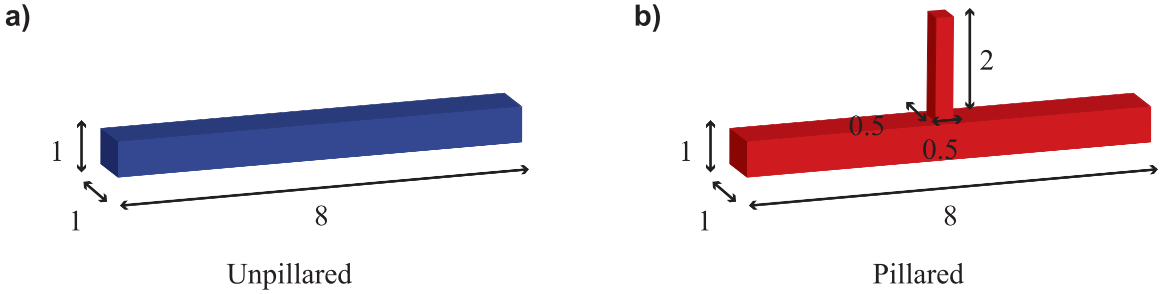

Figure 4.4: Models of the **a)** unpillared and **b)** pillared unit cells. Dimensions are given in inches.

4.3.1 Relation between the Vibration and Wave-Propagation Problems

Numerous studies on phononic materials have established a relation between the dispersion analysis of the unit cell and the FRF of the finite structure [41, 119]. For example, a band gap in

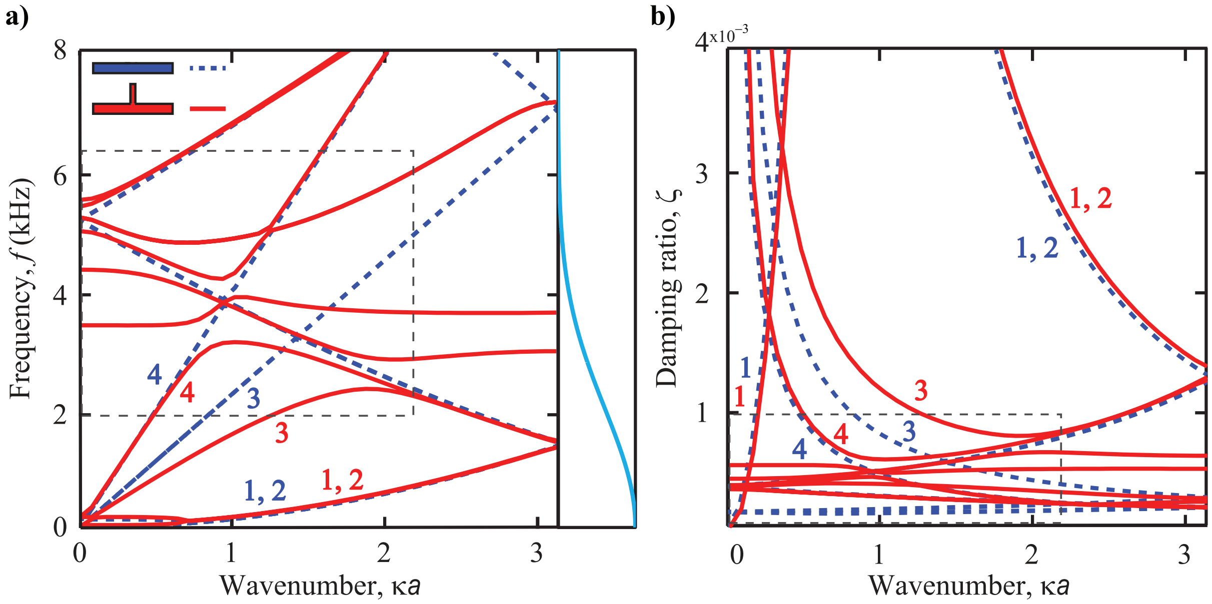

Figure 4.5: *Unit-cell analysis. a),* Dispersion diagram for the unpillared (dashed blue) and pillared (red) unit cells. The first four branches corresponding to the flexional, torsional, transverse and longitudinal modes of the beam are identified. The frequency content of the impulsive excitation excitations is depicted in the inset. **b)**, Damping-ratio diagram. The first four damping branches are identified. The insets in **a)** and **b)** are the close-up views used in Figure 4.6.

the dispersion diagram will materialize by low amplitude levels in the FRF of the finite structure. However, no such relation has been shown between the damping-ratio diagram of the unit cell and the modal damping ratios of the finite system. Fig. 4.6 demonstrates that the vibration (or finite) problem can be related to the wave-propagation (or infinite) problem in the context of damped wave propagation. For each resonance frequency in the FRF (Fig. 4.6-a), the modal damping ratios shown in Fig. 4.6-c are obtained using a circle-fit technique [23, 50]. Then, each of these resonance frequencies is projected onto the dispersion diagram and the corresponding wavenumber(s) are determined. Lastly, the modal damping values of Fig. 4.6-c are projected onto the damping-ratio diagram. The damping parameters p, q and μ, which were selected with experimental curve-fitting, are adjusted until the modal-damping ratios fall on the right spot on the damping-ratio diagram (see Fig. 4.6-d). We devised here a new procedure to close the loop between the infinite and finite analysis and were able to develop a damping model which accurately predicts dissipation within

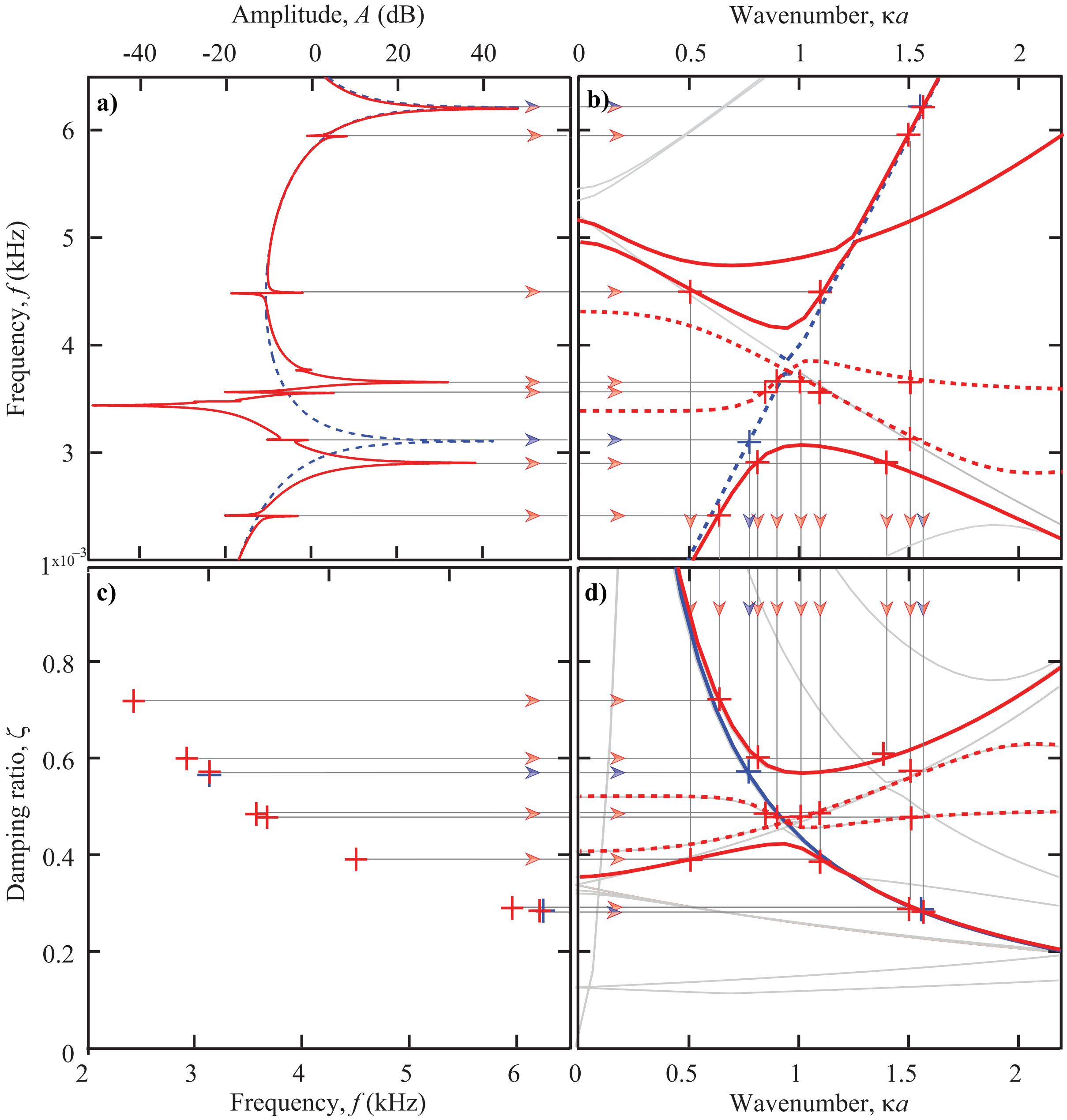

Figure 4.6: *Relation between the finite-structure and unit-cell analyses* ***a)*** Numerical FRFs for the unpillared (dashed blue) and pillared (red) beams. **b**) Dispersion diagram. For clarity, only the longitudinal modes are highlighted, the other modes are shaded. **c)** Modal-damping ratios for the finite structure obtained using a circle-fit technique. **d)** Damping-ratio diagram. For clarity, only the longitudinal modes are highlighted, the other modes are shaded.

the dispersion analysis framework.

4.3.2 Positive and Negative Metadamping

We conduct a numerical experiment to show that depending on the frequency content of the impulsive excitation, dissipation can be engineered for both its maximization or reduction. For the case presented earlier in this chapter (see Fig. 4.1), the frequency content of the excitation falls into the positive metadamping region, which ranges from 2.5 to 3.75 kHz (see blue line in inset of Fig. 4.7-a). The blue arrows in the dispersion diagram represent the displacement of the dispersion curves due to the introduction of a pillar. That effect is mapped onto the damping-ratio diagram (see Fig. 4.7-b), and it can be seen that, for those same points, the damping ratio has increased, hence supporting the positive metadamping observed in the finite structure (Fig. 4.5). It has been shown by theory and experiments, that local resonances with proper tuning and under certain conditions can actually enhance dissipation in the medium without adding more damping to the medium.

In principle, the opposite effect can be demonstrated; therefore, the existence of negative metadamping, i.e., decreasing the dissipation in the medium by adding a pillar, is investigated next. The black arrows in the dispersion diagram represent the displacement of the dispersion curves due to the pillar in a different frequency region (3.75-4.5 kHz). Again, those arrows are mapped onto the damping-ratio diagram, and this time the damping ratio has decreased. In order to test that hypothesis, the impulsive excitation is tailored such that its frequency content falls into our 'suspected' negative-metadamping region, i.e., 3.75-4.5 kHz (see black dashed line in Fig. 4.7-b). The Gaussian excitation of Eq. 4.1 becomes

$$u_0(t) = e^{-\frac{(t-a)^2}{2b^2}} e^{ict}, \tag{4.2}$$

where $a = 0.01$, $b = 3 \times 10^{-4}$, $c = 2.5 \times 10^{-4}$. The response extrema and time decays are obtained and shown on Fig. 4.7-d. (For reference, the response peaks and time decays are shown in Fig. 4.7-c. A metadamping ratio of $r_{\text{num}} = 0.84$ is found, which indicates that the pillared time response decays slower than the unpillared one, thus indicating the existence of negative metadamping.

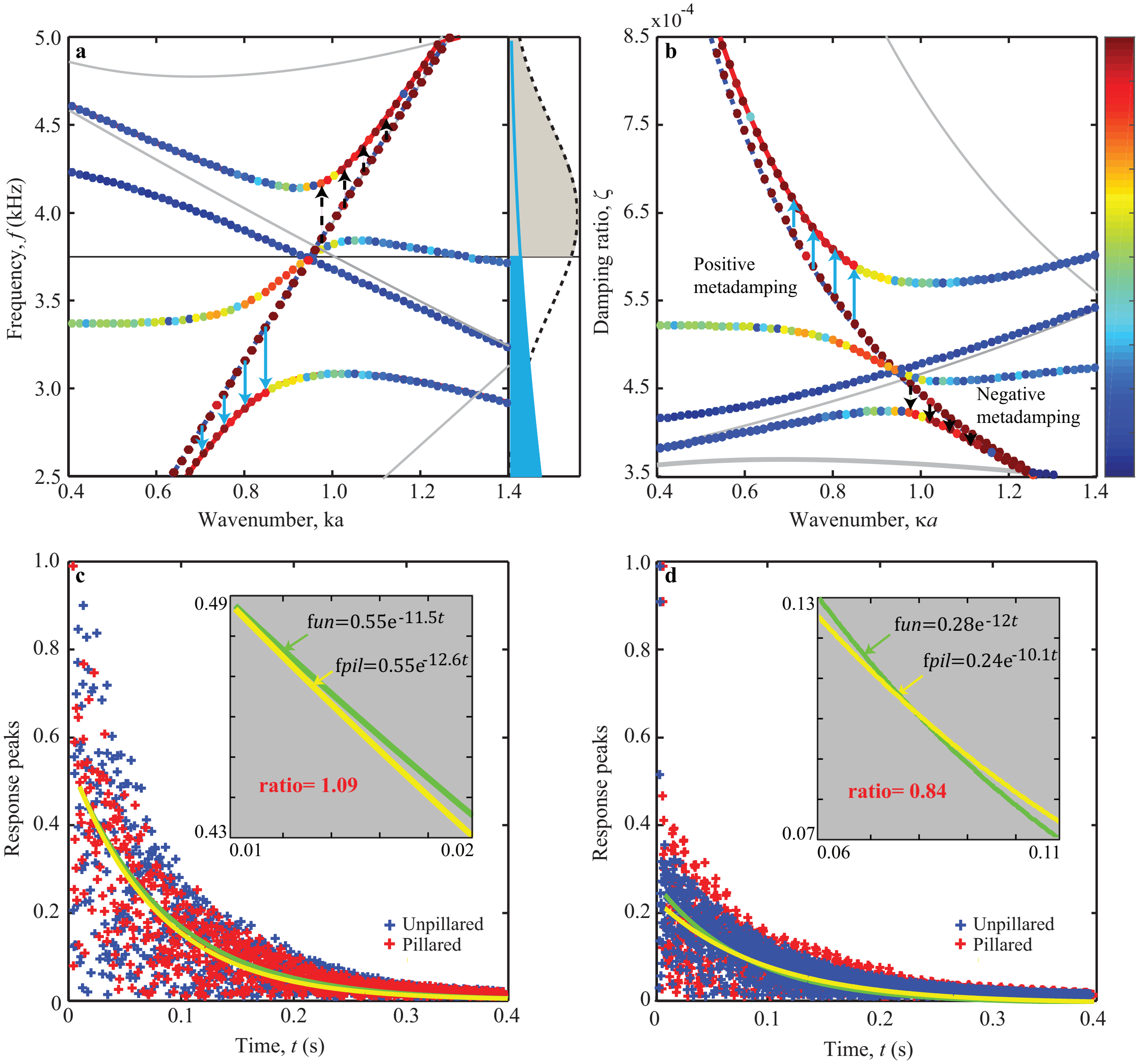

Figure 4.7: *Evidence of metadamping. a)* Dispersion diagram with a close-up view of the hybridization region. The color bar represents the degree longitudinal polarization. The inset shows the frequency content of the two impulsive excitations. The solid blue arrows (resp. dashed black arrows) represent positive (resp. negative) metadamping. **b)** Corresponding damping-ratio diagram. **c-d)**, Response peaks of the unpillared (blue) and pillared (red) time signals showing **c)** positive and **d)** negative metadamping. The insets show a close-up of the fitted exponential curves (green for unpillared, yellow for pillared).

4.4 Parametric Design Study: Effects of Pillar Spacing on Metadamping

We perform a parametric study and vary the unit-cell length to determine how the spacing of the pillars affects metadamping (positive and negative). We define the two metadamping metrics D_p and D_n to help quantify the amount of positive and negative metadamping in the unit cell. The procedure to obtain these metrics is as follows. First, the Bloch modes are sorted using the MAC criterion. Then, the damping branches corresponding to the longitudinal modes are identified in the damping-ratio diagram by computing the longitudinal polarization for each Bloch mode. According to [2], the amount of polarization along the longitudinal axis is given by

$$p_x = \frac{\int |u_x|^2 dr}{\int (|u_x|^2 + |u_y|^2 + |u_z|^2) dr}, \tag{4.3}$$

where u_x, u_y, and u_z are the displacement fields along the x, y, and z directions. The integral in Eq. (4.3) is taken over the unit cell. For the unpillared beam, the longitudinal mode consists of only one branch, whereas for the pillared beam, we extract two branches corresponding to the equivalent longitudinal mode. They are referred to as upper branch (associated with positive metadamping) and lower branch (associated with negative metadamping). We define the positive (resp. negative) metadamping metric as the area encompassed between the unpillared branch and the upper (resp. lower) pillared branch, and between the left (resp. right) and middle boundary lines. The left and right boundary lines are drawn at the wavenumbers for which the ratio between the pillared and unpillared damping ratios differ by 5% such that

$$\delta = \frac{|\zeta_{pil} - \zeta_{unp}|}{\zeta_{unp}} \times 100 = 5. \tag{4.4}$$

The middle line is drawn such that it passes through the extrema of the two pillared branches. The wavenumbers at which these extrema occur are determined using the curvature (second derivative, see insets on Fig. 4.8). In order to ensure accuracy in the area calculation of the two metadamping regions, linear interpolation is performed along the wavenumber axis on the unpillared and pillared branches, between the left and right boundary lines. The areas are then calculated by slicing the two metadamping regions into quadrilaterals between consecutive wavenumbers and summing their areas. The formula used to find the area of each quadrilateral is as given by

$$\begin{aligned} area =& \frac{1}{2}|(x_1y_2 - x_2y_1) + (x_2y_3 - x_3y_2) \\ &+ (x_3y_4 - x_4y_3) + (x_4y_1 - x_1y_4)|, \end{aligned} \tag{4.5}$$

where $x_1 = x_4 = \kappa_i$ and $x_2 = x_3 = \kappa_{i+1}$ are consecutive wavenumbers, y_1 and y_2 are the unpillared damping-ratio values, and y_3 and y_4 are the pillared damping-ratio values. Figure 4.8 shows a summary of the procedure for a unit cell with length $a = 6$ in. The positive metadamping region is highlighted in blue and the negative metadamping one in black.

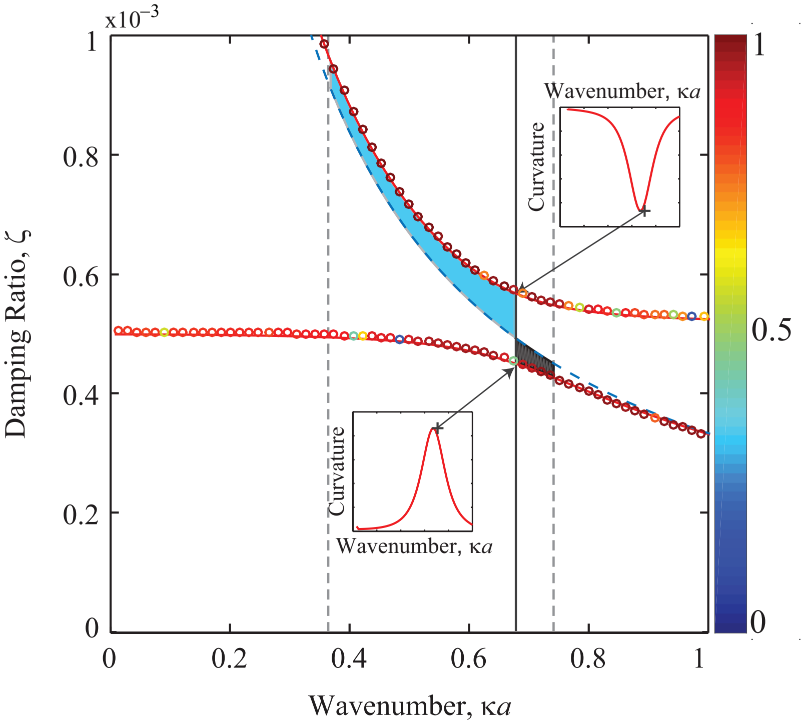

Figure 4.8: *Metadamping metric calculation for* $\boldsymbol{a = 6}$ The left and right boundary lines (dashed grey) are drawn at the wavenumbers for which the difference between the unpillared and pillared damping ratios is 5%. The middle line is drawn such that it passes through the extrema of both pillared damping branches (the curvature or second derivative for both branches are shown in the insets). The value of the positive metadamping metric D_p (resp. negative metadampig metric D_n) is derived by calculating the area of the region shaded in blue (resp. black). The color bar indicates the level of longitudinal polarization: values range from 0 (pure shear) to 1 (pure longitudinal).

Figure 4.9 shows the evolution of the metadamping metrics as a function of the unit-cell length a. As expected, both metrics follow a decreasing trend for increasing unit-cell lengths a.

Indeed, for longer unit cells, the coupling between the pillars becomes weaker, hence leading to a reduced effect on the damping in the main structure. It is interesting to note that positive metadamping especially is affected by the length of the unit cell, as D_p decays at a greater rate than D_n for increasing a.

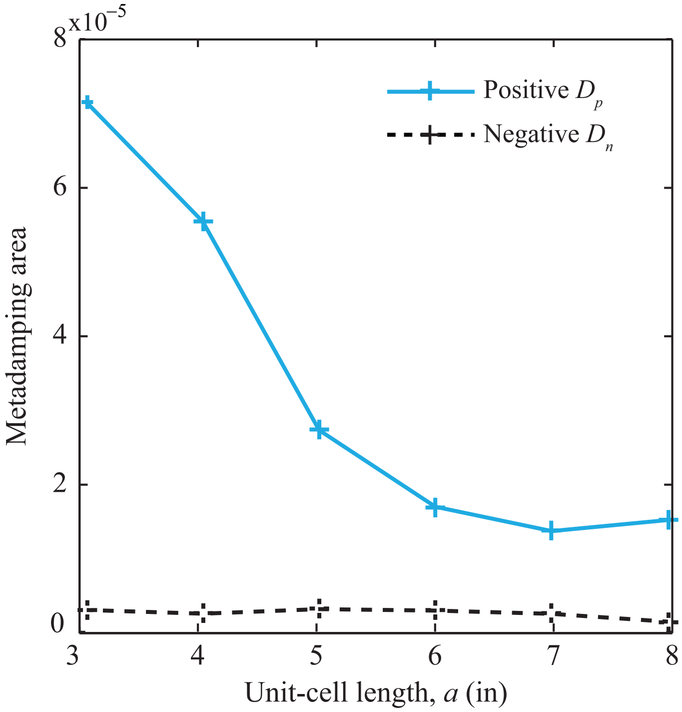

Figure 4.9: *Parametric study: effects of the pillar-spacing on metadamping.* Positive (blue) and negative (black) metadamping metrics as a function of the unit-cell length a.

4.5 Effects of Added Mass on the Damping-Ratio Diagram

We want to ensure that the added mass of the pillar is not a factor into our metadamping study. The pillared beam has a volume of $V_{pil} = 34$ in^3 whereas the unpillared beam has a volume of $V_{pil} = 32$ in^3. Therefore, to show that the metadamping is due to local resonance phenomena only, and not added mass, we perform a similar analysis as that of Fig. 4.3-d on an unpillared beam that has the same volume as the pillared beam. Numerical time responses and their curve-fitted exponential functions are shown on Fig. 4.10. The metadamping ratio, here redefined as $r = b_{\text{unpillared}_{\text{vol}}}/b_{\text{unpillared}}$, is unity as expected. This analysis supports our thesis that metadamping emerges from the presence of local resonance and not from the addition of damped material.

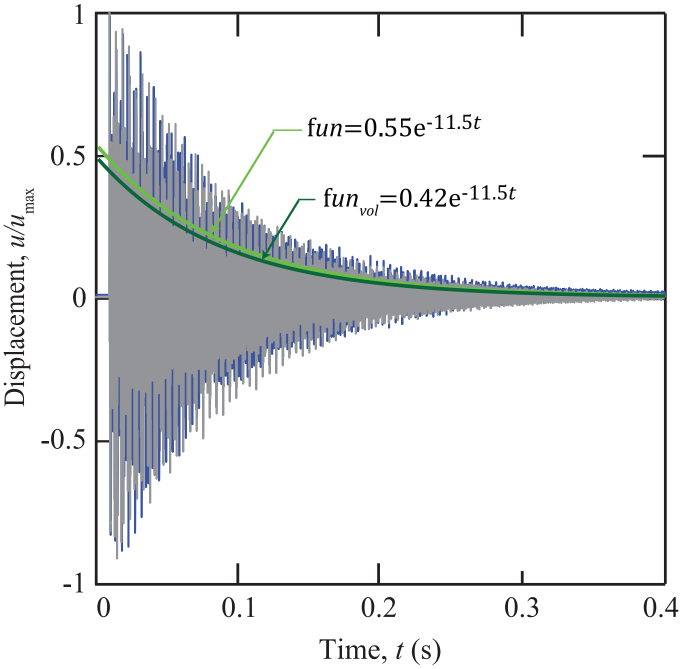

Figure 4.10: *Numerical time responses* for the two unpillared beam with volumes $V = 32$ in^3 (blue) and $V = 34$ in^3 (grey). The light and dark green curves correspond to exponential curves that were fitted to the unpillared and unpillared volume time signals, respectively, to determine their time decays.

4.6 Bounds on Positive and Negative Metadamping

In this section, we develop a mathematical framework to further investigate positive and negative metadamping in the context of free-wave propagation. To that end, we analytically describe the temporal attenuation of longitudinal waves in a locally resonant rod. We follow the work by Maznev [72] who, in a recent publication, analytically investigated the avoided crossing of the optical and acoustic branches in a locally resonant acoustic medium, as a function of the oscillator damping and oscillator interaction strength. We extend here his analysis, and determine the bounds on the prescribed damping η for the locally resonant rod to exhibit positive and negative metadamping over the whole wavenumber range.

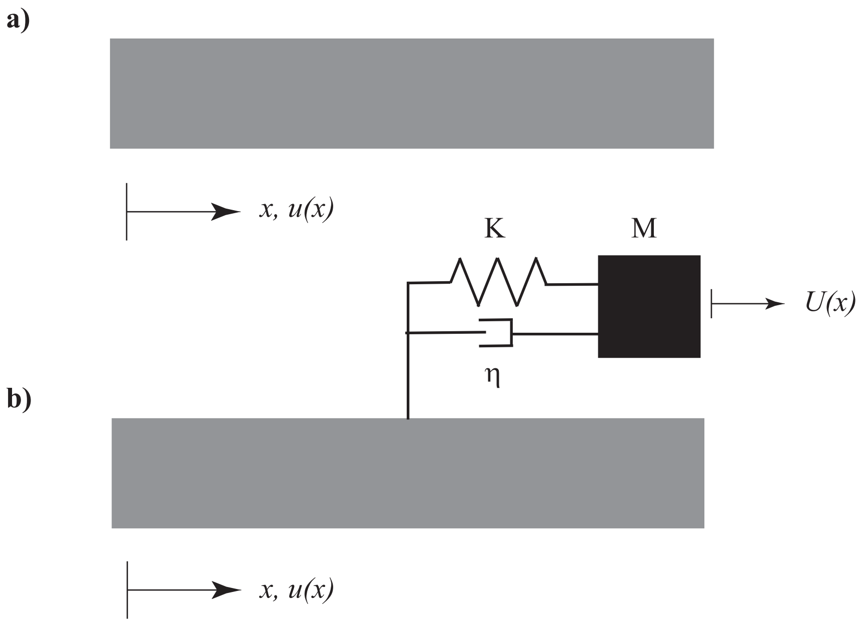

Figure 4.11: *Simplified analytical model*: **a)** Homogeneous rod, **b)** Rod with a local resonator

4.6.1 Simplified Analytical Model

The governing equation describing the longitudinal motion u of a homogenous rod is given by

$$\frac{\partial^2 u}{\partial t^2} - (c_L^*)^2 \frac{\partial^2 u}{\partial x^2} = 0, \tag{4.6}$$

where $c_L^* = \sqrt{E^*/\rho} = c_L\sqrt{(1+i\eta)}$ is the longitudinal speed of sound, where ρ is the density of the medium, $E^* = E(1+i\eta)$ is the complex Young's modulus, and η is the prescribed damping. For the locally resonant rod, an inertia term for the oscillator mass must be added [72] and Eq. (4.6) becomes:

$$\frac{\partial^2 u}{\partial t^2} + M\frac{\partial^2 U}{\partial t^2} - (c_L^*)^2 \frac{\partial^2 u}{\partial x^2} = 0, \tag{4.7}$$

where M is the mass of the oscillator and U its displacement. The volume fraction of the oscillator is negligible compared to the volume of the rod, therefore, the density and the modulus of the rod are not affected. The equation of motion of the spring-mass oscillator is given by

$$M\ddot{U} + \eta(\dot{U} - \dot{u}) + K(U - u) = 0, \tag{4.8}$$

where K is the spring constant, and η the damping coefficient (note that the damping coefficient is identical to the prescribed hysteresis damping). Assuming solutions of the form $u = ue^{i\omega t - i\kappa x}$ and $U = Ue^{i\omega t - i\kappa x}$ for the displacements of the rod and of the oscillator, respectively, Eqs. (4.6), (4.7) and (4.8) respectively become:

$$\begin{aligned} (\omega^2 - (c_L^*)^2\kappa^2)u &= 0 && (4.9)\\ (\omega^2\beta + \omega^2 - (c_L^*)^2 + \kappa^2)u + \beta\omega^2 r &= 0 && (4.10)\\ \omega^2 u + (\omega^2 - i\gamma\omega - \omega_0^2)r &= 0, && (4.11) \end{aligned}$$

where $r = U - u$ is defined as the amplitude of the oscillator displacement relative to the rod, $\omega_0^2 = K/M$ is the resonance frequency of the oscillator, $\gamma = \eta/M$ is a term describing the damping in the oscillator, and $\beta = M/\rho$ is a term describing the strength of coupling between the oscillator and the rod. From Eq. (4.9), we arrive at the dispersion relation for a damped rod:

$$(c_L^*)^2\kappa^2 = \omega^2. \tag{4.12}$$

Combining Eqs. (4.10) and (4.11), we obtain the dispersion for the damped rod with an oscillator:

$$(c_L^*)^2\kappa^2 = \omega^2(1 + \beta\frac{i\gamma\omega + \omega_0^2}{\omega_0^2 - \omega^2 + i\gamma\omega}). \tag{4.13}$$

Following the assumptions made in [72] that the damping is small $\gamma \ll 1$ and that the resonator has a small effect on the propagating waves $\beta \ll 1$, the term $i\beta\omega$ in Eq. (4.13) can be discarded from the numerator:

$$(c_L^*)^2\kappa^2 = \omega^2(1 + \beta\frac{\omega_0^2}{\omega_0^2 - \omega^2 + i\gamma\omega}). \tag{4.14}$$

We set ω_0 and c_L to unity in (4.12) and (4.14), which respectively become:

$$\begin{aligned}(1+i\eta)\kappa^2 &= \omega^2 && (4.15)\\ (1+i\eta)\kappa^2 &= \omega^2+\frac{\omega^2\beta}{1-\omega^2+i\gamma\omega}. && (4.16)\end{aligned}$$

Rearranging (4.16) yields:

$$((\sqrt{1+i\eta})\kappa^2-\omega^2)(1-\omega^2+i\gamma\omega)=\beta\omega^2. \tag{4.17}$$

The left-hand side of Eq. (4.17) describes the interaction of the oscillator with the propagating waves in the rod, whereas the right-hand side describes the interaction of the acoustic mode with the optical mode. From here, there are two ways to solve Eqs. (4.12) and (4.13). Either we treat κ as a fixed and real value and solve for the complex frequency ω, or we treat ω as a fixed and real value and solve for the complex wavenumber κ. As discussed in chapter 2, the first case is typically employed to describe the temporal attenuation of freely propagating waves, whereas the second case is utilized to describe the spatial dissipation of harmonically driven waves. In this chapter, we are interested on the effects of the oscillator on the temporal attenuation of longitudinal waves and therefore, assume a real wavenumber and solve for complex frequencies.

In the work presented in [72], the author is interested in a so-called *exceptional point*, which can be described as the bifurcation point separating the strong-coupling from the weak-coupling regimes. Therefore, if the two modes are uncoupled, one can assume that $\kappa=\omega=1$ in the vicinity of that exceptional point. Equation (4.17) can be further simplified as:

$$(2(\sqrt{1+i\eta})\kappa-\omega)(2-2\omega+i\gamma)=\beta. \tag{4.18}$$

The solution of this quadratic equation is:

$$\omega_{1,2}=\frac{1}{4}(2(\sqrt{1+i\eta})\kappa+2+i\gamma\mp\sqrt{(2-2(\sqrt{1+i\eta})\kappa+i\gamma)^2+4\beta}). \tag{4.19}$$

According to [72], the two modes coalesce at the exceptional point, requiring the square root term to be equal to zero. We rederive here the values taken by γ and ω at that exceptional point for the case where both the rod and the oscillator are damped:

$$\gamma = \frac{2\sqrt{\beta}}{1-2M},\ \kappa = 1,\ \omega = 1 + \frac{i\gamma(1+2M)}{4}. \tag{4.20}$$

4.6.2 Bounds on Metadamping

Let us now characterize the condition on η for the locally resonant rod to exhibit positive and negative metadamping across the wavenumber range. For the sake of simplicity, we followed Maznev's approach in the previous section and assumed a displacement of the form $u = e^{i\omega t - i\kappa x}$ as it greatly helped simplify Eq. (4.18). However, in order to be consistent with our formulation of Bloch's solution given by $\boldsymbol{u}(x,\kappa,t) = \tilde{\boldsymbol{U}}(x,\kappa)e^{i\kappa x+\lambda t}$, we will assume a solution of the form $u = e^{\lambda t - i\kappa x}$ for the rest of this analysis. With this formulation, the solution of the regular rod becomes:

$$\lambda_r = i\omega_r = i\kappa\sqrt{1+i\eta} = -\kappa n + i\kappa m, \tag{4.21}$$

where

$$m = \frac{1}{\sqrt{2}}\sqrt{\sqrt{1+\eta^2}+1}, \quad n = \frac{1}{\sqrt{2}}\sqrt{\sqrt{1+\eta^2}-1}. \tag{4.22}$$

Similarly, the solutions of the locally resonant rod become:

$$\lambda_{1,2} = \frac{1}{4}[(-(\gamma + 2\kappa q \pm b) + i(2\kappa p \pm a)], \tag{4.23}$$

where

$$a = \frac{1}{\sqrt{2}}\sqrt{\sqrt{x^2+y^2}+1}, \quad b = \frac{1}{\sqrt{2}}\sqrt{\sqrt{x^2+y^2}-1}, \tag{4.24}$$

and where

$$x = 4 - 8\kappa m + 4\kappa^2 m^2 - 4\kappa^2 n^2 + 4\beta + 4\kappa n\eta - \eta^2,\ y = -8\kappa n + 8\kappa^2 mn + 4\eta - 4\kappa n\eta. \tag{4.25}$$

From Eq. (4.21), we extract the wavenumber-dependent damping ratio for the regular rod such that $\zeta_r(\kappa) = -\operatorname{Re}(\lambda_r)/\operatorname{Abs}(\lambda_r)$. Note that, because of our choice of material damping model, i.e., a frequency-independent complex Young's modulus, ζ_r remains constant over the whole wavenumber range. Similarly, we extract the damping ratio for the acoustic $\zeta_1(\kappa)$ and for the optical $\zeta_2(\kappa)$

modes of the locally resonant rod from Eq. (4.23).

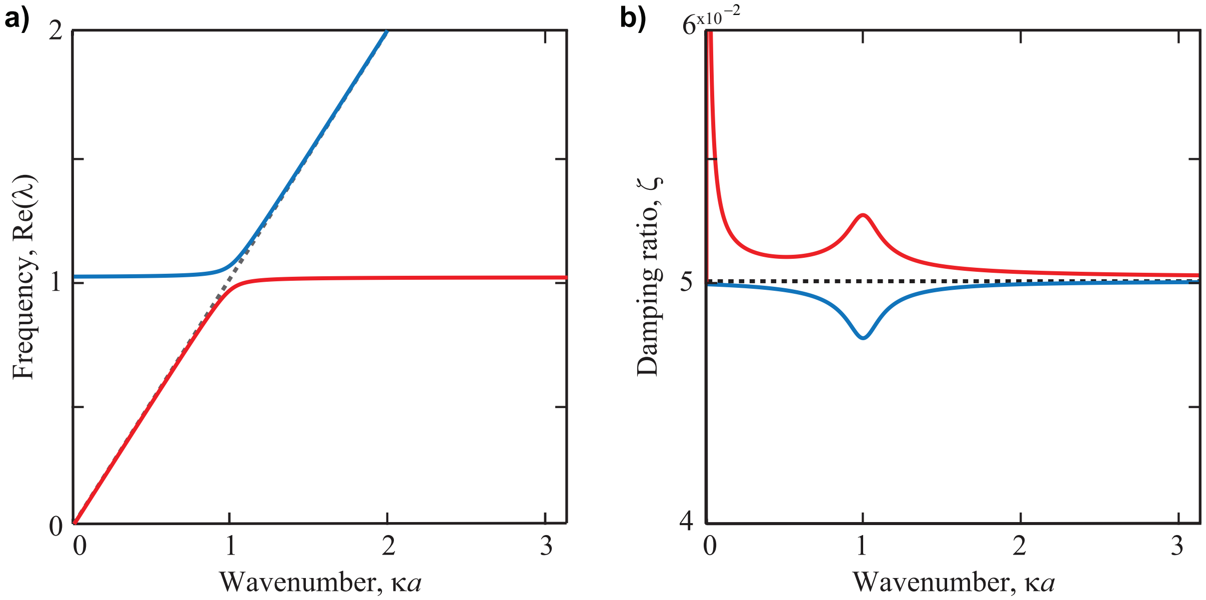

Figure 4.12: **a)** Damped dispersion curves for the regular rod (dashed) and the locally resonant rod (solid) for $\beta = 0.01$ and $\eta = 0.1$. The lower branch is the acoustic mode (red) and the upper branch is the optical mode (blue). **b)** Corresponding damping-ratio diagram.

We want to determine the bounds on the prescribed damping value η, such that the acoustic branch exhibits positive metadamping over the whole wavenumber, i.e., $\zeta_1(\kappa) - \zeta_r(\kappa) > 0$ is satisfied for any $0 < \kappa < \pi$, and the optical branch simultaneously exhibits negative metadamping over the whole wavenumber range, i.e., $\zeta_r(\kappa) - \zeta_2(\kappa) > 0$ is satisfied for any κ. Using Eq. (4.19), we plot the damped frequencies $\omega_{d_r} = \mathrm{Im}(\lambda_r)$ and $\omega_{d_{1,2}} = \mathrm{Im}(\lambda_{1,2})$ for prescribed values $\beta = 0.01$ and $\eta = 0.1$ (see Fig. 4.12-a). As expected, the hybridization caused by the local resonance occurs in the region of the resonance frequency of the oscillator $\omega_0 = 1$.

On Fig. 4.12-b, we show the corresponding damping ratios. The damping branch associated with the acoustic mode lies above the damping ratio branch for the regular rod for the entire wavenumber range (positive metadamping). Conversely, the damping branch associated with the optical mode lies below the damping ratio branch for the regular rod for the entire wavenumber range (negative metadamping).

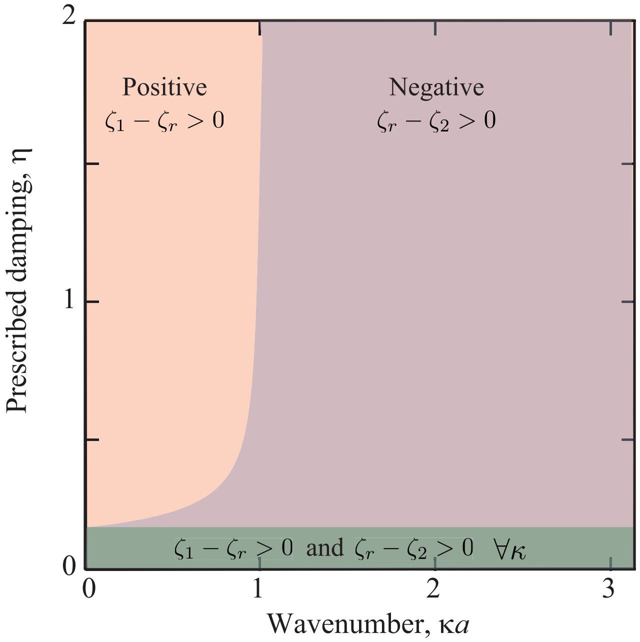

Figure 4.13: Phase diagram for the bounds on the prescribed damping η. The inequality for positive metadamping is shaded in red. The inequality for negative metadamping is shaded in blue. The region shaded in green represents the value of η, which satisfy both conditions on positive and negative metadamping accross the wavenumber range.

Due to the complexity of the closed form of both inequalities $\zeta_1(\kappa) - \zeta_r(\kappa) > 0$ and $\zeta_r(\kappa) - \zeta_2(\kappa) > 0$, we use the help of numerical root finding to solve for the values of η meeting both conditions. For an arbitrary value of $\beta = 0.01$, the results are summarized in the following phase diagram.

From Fig. 4.13, we find that, in order to satisfy both positive and negative metadamping accross the whole wavenumber range, the bounds on η are such that $0 < \eta < 0.14$. Figure 4.14 shows the damping ratio diagram obtained for two values of prescribed damping $\eta_1 = 0.1$ and $\eta_2 = 0.2$. In the first case (see Fig. 4.14-a), η is smaller than the threshold value η_{max}, which leads the optical branch to exhibit negative metadamping over the whole wavenumber range. In the second case however, η is greater than the threshold value η_{max}, and the condition for negative metadamping is therefore no longer satisfied for $0 < \kappa < 0.5$.

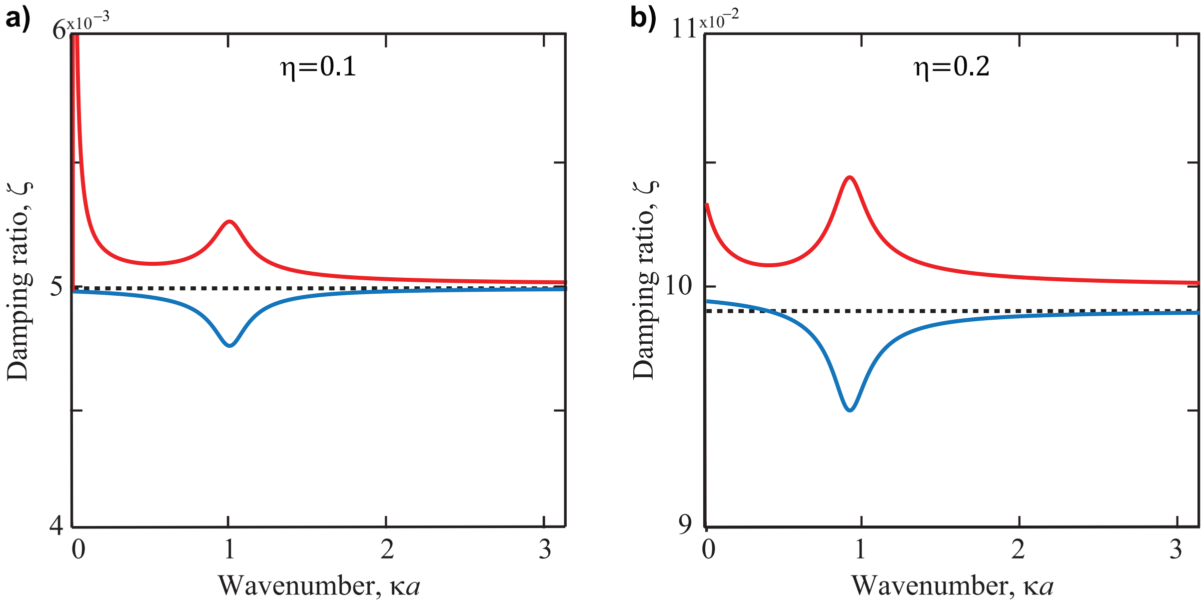

Figure 4.14: **a)** Damping-ratio diagram for $\eta = 0.1 < \eta_{max}$, **b)** Damping-ratio diagram for $\eta = 0.2 > \eta_{max}$.

4.6.3 Effect of Assumptions

For the sake of completeness, we investigate now the effects of the assumptions made from Eq. (4.13) to Eq. (4.17)— small damping, small coupling term, and vicinity of the exceptional point— on the solutions of the dispersion equations. For that purpose, we compare the solutions of Eq. (4.13) to those of Eq. (4.19) Using our Bloch-solution formulation, we rewrite Eq. (4.13) as:

$$(c_L^*)^2\kappa^2 = -\lambda^2(1+\beta\frac{\gamma\lambda+\omega_0^2}{\lambda^2+\gamma\lambda+\omega_0^2}). \tag{4.26}$$

Collecting terms as a function of λ yields the following quartic characteristic equation:

$$\lambda^4 + \lambda^3(\gamma(1+\beta)) + \lambda^2(\omega_0^2(1+\beta) + (c_L^*)^2\kappa^2) + \lambda(\gamma(c_L^*)^2\kappa^2) + (c_L^*)^2\kappa^2\omega_0^2 = 0. \tag{4.27}$$

Because of the complexity of the closed-form solution, we solve Eq. (4.27) with the help of numerical root finding (*roots* algorithm on Matlab). The results are presented in Fig. 4.15. The solutions obtained following Maznev's assumptions are plotted in solid lines, whereas the solutions of the full dispersion relation (with no assumptions made) are plotted in dashed lines. The imaginary part of λ, which is represents damped frequency is hardly affected, even for high levels of prescribed damping. On the other hand, the real part of the solution, from which we the damping ratio, seems to be significantly altered, even for small levels of prescribed damping. The bounds on the prescribed damping η become $0 \leq \eta \leq 0.03$. The maximum value $\eta_{max} = 0.03$ is significantly lower than the one calculated previously ($\eta_{max} = 0.14$).

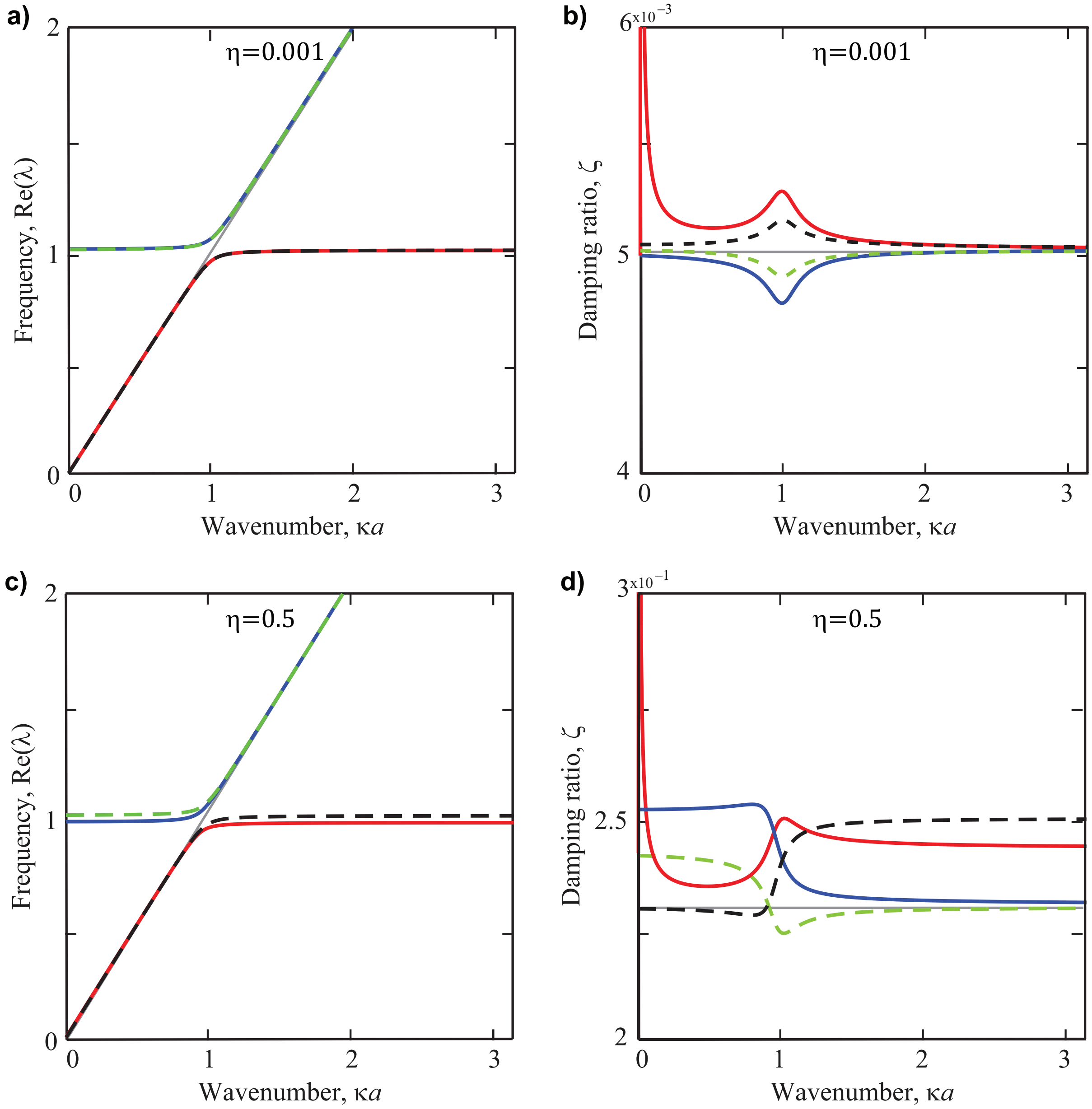

Figure 4.15: **a)** Damping-ratio diagram for $\eta = 0.001 < \eta_{max}$, **b)** Damping-ratio diagram for $\eta = 0.5 > \eta_{max}$.

4.7 Conclusions

Taken together, these results show that the dissipation levels can effectively be either enhanced or reduced in elastic metamaterials. Moreover, the unit-cell analysis provides us with a valuable design tool, as the regions of positive (resp. negative) metadamping can be tailored to the desired frequency ranges. Future work will focus on optimization through design of the unit cell in order to maximize the enhanced (resp. reduced) dissipation effect. Furthermore, metadamping has been here demonstrated in the context of free vibrations. For this concept to be applied to practical devices, it needs to be extended to harmonically driven vibrations.

Chapter 5

Metadamping in Frequency Driven Elastic Waves

5.1 Introduction

Harmonically driven waves are more frequently encountered than freely propagating waves in numerous engineering applications. For example, structures supporting rotating machine components such as turbines or motors are constantly subjected to forced vibrations. Over time, stresses induced by repetitive oscillatory motions can lead to material fatigue and eventually failure. In the previous chapter, elastic metamaterials have proven their ability to enhance dissipation when properly enginereed. This is why, in this chapter, we extend the concept of metadamping to driven waves such that we can design materials exhibiting both high stiffness and high damping under harmonic excitation. We examine the levels of spatial dissipation of the beam unit cells from chapter 4. To that end, we introduce the loss factor, which is the measure of damping that is commonly used to characterize spatial dissipation in viscoelastic materials and discuss some of the definitions available in the literature. Through a dispersion and finite-structure analysis, we verify metadmaping in the context of driven waves both qualitatively and quantitatively.

5.2 Damped Dispersion: Driven Waves versus Free Waves

In this chapter, we consider the same two unit cells as in chapter 4: an unpillared unit cell (homogeneous beam) and a pillared unit cell (homogeneous beam with a square pillar on top). For the sake of convenience, the unit-cell designs are depicted in Fig. 5.1. The harmonically forced

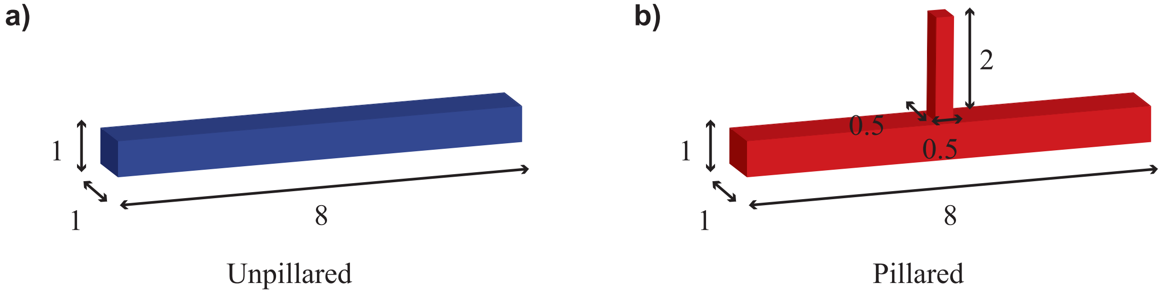

Figure 5.1: Models of the **a)** unpillared and **b)** pillared unit cells. Dimensions are given in inches.

equation of motion for an exponentially damped system is given by:

$$\mathbf{M}\ddot{\boldsymbol{u}}(t) + \int_0^t \mu e^{-\mu(t-\tau)}\mathbf{C}\dot{\boldsymbol{u}}(\tau)d\tau + \mathbf{K}\boldsymbol{u}(t) = \boldsymbol{f}(t). \tag{5.1}$$

We assume a time harmonic solution of the form $\boldsymbol{u}(t) = \tilde{\boldsymbol{U}}e^{i\omega t}$, where ω is a real frequency. Equation (5.1) becomes:

$$(-\omega^2\mathbf{M} + i\omega\frac{\mu}{\mu + i\omega}\mathbf{C} + \mathbf{K})\tilde{\boldsymbol{U}} = \boldsymbol{F}. \tag{5.2}$$

The mass and stiffness matrices are obtained upon discretization with the FEM using 3D 8-node brick elements (512 for the unpillared unit cell and 544 for the pillared unit cell). Both unit cells are made of aluminum with elasticity parameters $E = 68.9$ GPa, $\nu = 0.33$ and density $\rho = 2700$ kg/m^3. The damping matrix is constructed assuming proportional damping such that $\mathbf{C} = p\mathbf{M} + q\mathbf{K}$. In the previous chapter, the damping parameters were determined using experimental data obtained on an aluminum beam. However, because aluminum has low levels of dissipation, we arbitrarily select here a new set of prescribed damping parameters, such that the levels of material damping are higher and the effects of damping on the dispersion are amplified. The parameters chosen for this analysis are $p = 30,\ q = 10^{-7}$, and $\mu = 10^4$.

Bloch periodicity is enforced through Bloch periodic conditions. The Bloch periodicity matrix $\mathbf{P}$, which relates the displacement and stresses on one end of the unit cell to those on the opposite end, can be decomposed as follows (if the order of periodicity is 1):

$$\mathbf{P} = \mathbf{P}_0 + \lambda_x \mathbf{P}_x, \tag{5.3}$$

where $\lambda_x = e^{i\kappa a}$, where κ is the complex wavenumber as defined in Eq. (2.13), and $\mathbf{P}_0$ and $\mathbf{P}_x$ are the Bloch periodicity sub-matrices. To impose the periodic boundary conditions, we premultiply Eq. (5.2) by the complex transpose of the periodicity matrix $\mathbf{P}^*$ and postmultiply by $\mathbf{P}$:

$$\mathbf{P}^*(-\omega^2\mathbf{M} + i\omega\frac{\mu}{\mu + i\omega}\mathbf{C} + \mathbf{K})\mathbf{P}\tilde{\boldsymbol{U}} = \mathbf{0}, \tag{5.4}$$

where $\mathbf{P}^*\boldsymbol{F} = \mathbf{0}$. Equation (5.4) yields a quadratic eigenvalue problem [68]:

$$(\mathbf{A}_2\gamma^2 + \mathbf{A}_1\gamma + \mathbf{A}_0)\tilde{\boldsymbol{U}} = \mathbf{0}, \tag{5.5}$$

with

$$\mathbf{A}_0 = \mathbf{P}_x^T\mathbf{D}\mathbf{P}_0 \tag{5.6a}$$

$$\mathbf{A}_1 = \mathbf{P}_0^T\mathbf{D}\mathbf{P}_0 + \mathbf{P}_x^T\mathbf{D}\mathbf{P}_x \tag{5.6b}$$

$$\mathbf{A}_2 = \mathbf{P}_0^T\mathbf{D}\mathbf{P}_x, \tag{5.6c}$$

and where $\mathbf{D} = (-\omega^2\mathbf{M} + i\omega\frac{\mu}{\mu+i\omega}\mathbf{C} + \mathbf{K})$ is the dynamic matrix. We linearize the eigenvalue problem in Eq. (5.5) through a state-space transformation:

$$\left(\begin{bmatrix}\mathbf{A}_0(\omega) & \mathbf{0}\\ \mathbf{0} & \mathbf{I}\end{bmatrix} - \gamma\begin{bmatrix}-\mathbf{A}_1(\omega) & -\mathbf{A}_2(\omega)\\ \mathbf{I} & \mathbf{0}\end{bmatrix}\right)\begin{Bmatrix}\tilde{\boldsymbol{U}}\\ \gamma\tilde{\mathbf{U}}\end{Bmatrix} = \begin{Bmatrix}\mathbf{0}\\ \mathbf{0}\end{Bmatrix}. \tag{5.7}$$

The solutions of Eq. (5.7) are the frequency-dependent, complex eigenvalues $\gamma(\omega)$, from which we can extract the complex wavenumbers:

$$\kappa(\omega) = \frac{\ln\gamma(\omega)}{ia}. \tag{5.8}$$

Equation (2.12) can be decomposed into its real and imaginary parts such that:

$$\kappa(\omega) = \kappa_R(\omega) + i\kappa_I(\omega). \tag{5.9}$$

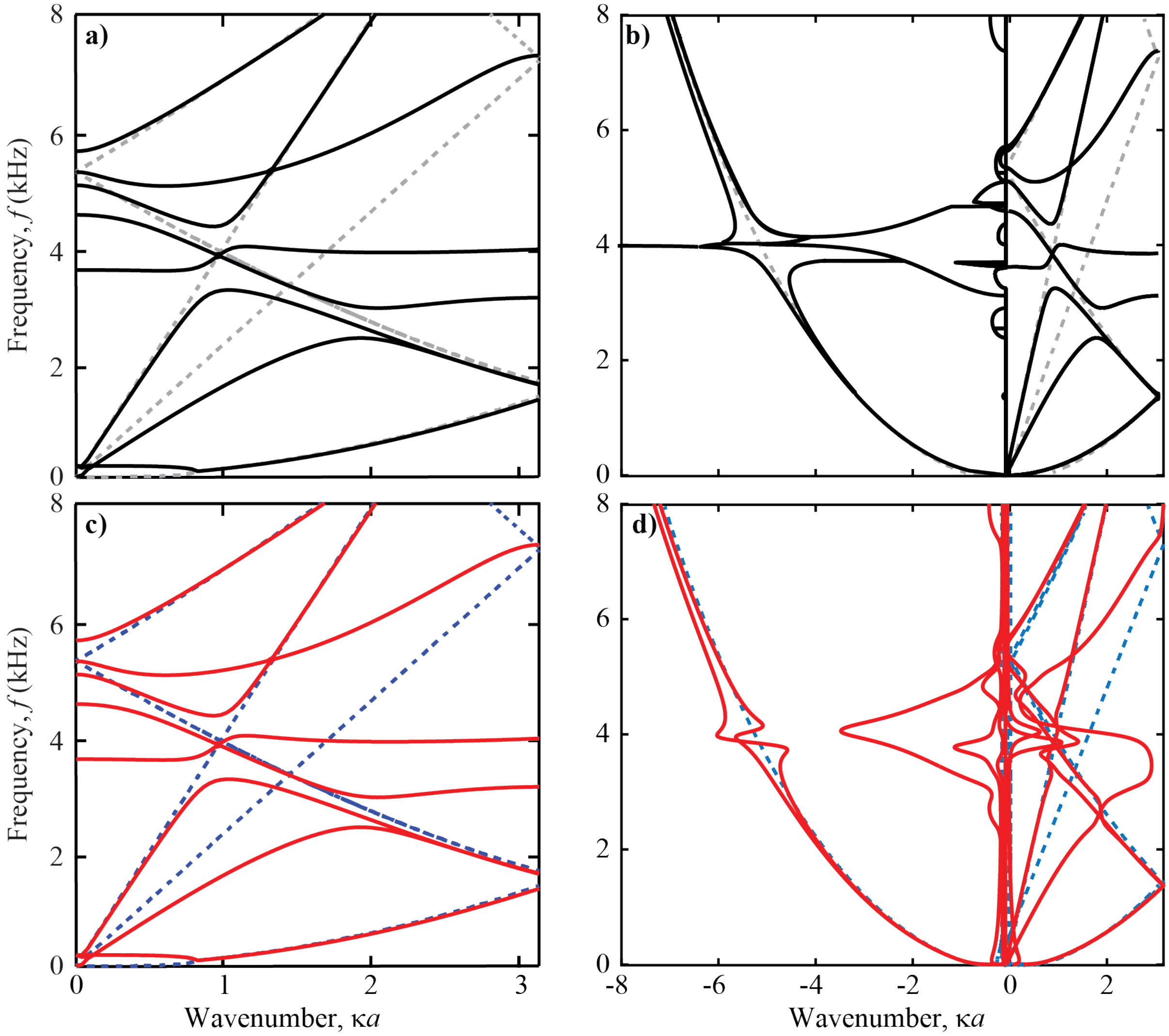

Figure 5.2: Undamped dispersion curves for **a)** freely propagating waves, **b)** harmonically driven waves. Damped dispersion curves for **c)** freely propagating waves, **d)** harmonically driven waves. The unpillared modes are plotted in dashed grey/blue and the pillared modes are plotted in solid black/red.

The real part of Eq. (5.9) corresponds to the oscillating modes, whereas the imaginary part represents the spatially decaying modes.

Figure 5.2-b shows the forced dispersion diagram plotted of the two beam unit cells from chapter 4 for the unadamped case. As a reference, the free dispersion diagram is plotted on Fig. 5.2-a. It is instructive to notice that the real part of dispersion curves obtained with both the $\kappa(\omega)$- and the $\omega(\kappa)$-formulations perfectly match when the systems are undamped. The corresponding forced and free damped dispersion diagrams are shown on Figs. 5.2-d and c, respectively. This time, even for relatively low levels of prescribed damping, the two dispersion diagrams exhibit significant differences, especially around the hybridization region. For example, the two pillared branches associated with the longitudinal mode in the free-waves case merge into one S-shaped branch in the driven-waves case.

5.3 Definition of the Loss Factor

In the free-wave analysis, we characterized the temporal attenuation of both unit cells with the help of the damping ratio, which was extracted from the real part of the complex frequency such that $\zeta = -\operatorname{Re}(\lambda)/|\lambda|$. For the driven-wave analysis, however, there is no temporal dissipation as the system is constantly being excited. (Moreover, the frequency is real and fixed). Therefore, we need to define a new metric in order to describe spatial attenuation caused by dissipative mechanisms in both unit cells. Most of the definitions available in the phononic literature are based on a variant of the so-called loss factor, which was originally introduced as a measure of intrinsic damping in viscoelastic materials.

After unloading, viscoelastic materials recover parts of the energy stored during loading and dissipate the remainder in the form of heat. The ratio of the energy loss and the energy stored is known as the loss tangent or, more frequently, loss factor. For viscoelastic materials, it is generally expressed as a function of the complex Young's modulus $E^* = E' + iE''$:

$$\eta = \tan(\delta) = 2\frac{E''}{E'}, \tag{5.10}$$

where E' is the storage modulus and E'' the loss modulus. Empirical plots of storage and loss moduli as a function of frequency (or temperature) are available for numerous viscoelastic materials in the literature [46]. Another definition of the loss factor, which is also commonly employed for viscoelastic materials, is based on energy concepts [18]:

$$\eta = \frac{D}{2\pi W}, \tag{5.11}$$

where D represents the energy dissipated per cycle (i.e., the amount of energy that has to be provided to maintain steady-state conditions) and W represents the maximum deformation energy stored. For low damping values, Eq. (5.11) is equivalent to Eq. (5.10). These two definitions are suitable and widely use to describe attenuation capacities of viscoelastic materials. However, in order to better describe the loss factor from a wave-propagation perspective, an alternative definition of the loss factor is required. Andreassen and Jensen [7] followed the work by [19] and defined the loss factor as twice the ratio of the imaginary component of the wavevector over the real component of the wavevector:

$$\eta = 2\frac{\kappa_I}{\kappa_R}. \tag{5.12}$$

In their study, they also computed an equivalent temporal decay by taking the product of the group velocity of the wave c_g with the spatial decay given by the imaginary part of the wavenumber κ_I such that $(TD)_\kappa = \kappa_I c_g$. They showed, that for low levels of material damping, the equivalent temporal decay matched the actual temporal decay which can explicitly be obtained from the $\omega(\kappa)$-formulation. Krushynska *et al.* [55] used the same loss factor definition to evaluate the attenuation performance of viscoelastic acoustic metamaterials. In addition, they noted that, in order to quantify the spatial attenuation due to material damping solely, the effects of the local resonance on spatial attenuation had to be taken into account. To that end, they calculated an "undamped" loss factor for the case where no damping was applied to the metamaterial and subtracted it from the actual loss factor.

Manconi and Mace proposed another approach to calculate the loss factor in periodic viscoelastic laminate plates based on the modal strain energy method, which was first proposed by Ungar and

Kerwin [111]. The loss factor is obtained by calculating the wave mode shapes [69]:

$$\eta = \frac{\mathbf{V}^*{}_j \mathbf{K}'' \mathbf{V}_j}{\mathbf{V}^*{}_j \mathbf{K}' \mathbf{V}_j}, \tag{5.13}$$

where $\mathbf{V}_j$ is a matrix containing the eigenvectors, $\mathbf{K}'$ is the real part of the stiffness matrix $\mathbf{K}$, and $\mathbf{K}''$ its imaginary part. One disadvantage of this method is that it requires the knowledge of the stiffness matrix which is not always guaranteed.

Finally, we consider the definition by Langley [61], which he proposed in the framework of wave propagation in a 1D waveguide. The wavenumber is complex and can be written as:

$$\kappa^* = \kappa_R - i\frac{\omega\eta}{cg}. \tag{5.14}$$

Rearranging terms yields the following loss factor definition:

$$\eta = 2\frac{\kappa_I c_g}{\omega}. \tag{5.15}$$

For the remainder of this analysis, we will use the definition of Eq. (5.12). A comparison of this

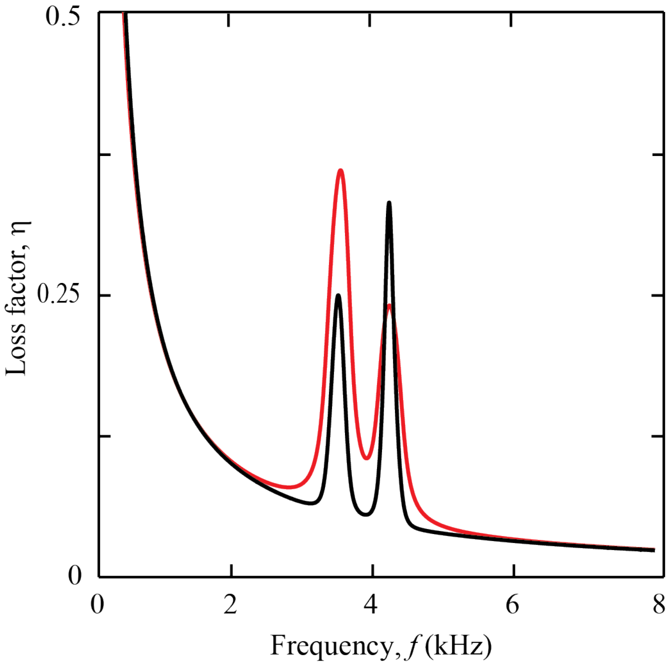

Figure 5.3: Comparison of the loss factor definitions described in Eqs. (5.12) (red) and (5.15) (black).

definition with that of Langley (Eq. (5.15)) is shown on Fig. 5.3 for the longitudinal modes of the unpillared and pillared unit cells. For the unpillared case, both definitions yield the same loss factor diagram. For the pillared case, on the other hand, the loss factors are qualitatively similar but quantitatively different. Note that for all the loss factor diagrams presented in this chapter, we follow Krushynska's approach of subtracting the "undamped" loss factor, such that we discard the effects of the local resonance on spatial attenuation and solely focus on the effects of material damping on the spatial dissipation.

5.4 Evidence of Metadamping in the Dispersion Analysis

We start by investigating metadamping in the dispersion analysis in order to identify the frequency regions where the pillared beam is expected to exhibit higher (or lower) levels of dissipation than the unpillared beam. Using a MAC criterion technique, we sort the waves by modes in Fig. 5.2-d and identify the longitudinal modes in both the dispersion and loss-factor diagrams. They are plotted on Fig. 5.4-a and b, respectively, and the other modes are shaded in grey.

We identify three points of interest on Fig. 5.4-b, which we will further investigate in our finite-structure analysis to numerically demonstrate the existence of positive metadamping. According to Fig. 5.4-b, we expect positive metadamping if the excitation frequency falls into one of the two "metadamping regions": $f_A = 3,421$ Hz (point A) and $f_B = 4,111$ Hz (point B). We also choose a point where the loss factors are identical for both beams $f_C = 2,000$ Hz (point C) and we expect that, if excited at that frequencies, both beams will have similar levels of dissipation.

5.5 Evidence of Metadamping in the Finite System

The unpillared beam geometry is such that $0 \leq x \leq 32,\ 0 \leq y \leq 1$, and $0 \leq z \leq 1$ in. The pillared beam, which is composed of four unit cells, has the same dimensions. In addition four pillars of dimensions $0.5 \times 0.5 \times 2$ are periodically arranged along the longitudinal axis. The mass $\mathbf{M}$ and stiffness $\mathbf{K}$ matrices are obtained upon discretization with the FEM using 3D 8-node brick finite elements (2,048 for the unpillared geometry, 2,176 for the pillared geometry). The numerical

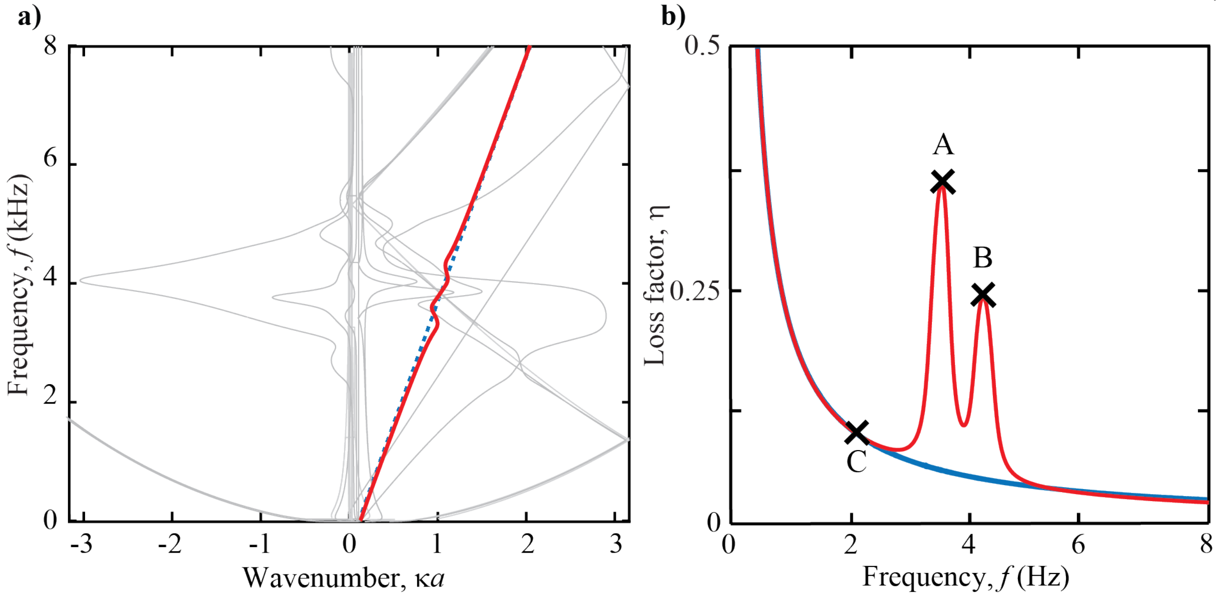

Figure 5.4: *Dispersion analysis:* **a)** Dispersion diagram for the unpillared (blue) and pillared (red) unit cells. The longitudinal modes of the beam are identified and highlighted. The other modes are shaded. **b)** Corresponding loss-factor diagram. The three frequencies of interest are denoted as A, B, and C.

time responses are obtained by implementing the direct time integration method for exponentially damped systems described in [3]. In order to simulate harmonically driven vibrations, a sinusoidal force is applied at the center of the cross-section on one end of the beam along the longitudinal axis, and the displacement is calculated at a point located at the center of the opposite cross-section. The simulation is run for a total time of $t = 2$ s with a time step of $\Delta t = 1 \times 10^{-6}$ s.

The undamped and damped responses of both beams are shown in Fig. 5.5 for the three excitation frequencies discussed earlier. Figures 5.5-a and b correspond to point A (i.e., $f_A = 3,421$ Hz), Figs. 5.5-c and d to point B (i.e., $f_B = 4,111$ Hz), and finally Figs. 5.5-e and f to point C (i.e., $f = 2,000$ Hz).

5.5.1 Steady-State Metadamping Metric

As we cannot use the metadamping-ratio procedure proposed in chapter 4 to characterize metadamping for forced waves, we need to define a new metric in order to quantify the levels

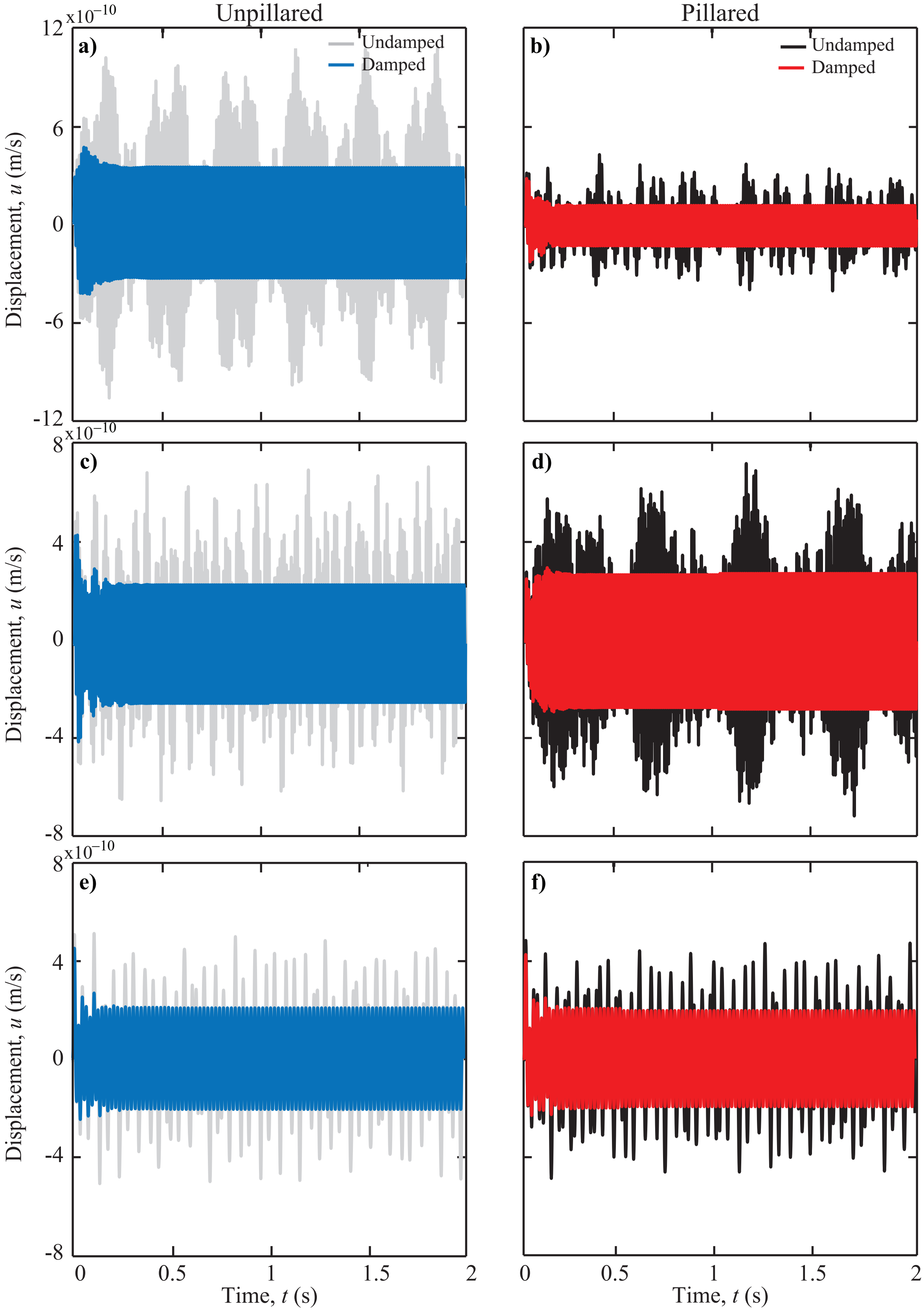

Figure 5.5: *Finite-structure analysis*: **a-b)** Undamped and damped time responses under the excitation frequency $f_A = 3,421$ Hz for **a)** the unpillared beam and **b)** the pillared beam, **c-d)** Undamped and damped time responses under the excitation frequency $f_B = 4,111$ Hz for **c)** the unpillared beam and **d)** the pillared beam, **e-f)** Undamped and damped time responses under the excitation frequency $f_C = 2,000$ Hz for **e)** the unpillared beam and **f)** the pillared beam.

of spatial dissipation in the finite-structure analysis. We cannot compare the change in absolute magnitude of the damped time signals, as these amplitude changes might be due to nondissipative mechanisms. Instead, we propose to compare the relative amplitude change between the undamped and damped time signals to ensure that we account for material dissipation only. If the beams are excited at frequency A or B, we expect a higher amplitude decrease for the pillared beam than for the unpillared beam. At the neutral point, we expect similar levels of amplitude change.

The procedure to obtain the steady-state metadamping metric is as follows. We split the time series in intervals of $dt = 0.01$ s for $1 \leq t \leq 1.8$ s (which corresponds to two "beats" on Fig. 5.5-d) and find the maximum displacement amplitude in each of these intervals. We then average these maximum amplitudes over all the intervals to ensure that any beating phenomenon is "averaged". We define the amplitude ratio as:

$$r_{\text{unpillared/pillared}} = \frac{\max(D_{\text{undamped}})}{\max(D_{\text{damped}})}, \tag{5.16}$$

where D_{undamped} and D_{damped} are the average maximum amplitude of the undamped and damped time response, respectively, for $1 \leq t \leq 1.8$ s. As in chapter 4, we define the metadamping ratio as:

$$r_{\text{meta}} = \frac{r_{\text{pillared}}}{r_{\text{unpillared}}}. \tag{5.17}$$

A ratio greater than unity suggest that the pillared beam exhibits positive metadamping. The ratios obtained for the three excitations frequencies are presented in Table 5.1. At both point A and B, r_{meta} is greater than unity, hence confirming our positive metadamping analysis. It also interesting to note that the two ratios follow the trend observed on the loss-factor diagram (see

Metadamping Metric: Steady-State Regime			
	A: Positive Metadamping	B: Positive Metadamping	C: No Metadamping
$r_{\text{unpillared}}$	1.26	1.62	1.34
r_{pillared}	1.62	1.78	1.33
$\boldsymbol{r}_{\text{meta}}$	**1.29**	**1.10**	**1.01**

Table 5.1: Steady-State Metadamping Metrics

Fig. 5.4-b), i.e., metadamping is stronger at point A than at point B. At point C, $r_{\text{meta}} = 1.01$ is very close to unity as expected from the loss-factor diagram.

5.6 Simplified Analytical Model

As in chapter 4, we analytically investigate the longitudinal motion of a locally resonant rod in order to further investigate metadamping in the context of driven waves. We consider the same simplified models as that of chapter 4: a homogeneous rod, and a rod with a spring-mass oscillator attached to it. A schematics of the two models is shown on Fig. 5.6. Following a recent study by Maznev [72], we derived the dispersion relations for both systems in chapter 4 (see Eqs. (4.12) and (4.14)). They are as follows:

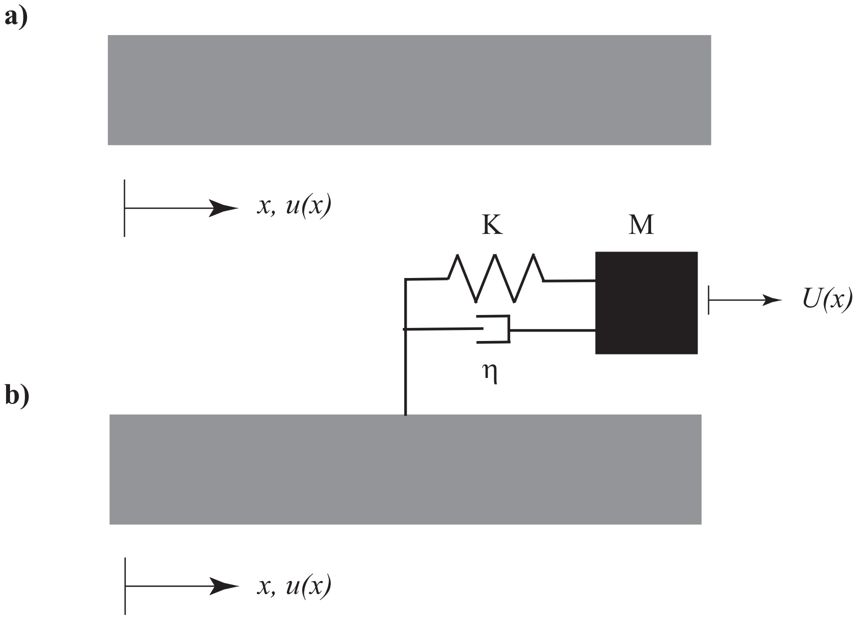

Figure 5.6: *Simplified analytical model*: **a)** Homogeneous rod, **b)** Rod with a local resonator

$$(c_L^*)^2\kappa^2 = \omega^2 \tag{5.18a}$$

$$(c_L^*)^2\kappa^2 = \omega^2(1 + \beta\frac{\omega_0^2 + i\gamma\omega}{\omega_0^2 - \omega^2 + i\gamma\omega}). \tag{5.18b}$$

This time, we treat the frequency ω as the independent variable and solve for the complex wavenumbers, which can be explicitly obtained from Eqs. (5.18a) and (5.18b). Note that, because these equations are much simpler to solve than the equations of the free-waves problem, we do not make any assumptions on the prescribed damping η nor on the coupling term β. However, we normalize the solutions by setting $c_L = \sqrt{E/\rho}$ and ω_0 to unity. Equations (5.18a) and (5.18b) then become:

$$\kappa^2 = \frac{1}{(1+i\eta)}\omega^2 \tag{5.19a}$$

$$\kappa^2 = \frac{1}{(1+i\eta)}\omega^2(1+\beta\frac{1+i\gamma\omega}{1-\omega^2+i\gamma\omega}). \tag{5.19b}$$

The solutions of Eqs. (5.19a) and(5.19b) are plotted on Fig. 5.7-a if the rods are undamped and on Fig. 5.7-b if the prescribed damping is $\eta = 0.1$. As in chapter 4, the coupling factor is arbitrarily set to $\beta = 0.01$. For the damped case, the two branches (acoustic and optical) merge into one S-shaped branch. On Figs. 5.7-c and d, we plot the loss factors calculated according to the definition given in Eq. 5.12. For the undamped case, the loss factors are zero as expected. For the damped case (see Fig. 5.7-d), we observe that the loss factor associated with the locally resonant rod forms a peak, which is known as the Lorentzian absorption peak [72]. The Lorentzian function can be mathematically described as:

$$L(x) = \frac{1}{\pi}\frac{\frac{1}{2}\Gamma}{(x-x_0)^2+(\frac{1}{2}\Gamma)^2}, \tag{5.20}$$

where x_0 is the center of the peak and Γ the width of the peak. Moreover, the value at its maximum is given by

$$L(x_0) = \frac{2}{\pi\Gamma}. \tag{5.21}$$

Next, we vary the value prescribed damping η from 0 to 1 and observe the effects on the height and width of the absorption peak. The results are presented on Fig. 5.8. Figure 5.8-a depicts the normalized maximum amplitude at the center of the absorption peak $P_n = L(x_0)/\eta$ as a function of the prescribed damping η. Figure 5.8-b depicts the normalized width $W_n = \Gamma\eta$ as a function of η. It is interesting to note that the absorption peak amplitude decreases for higher values of prescribed damping η. Conversely, the peak becomes wider for increasing values of η.

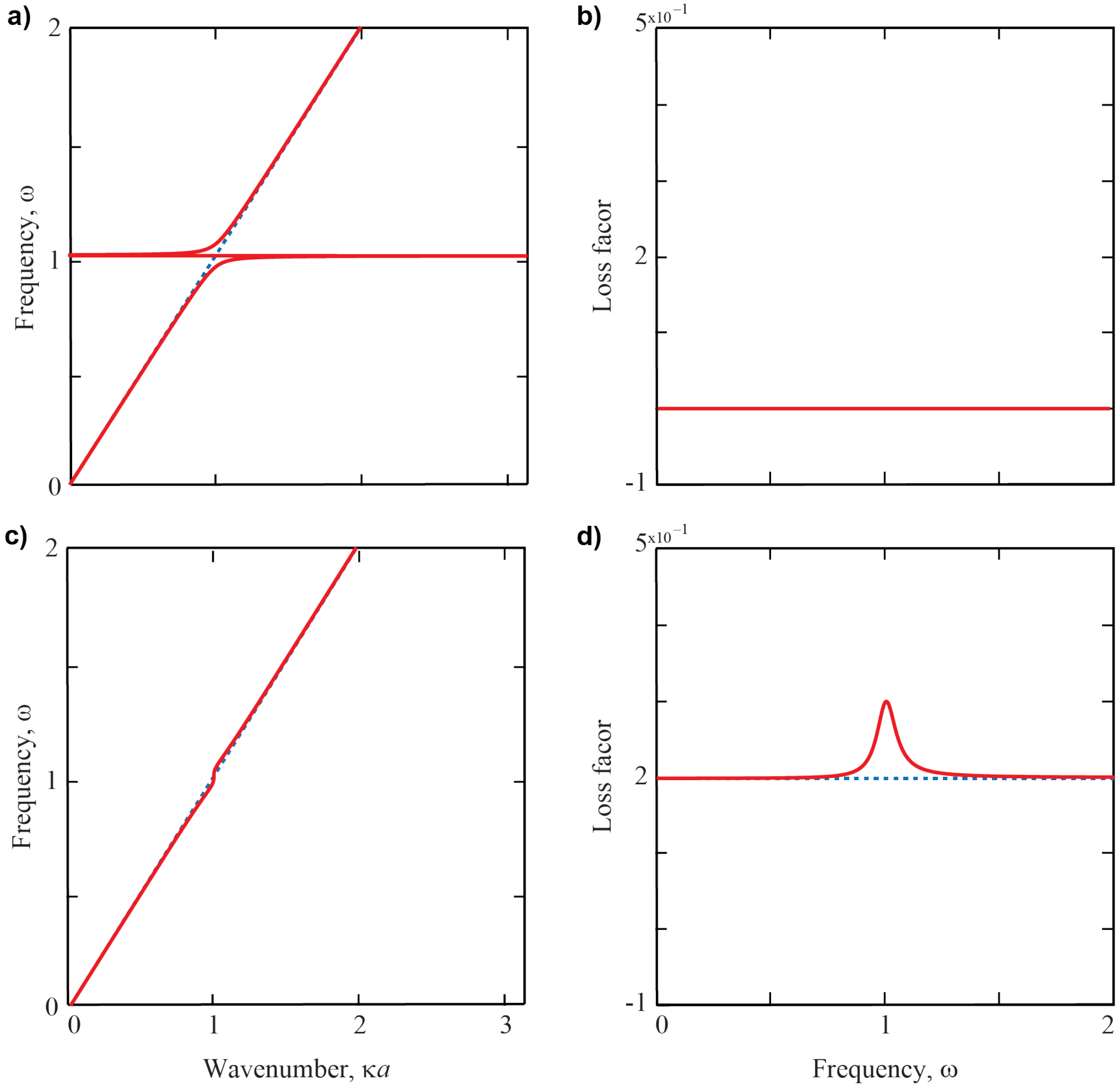

Figure 5.7: **a)** Undamped dispersion curves for the rod (dashed blue) and locally resonant rod (solid red) and **b)** corresponding loss-factor diagram. **c)** Damped dispersion curves for the rod (dashed blue) and locally resonant rod (solid red) for $\eta = 0.01$ and **c)** corresponding loss-factor diagram. The coupling factor is arbitrarily set to $\beta = 0.01$.

The decrease in dissipation levels for higher values of prescribed damping can be explained by the interaction between the two attenuation mechanisms: local resonance and material damping. Indeed, high levels of material damping may neutralize the effects of the local resonator on energy dissipation [70]. Finally, we select two values of η such that $\eta_A = 0.0707$ and $\eta_B = 0.5$. The

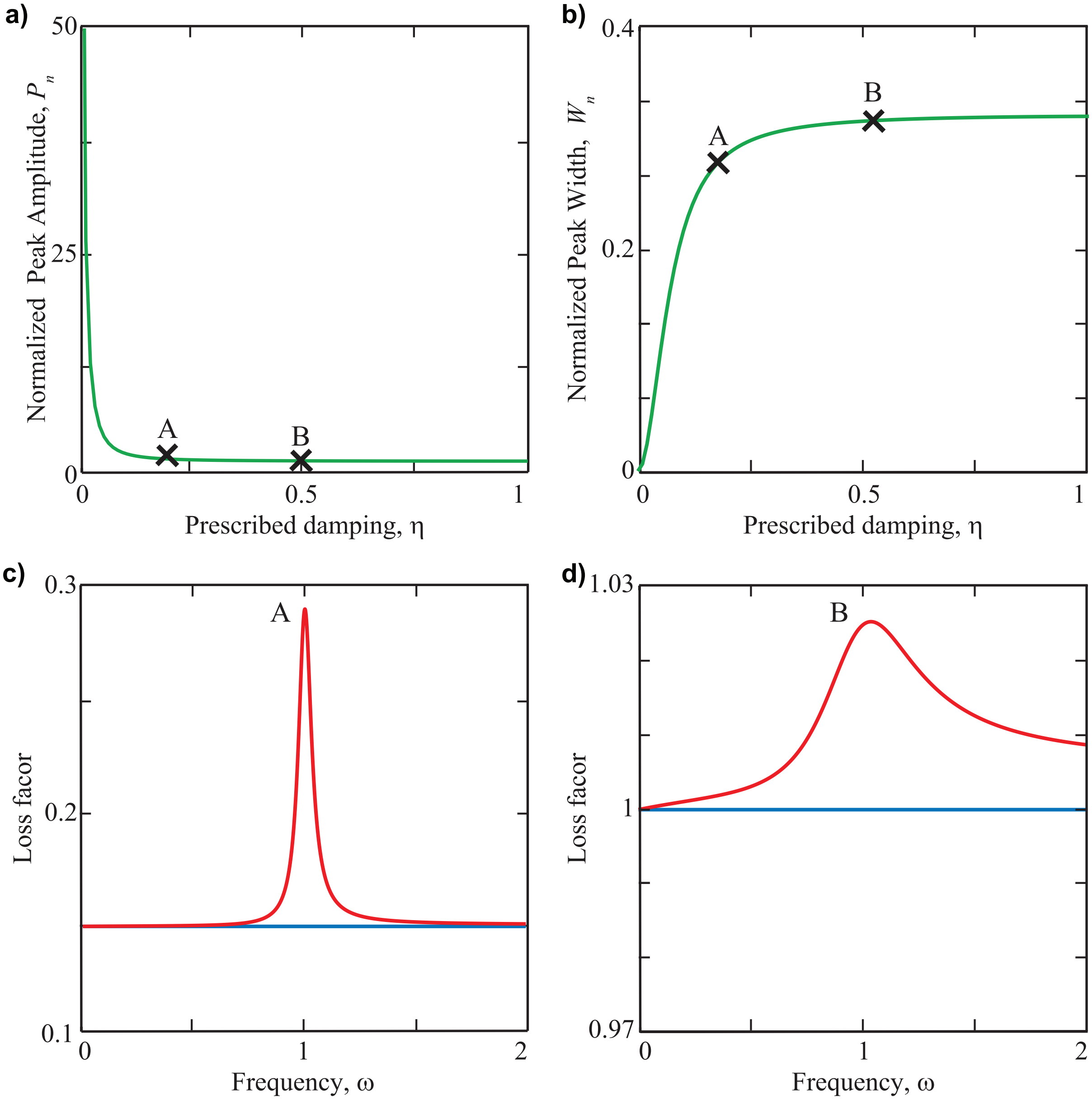

Figure 5.8: **a)** Normalized peak amplitude $P_n = L(x_0)/\eta$ and **b)** normalized width $W_n = \Gamma\eta$ as a function of the prescribed damping η. Two values of prescribed damping are selected and denoted as A $\eta_A = 0.0707$ and B $\eta_B = 0.5$. The corresponding loss-factor diagrams are plotted in **c)** and **d)**, respectively.

corresponding loss factors for these two values of η are shown on Figs. 5.8-c and d.

5.7 Parametric Design Study and Metadamping Performance

In this section, we vary the unit-cell length a in order to determine the effect of pillar spacing on the metadamping performance. Figure 5.9 summarizes the results for unit-cell lengths ranging from $a = 3$ to $a = 8$ in. For $3 \leq a \leq 6$ in, we observe one single absorption peak centered on the local resonance of the pillar, which is very similar to what we observed for the simplified analytical model. Moreover, we notice that, as the unit-cell length increases, the maximum amplitude of the peak decreases and its width increases. For $a = 7$ and $a = 8$ in, we observe the formation of another absorption peak which gets closer to the first one as the unit-cell length increases. That second peak is most likely caused by localized pillar modes which fall into the hybridization region for these two designs, and interact with the "equivalent" longitudinal modes of the pillared beam.

According to the loss-factor diagrams (see Fig. 5.9), the highest metadamping performance is obtained for $a = 3$ in at $f = 3,597$ Hz. We verify the correlation between the infinite and finite analyses by calculating the undamped and damped time responses for two finite beams made of four unit cells each. The new unpillared beam geometry is such that $0 \leq x \leq 12$, $0 \leq y \leq 1$, and $0 \leq z \leq 1$ in. The new pillared beam, which is composed of four unit cells, has the same dimensions. Again, four pillars of dimensions $0.5 \times 0.5 \times 2$ are periodically arranged along the longitudinal axis. The undamped and damped time responses of both beams under the excitation frequency of $f = 3,597$ Hz are shown on Fig. 5.10. Following the procedure described in section 5.5.1, we find the metadamping ratio to be $r_{\text{meta}} = 1.83$, which is an improvement of 40% compared to the ratio obtained for $a = 8$ in.

5.8 Conclusions

In this chapter, we have theoretically extended the concept of metadamping to the driven-waves problem with qualitative and quantitative verification. By performing a dispersion analysis on the 3D beam unit cells and examining the loss factor diagrams, we were able to determine the frequency regions where the pillared beam is expected to exhibit higher levels of dissipation than

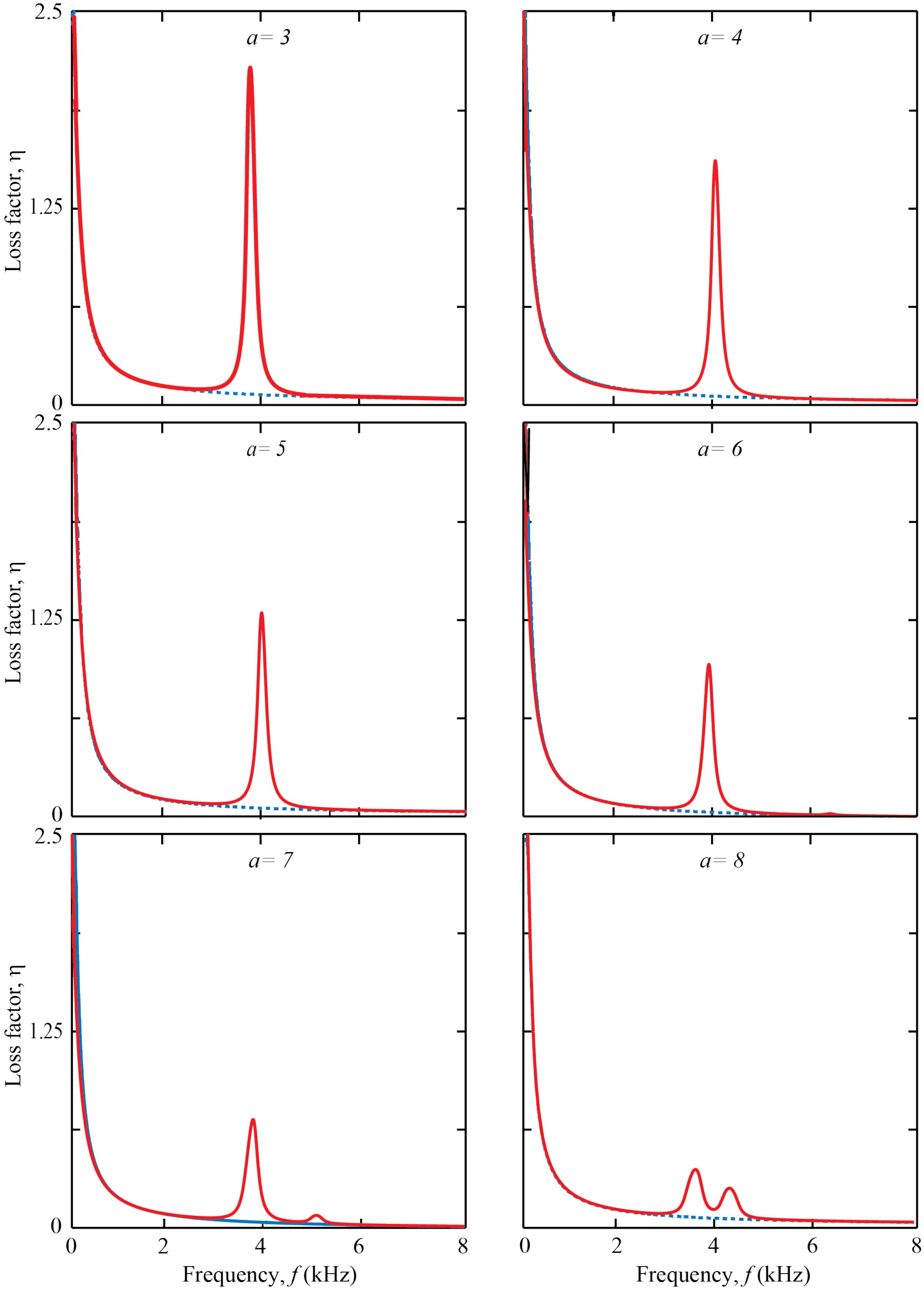

Figure 5.9: *Parametric Design Study*: Longitudinal loss factor for the unpillared unit cell dashed blue) and pillared unit cell (solid red) as a function of the unit-cell length a.

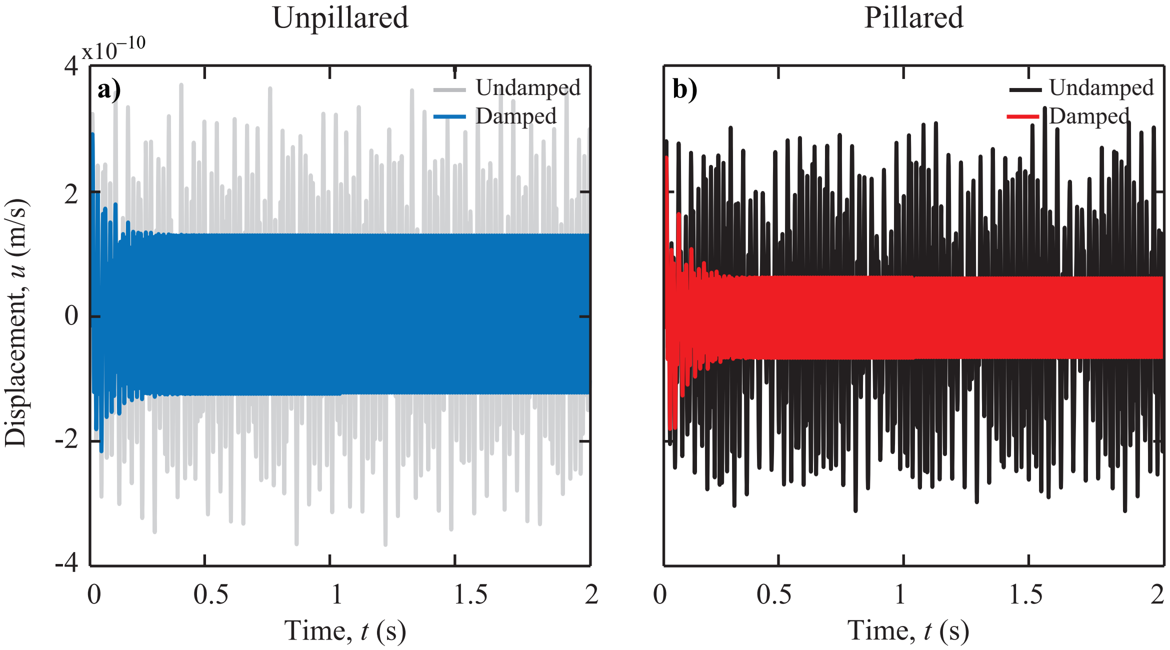

Figure 5.10: *Finite-structure analysis for* $a = 3$ *in*: **a-b)** Undamped and damped time responses under the excitation frequency $f_A = 3,597$ Hz for **a)** the unpillared beam and **b)** the pillared beam.

the unpillared beam. Next, we performed a finite-structure analysis and showed that indeed, if excited at frequencies falling into one of the metadamping regions, the pillared beam exhibited higher spatial dissipation levels than the unpillared beam. The analytical study on a simplified model enabled us to deepen our understanding of the absorption peaks observed in the loss-factor diagrams. Based on that knowledge, we performed a parametric design study to determine the effects of pillar spacing on the amplitude of the absorption peak. We find that for $a = 3$ in, the metadamping performance is increased by 40% compared to $a = 8$ in. In the future, other designs will be considered in order to further improve the metadamping performance of the pillared beam. Moreover, the concept of metadamping in forced-waves problems will be extended to structures with higher order of periodicity.

Chapter 6

Conclusions

6.1 Summary of Dissertation

This thesis focuses on the relation between dissipation and dispersion in elastic metamaterials. In the first part, a viscoelastic damping model fitted with experimental data is developed in order to accurately predict dissipation within the dispersion analysis framework. In the second part, the ability of metamaterials to manipulate waves is exploited for the engineering of dissipation. To that end, the concept of metadamping is validated in a finite experimental setting with direct correlation to theory as described within the dispersion framework.

Chapter 1 introduces the concept of phononic materials, of which elastic metamaterials are a category. A brief literature search covering the history and recent applications of these delicately engineered materials is provided. Elementary concepts of their dynamics are introduced and their fundamental equations are derived in the context of 1D discrete systems. Then, the topic of damped wave propagation in phononic materials is presented and a succinct literature review examines the methods employed for the treatment of damping in these materials. Finally, the concept of metadamping is reviewed and a brief literature synopsis is provided such that the work is placed into context.

Chapter 2 further details the treatment of damping in phononic materials. The methods to solve the two classes of damped-wave propagation problems—free waves versus driven waves—are presented and a literature review of their use in the phononics literature is provided. Next, a viscous dashpot is added to the spring-mass system of Chapter 1 and the fundamental equations are derived for both free and forced waves.

Chapter 3 extends the analysis of damping in phononic metamaterials to 3D continuous systems. In this chapter, only freely propagating waves are considered. Two categories of damping models are discussedviscous and viscoelasticand the corresponding damped dispersion relations are derived for general continuous unit cells. The dispersion curves of a 3D beam unit cell are plotted for different levels of prescribed damping, and the effects of viscous versus viscoelastic damping on the dispersion spectrum are discussed. The main result of this chapter is the development (with relevant mathematical derivations) of a viscoelastic damping model, whose parameters are curve-fitted with experimental data. The experimental procedure, as well as the method that was developed to extract sets of damping parameters leading to realistic levels of dissipation, are thoroughly described. In addition, two examples of the application of this method are presented: one to extract the damping parameters for longitudinal modes of an aluminum beam, and one to extract the damping parameters for bending modes of an ABS plate. The set of parameters obtained for the longitudinal modes of the aluminum beam are used in chapter 4, in an effort to accurately predict the damped dispersion characteristics of an aluminum elastic metamaterial beam.

Chapter 4 examines the capacity of a 3D locally resonant beam to exhibit either higher or lower dissipation levels, at certain frequency ranges, than those of a homogeneous beam in the context of freely propagating waves. This concept of damping emergence, referred to as "metadamping", is demonstrated first in two finite aluminum beams (a homogeneous beam and a locally resonant beam), both experimentally and numerically. Then, a dispersion analysis is performed on the homogeneous and locally resonant beam unit cells in order to further investigate the phenomenon of damping emergence caused by the presence of local resonances. On the damping-ratio diagram, two frequency regions are identified: one associated with positive metadamping and one with negative metadamping; the latter has been identified for the first time as a concept. We observe that the higher temporal attenuation in the corresponding finite structure takes place where the frequency range of the excitation coincides with the region where positive metadamping is indicated in the dispersion analysis, thus confirming our positive metadamping hypothesis. To investigate the negative metadamping hypothesis, the finite structures are numerically excited with an impulse whose frequency content is designed such that it falls within the identified negative metadamping region. In that case, the pillared beam is shown to exhibit lower levels of temporal attenuation. Next, a parametric design study is performed in order to examine the effects of pillar spacing on both positive and negative metadamping. Finally, wave dispersion relations are derived for simplified analytical models of both beams, and bounds on the prescribed damping value are determined such that the condition for simultaneous positive and negative metadamping is satisfied across the entire wavenumber range covering the first Brillouin zone.

Chapter 5 extends the study of metadamping followed in chapter 4 to the driven-waves problems. The dispersion diagrams from chapter 4 are rederived for harmonically driven waves. Next, a discussion is provided on the definitions of the loss factor, which is a measure of damping typically employed to describe spatial attenuation in viscoelastic materials. A dispersion analysis is performed in order to identify the potential regions of metadamping. For the unit-cell design of chapter 4 (i.e., $a = 8$ in), two positive metadamping frequency values are determined. By exciting the finite structures at frequencies coinciding with these two frequencies, and comparing the relative amplitude changes between the undamped and damped signals, the existence of positive metadamping is verified in the context of driven waves. Then, the simplified analytical model is used to further investigate the absorption peak observed in the loss factor diagram. Finally, the unit-cell length is varied and the metadamping performance of the various designs is examined. It is found that for $a = 3$ in the metadamping performance is improved by 40% compared to $a = 8$ in, which is consistent with what would be expected when the density of the resonators is increased.

6.2 Outlook

This dissertation has aimed to take the concept of metadamping, which was first proposed in [40] for theoretical systems, a significant step closer to being applied in practice. To that end, a physically realistic damping model has been developed to better predict damped-wave propagation within the dispersion analysis framework. Metadamping in 3D continuous systems has also been explored and the realization of positive metadamping for free-wave propagation has been demonstrated for the first time. Despite encouraging results, the work done in this dissertation has solely focused on rather simple structures such as beams. In order to design more practical devices which could be used by engineers in applications where both high stiffness and high damping are desirable, further work on the concept of metadamping has to be conducted. Possible tracks for future studies are listed below:

- *Damping model improvement*: Despite great efforts to develop a realistic damping model based on experimental data, the model presented has limitations and could be considerably improved. For example, one could use a general damping matrix instead of a proportional damping matrix. Furthermore, one could consider a more complex kernel function for the convolution integral in the damping force term, such a generalized Maxwell model.

- *Experimental validation of negative metadamping for free waves*: In this dissertation, positive metadamping has been experimentally validated because the frequency range of the excitation applied with the available laboratory modal hammer coincided with the region where positive metadamping is indicated in the dispersion analysis. In order to experimentally demonstrate negative metadamping for the locally resonant beam design proposed in chapter 4, one would need to synthesize an experimental excitation whose frequency profile matches the one plotted in dashed black in Fig. 4.7-a.

- *Negative metadamping in driven waves*: For applications where extremely low levels of wave attenuation is desirable (e.g., NDT, imaging lenses), devices exhibiting negative metadamping would be highly appealing and potentially revolutionary. Although, the existence of negative metadamping for free waves has been shown in this dissertation, it has yet to be shown in the context of driven waves.

- *Experimental verification of metadamping in driven waves*: The definition of the metadamping metric that is proposed in chapter 5 is suitable for numerical experiments, as one can easily remove damping from the model and compute the undamped time series. However, every real-world system has damping, therefore, it would be impossible to obtain an experimental undamped time response. Consequently, in order to experimentally demonstrate metadamping in driven waves, another metric should be proposed. One could also obtain an experimental loss-factor diagram by exciting the structure at one frequency and measuring the complex wavenumber.

- *Extension to more complex structures*: The studies in this dissertation have been conducted on relatively large beams. In addition to being rather impractical for most engineering applications, these structures are periodic along one dimension only. A natural next step would be to extend the realization of metadamping to structures with higher order of periodicity such as plates and to investigate it in the context of different types of waves (flexural, shear, etc.), and for smaller and more compact structures.

Bibliography

[1] Loss Factors of Viscoelastic Systems in Terms of Energy Concepts: The Journal of the Acoustical Society of America: Vol 34, No 7.

[2] Younes Achaoui, Abdelkrim Khelif, Sarah Benchabane, and Vincent Laude. Polarization state and level repulsion in two-dimensional phononic crystals and waveguides in the presence of material anisotropy. Journal of Physics D: Applied Physics, 43(18):185401, May 2010.

[3] S. Adhikari and N. Wagner. Direct time-domain integration method for exponentially damped linear systems. Computers & Structures, 82(2930):2453–2461, November 2004.

[4] S. Adhikari and J. Woodhouse. Identification of damping: Part 1, viscous damping. Journal of Sound and Vibration, 243(1):43–61, May 2001.

[5] S. Adhikari and J. Woodhouse. Identification of damping: Part 2, non-viscous damping. Journal of Sound and Vibration, 243(1):63–88, May 2001.

[6] Muralidhar Ambati, Nicholas Fang, Cheng Sun, and Xiang Zhang. Surface resonant states and superlensing in acoustic metamaterials. Physical Review B, 75(19), May 2007.

[7] Erik Andreassen and Jakob S. Jensen. Analysis of Phononic Bandgap Structures With Dissipation. Journal of Vibration and Acoustics, 135(4):041015–041015, June 2013.

[8] I. Antoniadis, D. Chronopoulos, V. Spitas, and D. Koulocheris. Hyper-damping properties of a stiff and stable linear oscillator with a negative stiffness element. Journal of Sound and Vibration, 346:37–52, June 2015.

[9] S. Biringen. Active control of transition by periodic suctionblowing. Physics of Fluids (1958-1988), 27(6):1345–1347, June 1984.

[10] S. BIRINGEN, W. E. NUTT, and M. J. CARUSO. Numerical study of transition control by periodic suction blowing. AIAA Journal, 25(2):239–244, 1987.

[11] Felix Bloch. ber die Quantenmechanik der Elektronen in Kristallgittern. Zeitschrift fr Physik, 52(7-8):555–600, July 1929.

[12] EI Houssaine EI Boudouti and Bahram Djafari-Rouhani. One-Dimensional Phononic Crystals. In Pierre A. Deymier, editor, Acoustic Metamaterials and Phononic Crystals, number 173 in Springer Series in Solid-State Sciences, pages 45–93. Springer Berlin Heidelberg, 2013.

[13] M. Brodt and R. S. Lakes. Composite Materials Which Exhibit High Stiffness and High Viscoelastic Damping. Journal of Composite Materials, 29(14):1823–1833, September 1995.

[14] Thomas Brunet, Aurore Merlin, Benoit Mascaro, Kevin Zimny, Jacques Leng, Olivier Poncelet, Christophe Aristgui, and Olivier Mondain-Monval. Soft 3d acoustic metamaterial with negative index. Nature Materials, 14(4):384–388, April 2015.

[15] Dennis M. Bushnell, Jerry N. Hefner, and Robert L. Ash. Effect of compliant wall motion on turbulent boundary layers. Physics of Fluids (1958-1988), 20(10):S31–S48, October 1977.

[16] Huanyang Chen and C. T. Chan. Acoustic cloaking in three dimensions using acoustic metamaterials. Applied Physics Letters, 91(18):183518, October 2007.

[17] M. Collet, M. Ouisse, M. Ruzzene, and M. N. Ichchou. FloquetBloch decomposition for the computation of dispersion of two-dimensional periodic, damped mechanical systems. International Journal of Solids and Structures, 48(20):2837–2848, October 2011.

[18] S. H. Crandall. The role of damping in vibration theory. Journal of Sound and Vibration, 11(1):3–IN1, January 1970.

[19] L. Cremer and O. Leilich. Zur Theorie der Biegekettenleiter. Archiv der Elektrischen Ubertragung, 7:261–270, 1953.

[20] D. DePauw, H. Al Babaa, and M. Nouh. Metadamping and energy dissipation enhancement via hybrid phononic resonators. Extreme Mechanics Letters, 18:36–44, January 2018.

[21] Pierre A. Deymier. Introduction to Phononic Crystals and Acoustic Metamaterials. In Pierre A. Deymier, editor, Acoustic Metamaterials and Phononic Crystals, number 173 in Springer Series in Solid-State Sciences, pages 1–12. Springer Berlin Heidelberg, 2013.

[22] Pierre A. Deymier and L. Dobrzynski. Discrete One-Dimensional Phononic and Resonant Crystals. In Pierre A. Deymier, editor, Acoustic Metamaterials and Phononic Crystals, number 173 in Springer Series in Solid-State Sciences, pages 13–44. Springer Berlin Heidelberg, 2013.

[23] D. j Ewins. Modal Testing, Theory, Practice, and Application. Research Studies Pre, Baldock, Hertfordshire, England ; Philadelphia, PA, 2 edition edition, September 2000.

[24] Nicholas Fang, Dongjuan Xi, Jianyi Xu, Muralidhar Ambati, Werayut Srituravanich, Cheng Sun, and Xiang Zhang. Ultrasonic metamaterials with negative modulus. Nature Materials, 5(6):452–456, June 2006.

[25] Farhad Farzbod and Michael J. Leamy. Analysis of Blochs Method and the Propagation Technique in Periodic Structures. Journal of Vibration and Acoustics, 133(3):031010–031010, March 2011.

[26] Michael J. Frazier and Mahmoud I. Hussein. Viscous-to-viscoelastic transition in phononic crystal and metamaterial band structures. The Journal of the Acoustical Society of America, 138(5):3169–3180, November 2015.

[27] Michael J. Frazier and Mahmoud I. Hussein. Generalized Bloch's theorem for viscous metamaterials: Dispersion and effective properties based on frequencies and wavenumbers that are simultaneously complex. Comptes Rendus Physique, 17(5):565–577, May 2016.

[28] L. Gaul, P. Klein, and S. Kemple. Damping description involving fractional operators. Mechanical Systems and Signal Processing, 5(2):81–88, March 1991.

[29] D. F. Golla and P. C. Hughes. Dynamics of Viscoelastic StructuresA Time-Domain, Finite Element Formulation. Journal of Applied Mechanics, 52(4):897–906, December 1985.

[30] Sbastien Guenneau, Alexander Movchan, Gunnar Ptursson, and S. Anantha Ramakrishna. Acoustic metamaterials for sound focusing and confinement. New Journal of Physics, 9(11):399, 2007.

[31] R. A. Handler, E. Levich, and L. Sirovich. Drag reduction in turbulent channel flow by phase randomization. Physics of Fluids A: Fluid Dynamics (1989-1993), 5(3):686–694, March 1993.

[32] Manfred A. Heckl. Investigations on the Vibrations of Grillages and Other Simple Beam Structures. The Journal of the Acoustical Society of America, 36(7):1335–1343, July 1964.

[33] Zhao Hong-Gang, Liu Yao-Zong, Wen Ji-Hong, Yu Dian-Long, Wang Gang, and Wen Xi-Sen. Sound Absorption of Locally Resonant Sonic Materials. Chinese Physics Letters, 23(8):2132, 2006.

[34] Andrew Honohan, Michael Amitay, and Ari Glezer. Aerodynamic control using synthetic jets. In Fluids 2000 Conference and Exhibit. American Institute of Aeronautics and Astronautics, June 2000.

[35] M. I. Hussein, S. Biringen, O. R. Bilal, and A. Kucala. Flow stabilization by subsurface phonons. Proceedings of the Royal Society A: Mathematical, Physical and Engineering Sciences, 471(2177):20140928–20140928, April 2015.

[36] Mahmoud I. Hussein. Reduced Bloch mode expansion for periodic media band structure calculations. Proceedings of the Royal Society of London A: Mathematical, Physical and Engineering Sciences, 465(2109):2825–2848, September 2009.

[37] Mahmoud I. Hussein. Theory of damped Bloch waves in elastic media. Physical Review B, 80(21), December 2009.

[38] Mahmoud I. Hussein and Michael J. Frazier. Band structure of phononic crystals with general damping. Journal of Applied Physics, 108(9):093506, November 2010.

[39] Mahmoud I. Hussein and Michael J. Frazier. Damped Phononic Crystals and Acoustic Metamaterials. In Pierre A. Deymier, editor, Acoustic Metamaterials and Phononic Crystals, number 173 in Springer Series in Solid-State Sciences, pages 201–215. Springer Berlin Heidelberg, 2013.

[40] Mahmoud I. Hussein and Michael J. Frazier. Metadamping: An emergent phenomenon in dissipative metamaterials. Journal of Sound and Vibration, 332(20):4767–4774, September 2013.

[41] Mahmoud I. Hussein, Gregory M. Hulbert, and Richard A. Scott. Dispersive elastodynamics of 1d banded materials and structures: analysis. Journal of Sound and Vibration, 289(45):779–806, February 2006.

[42] Joo Hwan Oh, Yoon Jae Kim, and Yoon Young Kim. Wave attenuation and dissipation mechanisms in viscoelastic phononic crystals. Journal of Applied Physics, 113(10):106101, March 2013.

[43] T. Jaglinski, D. Kochmann, D. Stone, and R. S. Lakes. Composite Materials with Viscoelastic Stiffness Greater Than Diamond. Science, 315(5812):620–622, February 2007.

[44] Sajeev John. Strong localization of photons in certain disordered dielectric superlattices. Physical Review Letters, 58(23):2486–2489, June 1987.

[45] Conor D. Johnson and David A. Kienholz. Finite Element Prediction of Damping in Structures with Constrained Viscoelastic Layers. AIAA Journal, 20(9):1284–1290, 1982.

[46] David I. G. Jones. Handbook of Viscoelastic Vibration Damping. John Wiley & Sons, August 2001.

[47] W. J. Jung, N. Mangiavacchi, and R. Akhavan. Suppression of turbulence in wall-bounded flows by high-frequency spanwise oscillations. Physics of Fluids A: Fluid Dynamics (1989-1993), 4(8):1605–1607, 1992.

[48] Hammouche Khales, Abdelkader Hassein-Bey, and Abdelkrim Khelif. Evidence of Ultrasonic Band Gap in Aluminum Phononic Crystal Beam. Journal of Vibration and Acoustics, 135(4):041007–041007, June 2013.

[49] A. Khelif, A. Choujaa, S. Benchabane, B. Djafari-Rouhani, and V. Laude. Guiding and bending of acoustic waves in highly confined phononic crystal waveguides. Applied Physics Letters, 84(22):4400–4402, May 2004.

[50] Georges Kouroussis, L. Ben Fekih, Calogero Conti, and Olivier Verlinden. EasyMod: A MatLab/SciLab toolbox for teaching modal analysis. In Proceedings of the international congress on sound and vibration, Vilnius, pages 9–12, 2012.

[51] Max O. Kramer. Boundary Layer Stabilization by Distributed Damping. Journal of the American Society for Naval Engineers, 72(1):25–34, February 1960.

[52] Dimitri Krattiger. Fast Band-Structure Computation for Phononic and Electronic Waves in Crystals. Aerospace Engineering Sciences Graduate Theses & Dissertations, January 2017.

[53] Dimitri Krattiger, Romik Khajehtourian, Clmence L. Bacquet, and Mahmoud I. Hussein. Anisotropic dissipation in lattice metamaterials. AIP Advances, 6(12):121802, 2016.

[54] Dimitri Krattiger, A. Srikantha Phani, and Mahmoud I. Hussein. Wave Propagation in Damped Lattice Materials. In Dynamics of Lattice Materials, pages 93–106. John Wiley & Sons, Ltd, 2017.

[55] A. O. Krushynska, V. G. Kouznetsova, and M. G. D. Geers. Visco-elastic effects on wave dispersion in three-phase acoustic metamaterials. Journal of the Mechanics and Physics of Solids, 96:29–47, November 2016.

[56] A. O. Krushynska, V. G. Kouznetsova, and M. G. D. Geers. Visco-elastic effects on wave dispersion in three-phase acoustic metamaterials. Journal of the Mechanics and Physics of Solids, 96:29–47, November 2016.

[57] Alec Kucala and Sedat Biringen. Spatial simulation of channel flow instability and control. Journal of Fluid Mechanics, 738:105–123, January 2014.

[58] Yun Lai, Ying Wu, Ping Sheng, and Zhao-Qing Zhang. Hybrid elastic solids. Nature Materials, 10(8):620–624, August 2011.

[59] R. S. Lakes, T. Lee, A. Bersie, and Y. C. Wang. Extreme damping in composite materials with negative-stiffness inclusions. Nature, 410(6828):565–567, March 2001.

[60] R. S. Langley. On The Forced Response Of One-dimensional Periodic Structures: Vibration Localization By Damping. Journal of Sound and Vibration, 178(3):411–428, December 1994.

[61] R. S. Langley. Some Perspectives on Wave-Mode Duality in Sea. In IUTAM Symposium on Statistical Energy Analysis, Solid Mechanics and Its Applications, pages 1–12. Springer, Dordrecht, 1999.

[62] M. A. Lewiska, V. G. Kouznetsova, J. A. W. van Dommelen, A. O. Krushynska, and M. G. D. Geers. The attenuation performance of locally resonant acoustic metamaterials based on generalised viscoelastic modelling. International Journal of Solids and Structures, 126-127:163–174, November 2017.

[63] Yaozong Liu, Dianlong Yu, Honggang Zhao, Jihong Wen, and Xisen Wen. Theoretical study of two-dimensional phononic crystals with viscoelasticity based on fractional derivative models. Journal of Physics D: Applied Physics, 41(6):065503, 2008.

[64] Zhengyou Liu, Xixiang Zhang, Yiwei Mao, Y. Y. Zhu, Zhiyu Yang, C. T. Chan, and Ping Sheng. Locally Resonant Sonic Materials. Science, 289(5485):1734–1736, September 2000.

[65] S. Lurie, M. Minhat, N. Tuchkova, and J. Soliaev. On Remarkable Loss Amplification Mechanism in Fiber Reinforced Laminated Composite Materials. Applied Composite Materials, 21(1):179–196, January 2014.

[66] N. M. M. Maia, J. M. M. Silva, and A. M. R. Ribeiro. On a general model for damping. Journal of Sound and Vibration, 218(5):749–767, December 1998.

[67] E. Manconi and B. R. Mace. Wave propagation in viscoelastic laminated composite plates using a wave/finite element method. EuroDyn 2008, 2008.

[68] Elisabetta Manconi and B. R. Mace. Modelling wave propagation in two-dimensional structures using a wave/finite element technique. ISVR Technical Memorandum, 2007.

[69] Elisabetta Manconi and Sergey Sorokin. On the effect of damping on dispersion curves in plates. International Journal of Solids and Structures, 50(11):1966–1973, June 2013.

[70] James M. Manimala and C. T. Sun. Microstructural design studies for locally dissipative acoustic metamaterials. Journal of Applied Physics, 115(2):023518, January 2014.

[71] O. Bou Matar, J. O. Vasseur, and Pierre A. Deymier. Tunable Phononic Crystals and Metamaterials. In Pierre A. Deymier, editor, Acoustic Metamaterials and Phononic Crystals, number 173 in Springer Series in Solid-State Sciences, pages 253–280. Springer Berlin Heidelberg, 2013.

[72] A. A. Maznev. Bifurcation of avoided crossing at an exceptional point in the dispersion of sound and light in locally resonant media. Journal of Applied Physics, 123(9):091715, February 2018.

[73] K. McManus and J. Magill. Separation control in incompressible and compressible flows using pulsed jets. In AIAA,Fluid Dynamics Conference, 27th, New Orleans LA. American Institute of Aeronautics and Astronautics, June 1996.

[74] K. R. McManus, P. B. Joshi, H. H. Legner, and S. J. Davis. Active control of aerodynamic stall using pulsed jet actuators. In AIAA, Fluid Dynamics Conference, 26 th, San Diego, CA, 1995.

[75] D. J. Mead. A general theory of harmonic wave propagation in linear periodic systems with multiple coupling. Journal of Sound and Vibration, 27(2):235–260, March 1973.

[76] D. J. Mead. Wave propagation and natural modes in periodic systems: I. Mono-coupled systems. Journal of Sound and Vibration, 40(1):1–18, May 1975.

[77] Denys J. Mead and Gautam Sen Gupta. Propagation of flexural waves in infinite, damped rib-skin structures. Technical Report ISVR-M-303, Southampton University (England) Institute of Sound and Vibration Research, January 1970.

[78] Julien Meaud, Trisha Sain, Bongjun Yeom, Sei Jin Park, Anna Brieland Shoultz, Gregory Hulbert, Zheng-Dong Ma, Nicholas A. Kotov, A. John Hart, Ellen M. Arruda, and Anthony M. Waas. Simultaneously High Stiffness and Damping in Nanoengineered Microtruss Composites. ACS Nano, 8(4):3468–3475, April 2014.

[79] Jun Mei, Guancong Ma, Min Yang, Jason Yang, and Ping Sheng. Dynamic Mass Density and Acoustic Metamaterials. In Pierre A. Deymier, editor, Acoustic Metamaterials and Phononic Crystals, number 173 in Springer Series in Solid-State Sciences, pages 159–199. Springer Berlin Heidelberg, 2013.

[80] B. Merheb, P. A. Deymier, M. Jain, M. Aloshyna-Lesuffleur, S. Mohanty, A. Berker, and R. W. Greger. Elastic and viscoelastic effects in rubber/air acoustic band gap structures: A theoretical and experimental study. Journal of Applied Physics, 104(6):064913, September 2008.

[81] Rayisa P. Moiseyenko and Vincent Laude. Material loss influence on the complex band structure and group velocity in phononic crystals. Physical Review B, 83(6), February 2011.

[82] Subrata Mukherjee and E. H. Lee. Dispersion relations and mode shapes for waves in laminated viscoelastic composites by variational methods. International Journal of Solids and Structures, 14(1):1–13, January 1978.

[83] Youichi Murakami, Leonid Shtilman, and Evgeny Levich. Reducing turbulence by phase juggling. Physics of Fluids A: Fluid Dynamics (1989-1993), 4(8):1776–1781, August 1992.

[84] S. Nemat-Nasser. General variational methods for waves in elastic composites. Journal of Elasticity, 2(2):73–90, June 1972.

[85] Isaac Newton. The Principia : Mathematical Principles of Natural Philosophy. University of California Press, Berkeley, October 1999.

[86] Choon Mahn Park, Jong Jin Park, Seung Hwan Lee, Yong Mun Seo, Chul Koo Kim, and Sam H. Lee. Amplification of Acoustic Evanescent Waves Using Metamaterial Slabs. Physical Review Letters, 107(19):194301, November 2011.

[87] Y. Pennec, B. Djafari-Rouhani, J. O. Vasseur, A. Khelif, and P. A. Deymier. Tunable filtering and demultiplexing in phononic crystals with hollow cylinders. Physical Review E, 69(4), April 2004.

[88] A. Srikantha Phani and Mahmoud I. Hussein. Analysis of Damped Bloch Waves by the Rayleigh Perturbation Method. Journal of Vibration and Acoustics, 135(4):041014–041014, June 2013.

[89] H. Policarpo, M. M. Neves, and A. M. R. Ribeiro. Dynamical Response of a Multi-Laminated Periodic Bar: Analytical, Numerical and Experimental Study, 2010.

[90] I. E. Psarobas. Viscoelastic response of sonic band-gap materials. Physical Review B, 64(1), June 2001.

[91] John William Strutt Rayleigh. The theory of sound. London, Macmillan and co., 1877.

[92] Lord Rayleigh Sec R. Rayleigh. XVII. On the maintenance of vibrations by forces of double frequency, and on the propagation of waves through a medium endowed with a periodic structure. The London, Edinburgh, and Dublin Philosophical Magazine and Journal of Science, 24(147):145–159, August 1887.

[93] Geo A. Richards, Douglas L. Straub, and Edward H. Robey. Passive Control of Combustion Dynamics in Stationary Gas Turbines. Journal of Propulsion and Power, 19(5):795–810, 2003.

[94] J J Riley, M Gad el Hak, and and R. W. Metcalfe. Complaint Coatings. Annual Review of Fluid Mechanics, 20(1):393–420, 1988.

[95] Trisha Sain, Julien Meaud, Greg Hulbert, Ellen M. Arruda, and Anthony M. Waas. Simultaneously high stiffness and damping in a class of wavy layered composites. Composite Structures, 101:104–110, July 2013.

[96] D. Schurig, J. J. Mock, B. J. Justice, S. A. Cummer, J. B. Pendry, A. F. Starr, and D. R. Smith. Metamaterial Electromagnetic Cloak at Microwave Frequencies. Science, 314(5801):977–980, November 2006.

[97] G. Sen Gupta. Natural frequencies of periodic skin-stringer structures using a wave approach. Journal of Sound and Vibration, 16(4):567–580, June 1971.

[98] M. Sigalas and E. N. Economou. Band structure of elastic waves in two dimensional systems. Solid State Communications, 86(3):141–143, April 1993.

[99] M. M. Sigalas and E. N. Economou. Elastic and acoustic wave band structure. Journal of Sound Vibration, 158:377–382, October 1992.

[100] Barton L. Smith and Ari Glezer. The formation and evolution of synthetic jets. Physics of Fluids (1994-present), 10(9):2281–2297, September 1998.

[101] D. R. Smith, J. B. Pendry, and M. C. K. Wiltshire. Metamaterials and Negative Refractive Index. Science, 305(5685):788–792, August 2004.

[102] Jos Snchez-Dehesa, Victor M. Garcia-Chocano, Daniel Torrent, Francisco Cervera, Suitberto Cabrera, and Francisco Simon. Noise control by sonic crystal barriers made of recycled materials. The Journal of the Acoustical Society of America, 129(3):1173–1183, March 2011.

[103] Rudolf Sprik and Gerard H. Wegdam. Acoustic band gaps in composites of solids and viscous liquids. Solid State Communications, 106(2):77–81, April 1998.

[104] A. Sukhovich, J. H. Page, J. O. Vasseur, J. F. Robillard, N. Swinteck, and Pierre A. Deymier. 2d3d Phononic Crystals. In Pierre A. Deymier, editor, Acoustic Metamaterials and Phononic Crystals, number 173 in Springer Series in Solid-State Sciences, pages 95–157. Springer Berlin Heidelberg, 2013.

[105] C. T. Sun, J. D. Achenbach, and G. Herrmann. Time-harmonic waves in a stratified medium propagating in the direction of the layering. Journal of Applied Mechanics, Transactions ASME, 35(2):408–410, January 1964.

[106] C.-T. Sun, J. D. Achenbach, and G. Herrmann. Time-Harmonic Waves in a Stratified Medium Propagating in the Direction of the Layering. Journal of Applied Mechanics, 35(2):408–411, June 1968.

[107] N. Swinteck, Pierre A. Deymier, K. Muralidharan, and R. Erdmann. Nanoscale Phononic Crystals and Structures. In Pierre A. Deymier, editor, Acoustic Metamaterials and Phononic Crystals, number 173 in Springer Series in Solid-State Sciences, pages 281–327. Springer Berlin Heidelberg, 2013.

[108] H.D. Taylor. The elimination of diffuser separation by vortex generators. United Aircraft Corporation Report, R-4012-3, June 1947.

[109] G. Theocharis, N. Boechler, and C. Daraio. Nonlinear Periodic Phononic Structures and Granular Crystals. In Pierre A. Deymier, editor, Acoustic Metamaterials and Phononic Crystals, number 173 in Springer Series in Solid-State Sciences, pages 217–251. Springer Berlin Heidelberg, 2013.

[110] Peter J. Torvik and D. L. Bagley. Fractional derivatives in the description of damping materials and phenomena. The Role of Damping in Vibration and Noise Control, pages 125–135, 1987.

[111] Eric E. Ungar and Edward M. Kerwin. Loss Factors of Viscoelastic Systems in Terms of Energy Concepts. The Journal of the Acoustical Society of America, 34(7):954–957, July 1962.

[112] Lucas Van Belle, Claus Claeys, Elke Deckers, and Wim Desmet. On the impact of damping on the dispersion curves of a locally resonant metamaterial: Modelling and experimental validation. Journal of Sound and Vibration, 409:1–23, November 2017.

[113] J. O. Vasseur, Pierre A. Deymier, A. Sukhovich, B. Merheb, A.-C. Hladky-Hennion, and M. I. Hussein. Phononic Band Structures and Transmission Coefficients: Methods and Approaches. In Pierre A. Deymier, editor, Acoustic Metamaterials and Phononic Crystals, number 173 in Springer Series in Solid-State Sciences, pages 329–372. Springer Berlin Heidelberg, 2013.

[114] N. Wagner and S. Adhikari. Symmetric State-Space Method for a Class of Nonviscously Damped Systems. AIAA Journal, 41(5):951–956, May 2003.

[115] M. Walsh and A. Lindemann. Optimization and application of riblets for turbulent drag reduction. In AlAA 22nd Aerospace Sciences Meeting, January 1984.

[116] Yan-Feng Wang, Yue-Sheng Wang, and Vincent Laude. Wave propagation in two-dimensional viscoelastic metamaterials. Physical Review B, 92(10), September 2015.

[117] P. J. Wei and Y. P. Zhao. The Influence of Viscosity on Band Gaps of 2d Phononic Crystal. Mechanics of Advanced Materials and Structures, 17(6):383–392, July 2010.

[118] J. Woodhouse. Linear damping models for structural vibrations. Journal of Sound and Vibration, 215(3):547–569, August 1998.

[119] Yong Xiao, Jihong Wen, and Xisen Wen. Longitudinal wave band gaps in metamaterial-based elastic rods containing multi-degree-of-freedom resonators. New Journal of Physics, 14(3):033042, 2012.

[120] Eli Yablonovitch. Inhibited Spontaneous Emission in Solid-State Physics and Electronics. Physical Review Letters, 58(20):2059–2062, May 1987.

[121] Y. Yong and Y. K. Lin. Propagation of decaying waves in periodic and piecewise periodic structures of finite length. Journal of Sound and Vibration, 129(1):99–118, February 1989.

[122] Pu Zhang, Mary A. Heyne, and Albert C. To. Biomimetic staggered composites with highly enhanced energy dissipation: Modeling, 3d printing, and testing. Journal of the Mechanics and Physics of Solids, 83:285–300, October 2015.

[123] Shu Zhang, Leilei Yin, and Nicholas Fang. Focusing Ultrasound with an Acoustic Metamaterial Network. Physical Review Letters, 102(19):194301, May 2009.

[124] Xin Zhang, Zhengyou Liu, Jun Mei, and Youyan Liu. Acoustic band gaps for a two-dimensional periodic array of solid cylinders in viscous liquid. Journal of Physics: Condensed Matter, 15(49):8207, 2003.